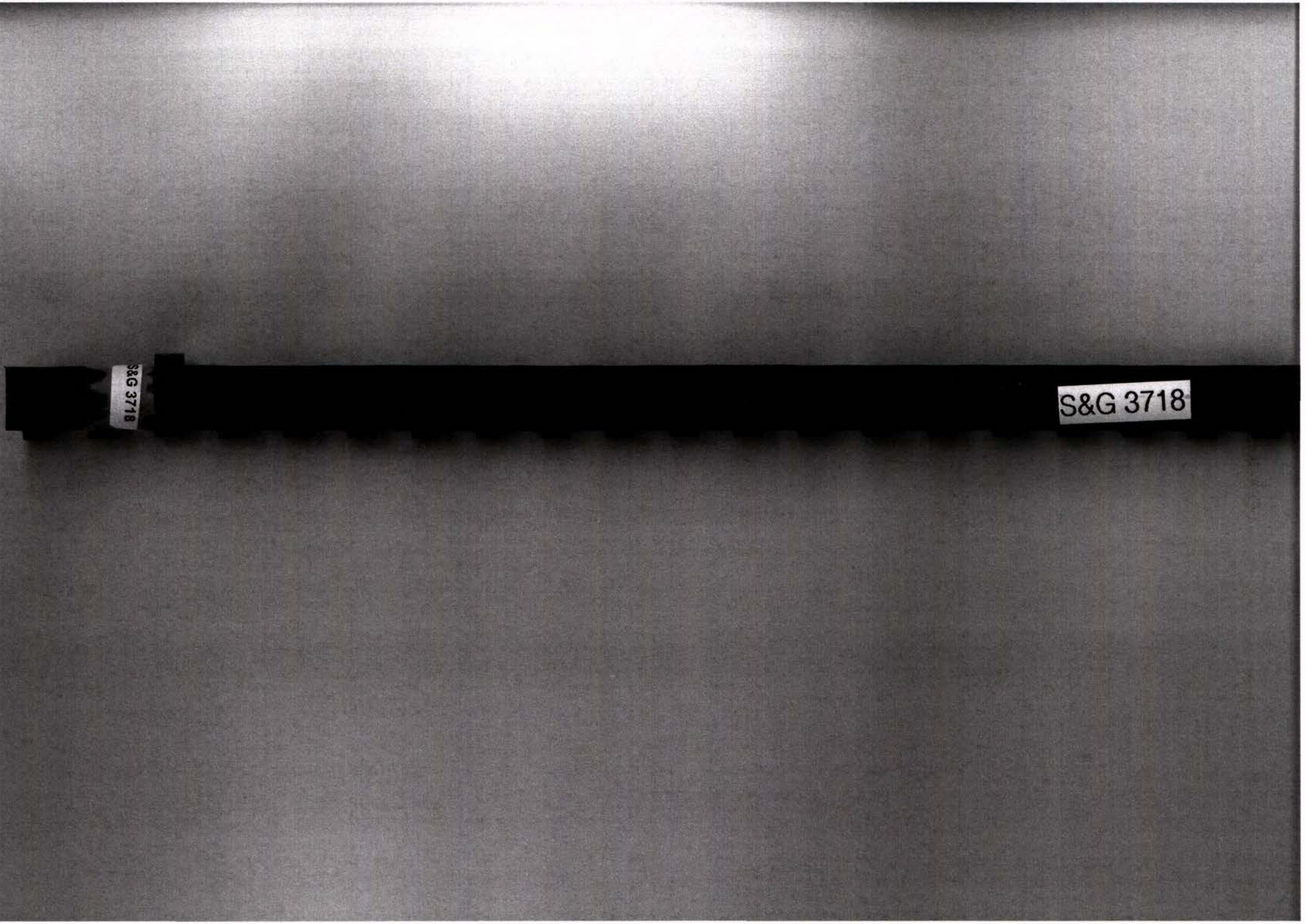
S&G 3718
S&G 3718

Final Report to the Earthquake Commission on Project No. 03/489

"Stress and Crustal Anisotropy in Marlborough and Wellington"

Natalie Balfour, Martha K. Savage and John Townend

LAYMAN'S ABSTRACT

We have investigated the mechanics of faulting and strain accommodation in the greater Marlborough region. This is a tectonically complex area containing several large faults known to have generated large earthquakes in the recent past. This research focussed on the frictional strength of those faults, and on differentiating between two hypothesized controls on the mechanical properties of the adjacent crust.

The major faults in Marlborough and Wellington play a key role in accommodating the oblique motion between the Australian and Pacific plates, and pose a high seismic risk to central New Zealand. Studies of the plate-bounding faults of the San Andreas fault system, which are geometrically similar to those in Marlborough and Wellington, suggest that the San Andreas faults are weak, and that crustal anisotropy is controlled by the ambient stress. However, whether these observations are more generally applicable to major strike-slip faults is yet to be determined. To address this concern, we have calculated the principal stress directions in Marlborough and related these results to the frictional strength of the major faults. We have also determined the directions of crustal anisotropy in Marlborough, and investigated their geometric relationships to the geological fabric and the principal stress directions.

We find that the faults are weak: they slip when shear stress is lower than expected for a typical friction coefficient. This suggests that the fault have either a moderately low friction coefficient or moderately high fluid pressure. These end-member values are similar to those inferred for the San Andreas Fault in southern California. This substantiates the hypothesis that the San Andreas fault is not unique in being frictionally weak. In the crust in Marlborough, seismic anisotropy is controlled more by the geological structures than by the prevailing stress field, so that the cause of anisotropy varies from that near the San Andreas Fault.

This research complements work in California and elsewhere into the mechanics of major faults and helps provide a mechanical framework in which to interpret future geological and geophysical studies of New Zealand tectonics.

TECHNICAL ABSTRACT

The major faults in Marlborough and Wellington are of both scientific and societal interest as they play a key role in accommodating relative plate motion in the upper plate of an oblique subduction zone, and are thought to pose a high seismic risk to central New Zealand. Studies in California suggest that some plate boundary strike-slip faults, similar to those in central New Zealand, are frictionally weak and that crustal anisotropy is controlled by the ambient stress. However, whether these observations are generally applicable to all major strike-slip faults is yet to be determined.

In this project we have addressed three main objectives, which are: to investigate the frictional properties of the faults in Marlborough in terms of their geometric relationship to the regional stress field; to investigate the cause of crustal anisotropy using results from shear-wave splitting; and to explore to what extent the faults in Marlborough are

mechanically similar to those in California. We have used inversions of focal mechanism and first motion data to calculate the stress tensor and relate it to the geometry of the major faults. We have also conducted shear-wave splitting analysis on local S phases to determine the directions of crustal anisotropy and investigate their relationship to the geological fabric and the principal stress directions.

The observed angle between the maximum horizontal compressive stress direction and the average strike of the major faults is 60°; this is substantially higher than the ~30° optimal angle expected for a vertical strike-slip fault given Byerlee friction and hydrostatic fluid pressures. The geometry can be explained, however, if the fault's friction coefficient is moderately low (~0.35) or the fluid pressure is moderately high (~0.7 × lithostatic). These end-member values are similar to those inferred for the San Andreas fault in southern California.

The maximum compressive stress direction is markedly different from the average strike of the major faults, enabling us to distinguish between stress- and structure-related anisotropy. Anisotropy directions determined from earthquakes less than 50 km deep reveal that the fast directions are principally aligned with the NE–SW-striking faults, and we therefore conclude that the anisotropy is mainly controlled by the geological fabric. Fault-parallel fast directions have also been observed in California, however stress-related anisotropy is present to greater distances from the fault there than seen in our results from Marlborough.

The observation that faulting occurs at high angles to the maximum horizontal compressive stress direction substantiates the hypothesis that the San Andreas fault is not unique in being a frictionally weak fault. The results from our shear-wave splitting calculations suggest that anisotropy in the crust varies spatially in regions of active faulting but that in Marlborough, at least, it is controlled more by the geological structures than by the prevailing stress field.

Publications relating to this project:

Publication:

Balfour, N., Savage, M.K. and Townend, J., 2005. Stress and crustal anisotropy in Marlborough, New Zealand: evidence for low fault strength and structure-controlled anisotropy. *Geophysical Journal International*, in press.

Master's thesis:

Balfour, N., 2005. Stress and crustal anisotropy in Marlborough, New Zealand: evidence for low fault strength and structure-controlled anisotropy. Unpublished M.Sc. thesis, Victoria University of Wellington, 132 pp.

Abstracts:

Balfour, N., Savage, M.K., and Townend, J., 2004. Stress and crustal anisotropy in Marlborough, New Zealand: evidence for low fault strength and structure-controlled anisotropy. AGU, 85(47), Fall Meet. Suppl., Abstract T33E-02.

STRESS AND CRUSTAL ANISOTROPY IN MARLBOROUGH, NEW ZEALAND: EVIDENCE FOR LOW FAULT STRENGTH AND STRUCTURE-CONTROLLED ANISOTROPY

Natalie Balfour

Geophysics
2004

A Research Project submitted to the School of Earth Sciences,
Victoria University of Wellington, as partial fulfillment of the degree of
MSc in Geophysics, 2004.

School of Earth Sciences
Victoria University of Wellington

Balfour, N., Savage, M.K., and Townend, J., 2004. Stress and shear-wave splitting measurements in Marlborough and their implications for fault strength and structure-controlled crustal anisotropy. In: Manville, V., and Tilyard, D. (eds.), Programme and Abstracts, Geological Society of New Zealand/New Zealand Geophysical Society/26th Annual Geothermal Workshop combined conference "GEO3", Taupo, New Zealand. Geological Society of New Zealand Misc. Publ. 117A.

ABSTRACT

The major faults in Marlborough and Wellington are of both scientific and societal interest as they play a key role in accommodating relative plate motion in the upper plate of an oblique subduction zone, and are thought to pose a high seismic risk to central New Zealand. Studies in California suggest that some plate boundary strike-slip faults, similar to those in central New Zealand, are frictionally weak and that crustal anisotropy is controlled by the ambient stress. However, whether these observations are generally applicable to all major strike-slip faults is yet to be determined.

In this project we have addressed three main objectives, which are: to investigate the frictional properties of the faults in Marlborough in terms of their geometric relationship to the regional stress field; to investigate the cause of crustal anisotropy using results from shear-wave splitting; and to explore to what extent the faults in Marlborough are mechanically similar to those in California. We have used inversions of focal mechanism and first motion data to calculate the stress tensor and relate it to the geometry of the major faults. We have also conducted shear-wave splitting analysis on local S phases to determine the directions of crustal anisotropy and investigate their relationship to the geological fabric and the principal stress directions.

The observed angle between the maximum horizontal compressive stress direction and the average strike of the major faults is 60°; this is substantially higher than the ~30° optimal angle expected for a vertical strike-slip fault given Byerlee friction and hydrostatic fluid pressures. The geometry can be explained, however, if the fault's friction coefficient is moderately low (~0.35) or the fluid pressure is moderately high (~0.7×lithostatic). These end-member values are similar to those inferred for the San Andreas fault in southern California.

The maximum compressive stress direction is markedly different from the average strike

of the major faults, enabling us to distinguish between stress- and structure-controlled anisotropy. Anisotropy directions determined from earthquakes less than 50 km deep reveal that the fast directions are principally aligned with the NE–SW-striking faults, and we therefore conclude that the anisotropy is mainly controlled by the geological fabric. Fault-parallel fast directions have also been observed in California, but stress-related anisotropy is present to greater distances from the fault there than seen in our results from Marlborough.

The observation that faulting occurs at high angles to the maximum horizontal compressive stress direction substantiates the hypothesis that the San Andreas fault is not unique in being a frictionally weak fault. The results from our shear-wave splitting calculations suggest that anisotropy in the crust varies spatially in regions of active faulting but that in Marlborough, at least, it is controlled more by the geological structures than by the prevailing stress field.

ACKNOWLEDGEMENTS

Firstly, I would like to thank my supervisors Martha Savage and John Townend, for all their guidance with the writing of my thesis and the time they have spent helping me with programs. It has been a pleasure working with people who are enthusiastic and motivate me to continue studying geophysics. Thank you to the Earthquake Commission who funded this project (grant 03/489) and to Geological and Nuclear Sciences, National Science Foundation and the University of Colorado who helped with the data collection for the anisotropy study; and to GEONET and IRIS Data Management Centre for archiving and supplying the data.

Thanks to the people who supplied me with data, Etienne Audoine, Mark Chadwick, Donna Eberhart-Phillips, Ken Gledhill, Peter McGinty and Martin Reyners. And to everyone who helped organise anisotropy study, Craig Jones, Anne Sheehan, and those who helped with fieldwork. Also to Ralph Wahrlich for all your help with Unix and loading software. To Geoff Abers and Nick Teanby who supplied me with their programs and technical support. Thanks to the lovely people at the School of Earth Science office and to the Jill the Librarian. And to my examiners Tim Little and John Cassidy for all their helpful comments.

Thanks to all my family, especially Lorraine, Peter and Nic, for their endless support. A special thank you to Grandy Balfour who is my constant source of inspiration. Also to Graham and Glennys Elliot who have been my family away from home.

To my fellow graduate students at the School of Earth Sciences, especially Mathieu Duclos and Michelle Salmon for their help with SAC, Nick Horspool and Guy Baldock for their GMT expertise, Audrey Galvé, and Katrina Marson-Pidgeon.

Thanks to Jessica Mills and Cassandra Crowley, who put up with me on a daily basis. And to all my friends at the Victoria University of Wellington and in other areas of my life. And lastly an apology to anyone who I may have inadvertently forgotten, thank you.

CONTENTS

1 Introduction **3**

1.1 Objectives 3

1.2 Geological, tectonic and seismological setting 4

1.3 Related studies 6

1.3.1 Previous seismic anisotropy studies in central New Zealand 6

1.3.2 Previous crustal stress studies 10

1.3.3 Previous studies of crustal strain 13

1.3.4 Related studies for California 14

2 Theory **17**

2.1 Seismic anisotropy 17

2.1.1 What is seismic anisotropy? 17

2.1.2 Hexagonal anisotropy 18

2.1.3 Causes of crustal anisotropy 22

2.2 Focal mechanisms and stress 22

2.2.1 Definitions and the stress tensor 23

2.2.2 Stress indicators 27

2.2.3 Sources of stress 28

2.2.4 Stress inversion algorithms 29

3 Seismic Anisotropy **33**

3.1 Introduction 33

3.2 Data selection 34

3.2.1 Depth-dependance of observations 35

3.2.2 Importance of the shear-wave window 35

3.2.3 Quality of the data 36

3.3 Data processing 37

3.3.1 Automated shear-wave splitting technique 38

3.3.2 Cluster analysis and identification of the result 40
3.4 Results 42
3.4.1 Statistics 42
3.4.2 Fresnel zones 43
3.4.3 CU/VUW broadband array 44
3.4.4 CU/VUW short-period array 48
3.4.5 GNS short-period results 52
3.5 Discussion 57

4 Focal Mechanisms and Stress Orientations **61**
4.1 Introduction 61
4.2 Comparison of stress inversion techniques 64
4.2.1 A comparison of inversion algorithms 65
4.2.2 A comparison of methods for constructing focal mechanisms 69
4.3 Stress results 72
4.3.1 Crustal stress in the Lake Tennyson area 72
4.3.2 Crustal stress directions in Marlborough and Wellington computed from first motion data 73
4.3.3 Crustal stress directions in Marlborough and Wellington computed from focal mechanism data 75
4.4 Summary 77

5 Discussion **79**
5.1 Crustal stress in Marlborough 79
5.2 Crustal anisotropy 83
5.3 Conclusions 86

6 References **89**

A Published Focal Mechanism Data **95**

B Shear-Wave Splitting Measurements **103**

C Events used for Stress Inversions **115**

D Documentation for the MOTSI Inversion Codes **127**

D.1 Main inversion codes 127

D.2 Other useful scripts related to MOTSI 128

D.3 Plotting codes 128

D.4 Input format 129

D.5 Running codes on Mac OSX 130

FIGURES

1.1 Map of New Zealand with bathymetry and related tectonic features. 4
1.2 Map of seismicity and faults in Marlborough 6
1.3 Station deployments for the anisotropy studies. 7
1.4 Stations used in the anisotropy study. 8
1.5 Published splitting results from previous studies of crustal anisotropy 9
1.6 Summary of published focal mechanisms used in this study 11

2.1 Wave propagation through an anisotropic medium 19
2.2 Illustration of shear-wave splitting 21
2.3 Illustration of the stress tensor 23
2.4 Illustration of the principal stress coordinate system. 24
2.5 Rotation of coordinate systems 25
2.6 Anderson's classification of faults 27
2.7 Schematic representation of stress determined from different input data. . . 29
2.8 An example of output from `SLFAST` 30
2.9 An example of output from `FMSI` 31
2.10 An example of output from `MOTSI`. 32

3.1 Locations of stations used for shear-wave splitting analysis 34
3.2 Flow diagram comparing manual and automated shear-wave splitting analysis techniques. 37
3.3 Diagnostic plots of a single shear-wave splitting measurement. 38
3.4 Diagnostic plots from cluster analysis. 40
3.5 Geometry of overlapping Fresnel zones used to calculate the percentage of overlap. 44
3.6 Rose diagrams of the fast direction results from the CU/VUW broadband array. 46
3.7 Shear-wave splitting results for the broadband stations of the CU/VUW deployment. 47
3.8 Depth-dependance of shear-wave splitting at WAG 48

3.9 Rose diagrams of the fast direction for each station in the CU/VUW short-period array. 50
3.10 Shear-wave splitting results for the short-period stations of the ALI00 array from the CU/VUW deployment. 51
3.11 Splitting measurements from station ALIE5 51
3.12 Variation of the fast direction with initial polarisation inferred from shear-wave splitting. 52
3.13 Variation of the fast direction with initial polarisation determined from focal mechanisms 53
3.14 Comparison of initial polarisations determined from shear-wave splitting analysis with those from focal mechanisms 53
3.15 Shear-wave splitting results for the short-period stations of the GNS deployment. 55
3.16 Rose diagrams of the fast direction for each station in the GNS short-period deployment. 56
3.17 The effect of faults on incoming rays 57
3.18 Shear-wave splitting results from a single event recorded at several stations. 59
3.19 Splitting measurements plotted along ray paths for station PUH. 60

4.1 Epicenters of the events used for stress calculations 62
4.2 Comparison of stress results from SLFAST and published stress data 64
4.3 Stress results near Lake Tennyson 65
4.4 Histograms of stress ratio estimates from FMSI and MOTSI. 66
4.5 Map of results obtained with different stress inversion techniques in Marlborough. 68
4.6 The result of computing focal mechanism with the stress constraint using MOTSI. 70
4.7 P and T axes of focal mechanisms computed using different techniques . . 71
4.8 The effect of the stress constraint on focal mechanisms near Lake Tennyson. 71
4.9 Focal mechanisms of the 1990 Lake Tennyson earthquake and its aftershocks 72
4.10 Map of Marlborough with stress results from all available focal mechanisms 76
4.11 Relationship of S_{Hmax} to the average orientation of the major faults and the plate motion vector. 77

5.1 Plot of all calculated S_{Hmax} directions 80
5.2 Mohr diagram illustrating the relationship of stresses to fault orientation . . 81
5.3 Splitting measurements from all studies on local-S phases in central New Zealand 84

TABLES

2.1 Summary of stress the inversion algorithms 29

3.1 Overall mean and standard deviation of the fast direction and delay time from each deployment 43

3.2 Summary of statistics for each station in the CU/VUW broadband deployment. 45

3.3 Summary of statistics for each station in the CU/VUW short-period deployment 49

3.4 Summary of statistics for each station in the GNS short-period deployment. 54

4.1 Summary of the data sets used in stress inversions 63

4.2 Comparison of stress results obtained using two different inversion techniques and the same set of focal mechanisms 64

4.3 Stress results for clusters used in the focal mechanism comparison 70

4.4 Lake Tennyson stress results 73

4.5 Stress results obtained from various inversion algorithms for the GNS Marlborough data 74

4.6 Stress results obtained for different clusters in Marlborough using all published focal mechanism data. 75

A.1 Summary of published focal mechanisms 96

B.1 Summary of splitting measurements for broadband instruments. 104

B.2 Summary of splitting measurements for short-period array ALI 108

B.3 Summary of splitting measurements for the GNS deployment 111

C.1 Summary of the events used in inversions 116

CHAPTER 1

INTRODUCTION

This chapter provides a synopsis of the objectives and background of this project. It contains an introduction to the tectonic setting of central New Zealand as well as an overview of related work from New Zealand and California.

1.1 Objectives

The aim of this project is to investigate the tectonic stress field and crustal anisotropy in central New Zealand and to help answer the questions: Are all large strike-slip faults weak and what is the dominant cause of anisotropy in the crust. We use stress calculations based on earthquake focal mechanism and first motion data to determine the principal stress directions and then investigate the frictional strength of the faults in Marlborough. To test the consistency of the stress results we apply a variety of different techniques to each data set. A recently developed automated splitting code is used for the shear-wave splitting analysis on three deployments in Marlborough and the fast direction is used to establish whether the observed anisotropy is controlled by the stress field or the geological structure. The results from Marlborough are compared with studies from the San Andreas fault (SAF) system since the geometries of the faults are similar.

Studies of the SAF have concluded that it is frictionally weak (Townend and Zoback, 2004) and therefore the question arises of whether this is characteristic of all big faults. By studying another system of transform faults, namely those in Marlborough, we can come one step closer to answering this question.

1.2 Geological, tectonic and seismological setting

The New Zealand land mass is part of a complex plate boundary between the Australian and Pacific Plates (Figure 1.1). In the northeast of New Zealand, the Pacific Plate is subducting

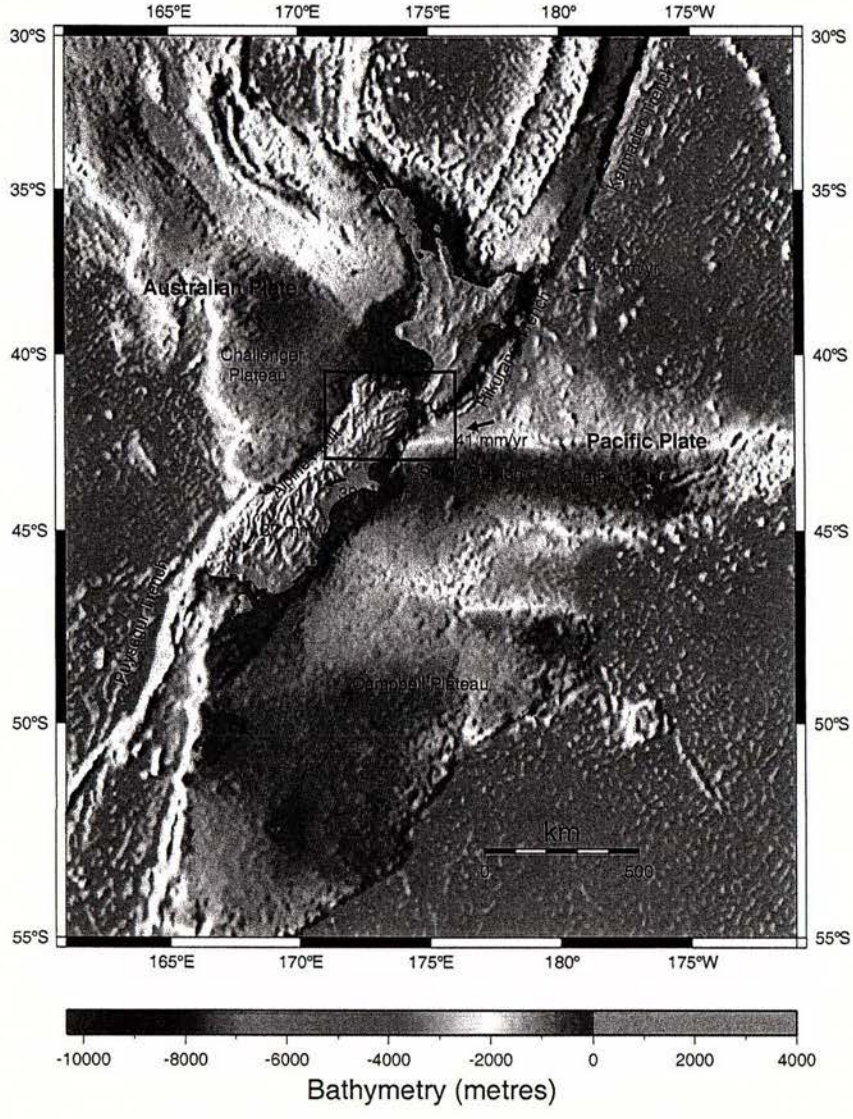

Figure 1.1 *Map of New Zealand showing bathymetry and related tectonic features. The region covered in this study is outlined by the box.*

beneath the Australian Plate (marked by the Hikurangi and Kermadec trenches) while southwest of New Zealand the opposite is occuring (marked by the Puysegsur Trench). Linking these two subduction systems is the Alpine Fault, an oblique transform fault separating two

blocks of continental crust, the Challenger Plateau to the west and the Campbell Plateau to the east. The Marlborough Fault System (MFS) marks the transition from subduction along the Hikurangi Trench in the north to the Alpine fault in the south.

The faults in the MFS are predominantly dextral strike-slip, although they do exhibit a component of reverse motion (Anderson *et al.*, 1993). The average strike of the faults is ~55° and their dips vary from 60° to near-vertical (as indicated by 1:250,000 New Zealand Survey Geological Maps, Sheets 13, 14, 15, 15, 16 and 18). Several of the major faults, and in particular the Awatere fault, have associated subvertical low-velocity zones that extend to 23 km depth and are interpreted as regions of high pore fluid pressure (Eberhart-Phillips and Reyners, 1997). The plate motion vector is oriented at ~20° to the strike of the faults (DeMets *et al.*, 1990), and geodetic data and the inversion of slip vectors suggest that 80–100% of the relative plate motion is accommodated by the Marlborough faults (Bibby, 1981; Holt and Haines, 1995; Bourne *et al.*, 1998). The plate interface between the Australian Plate and Pacific Plate has been investigated by Bibby (1981) and Reyners (1998) among others, and is suggested to be coupled beneath Wellington and locked beneath Marlborough on the basis of the high ratio of slip rate deficit to the total predicted slip rate. This difference is thought to be due to the increase in thickness of the subducted plate to the south causing it to be more buoyant than the thinner oceanic crust further north (Reyners, 1998).

The Alpine-Wairau Fault (Figure 1.2) separates two different geologic provinces: the Western Province is comprised of Paleozoic plutonic, volcanic and metamorphic terranes that have been offset by 450 km of strike-slip motion along the Alpine Fault, while the Eastern Province is made up of Mesozoic Torlesse greywacke, and Haast schist that has been uplifted and exposed near the Alpine Fault (Sutherland, 1999).

Seismicity in the region deepens from east to west and reaches a maximum depth beneath Nelson of ~350 km (Figure 1.2). Northwest of Nelson the seismicity shallows and studies suggest that the faults in this region accommodate little of the plate motion (Holt and Haines, 1995). Extensive studies have been conducted to determine the plate configuration beneath the northern South Island, but there is still some controversy over what happens to the subducted slab south of Kaikoura (Reyners and de J. Robertson, 2004; Furlong and Kamp, 2004).

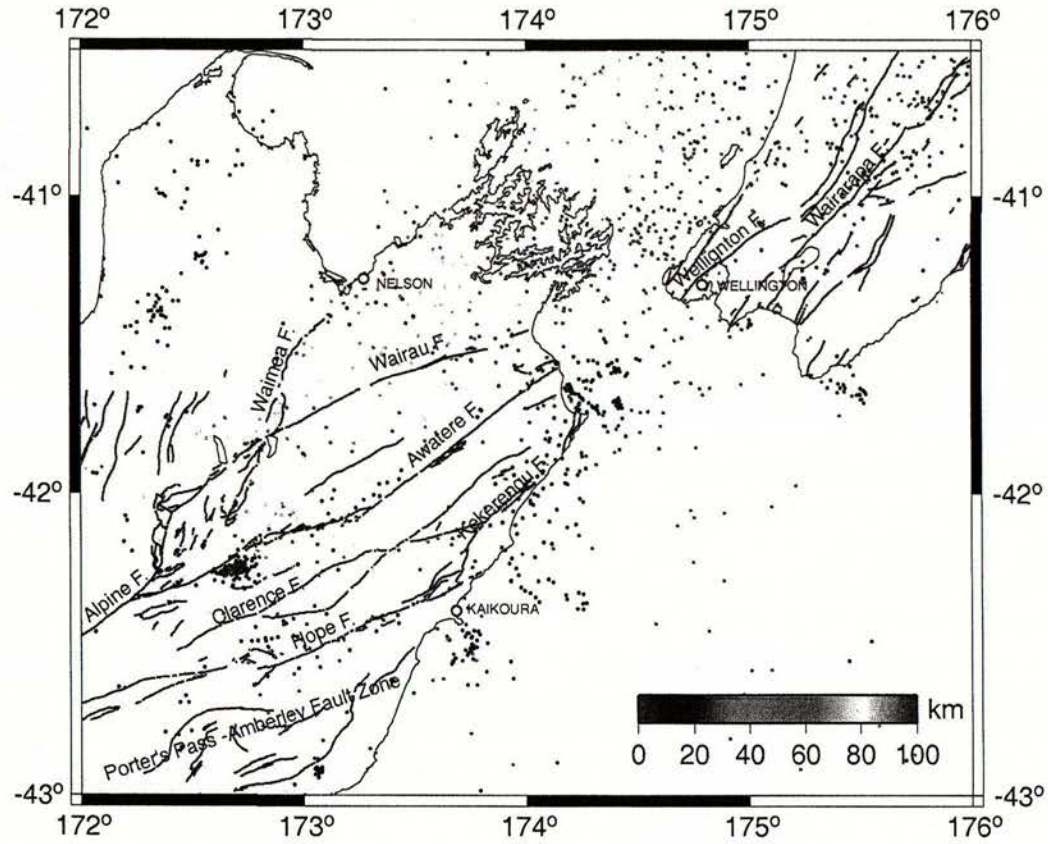

Figure 1.2 *Map of faults and seismicity in Marlborough and Wellington. The events shown are those larger than magnitude 3.5 occurring between 1989 and 2004.*

1.3 Related studies

A wide variety of geophysical studies have been conducted in central New Zealand as the region has a complex crustal structure and potentially high seismic hazard. In the following sections, we discuss several studies that motivate this project and are helpful in understanding the relationships between faulting, stress, strain and crustal anisotropy in this region.

1.3.1 Previous seismic anisotropy studies in central New Zealand

Anisotropy in the lower North Island has been studied using a variety of seismic phases; Pn (Smith and Ekström, 1999), SKS (Marson-Pidgeon and Savage, 1997; Marson-Pidgeon *et al.*, 1999; Klosko *et al.*, 1999) and S-waves from local earthquakes ("local S") (Gledhill, 1991; Gledhill and Stuart, 1996; Matcham *et al.*, 2000). In the northern South Island SKS

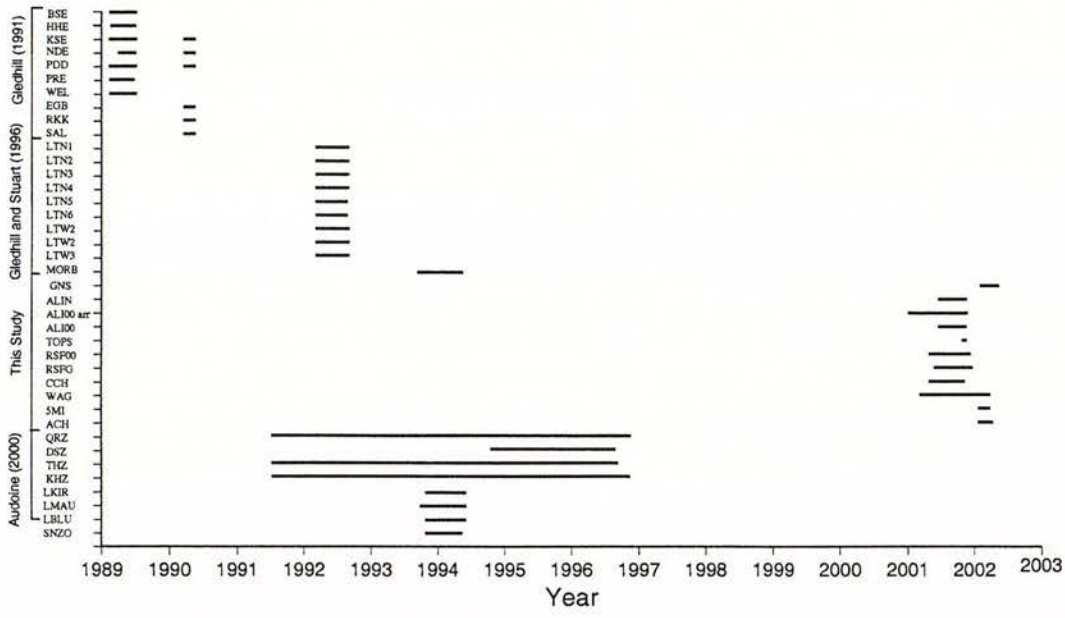

Figure 1.3 *The duration of the deployment of stations used for studies of anisotropy. Station GNS denotes all stations in the GNS Marlborough deployment.*

(Klosko *et al.*, 1999) and local S phases (Audoine *et al.*, 2000; Audoine, 2002) have been used to study the mantle; however, no studies of the South Island have focussed solely at the crustal component of anisotropy. Bearing in mind that one aim of this study is to investigate crustal anisotropy, the following reviews of previous work focus on studies involving shallow earthquakes and local S phases. The periods of instrument deployment for each anisotropy study are shown in Figure 1.3 and the location of each station is shown in Figure 1.4.

North Island

Gledhill (1991) conducted a closely spaced study on the Wellington Peninsula and recorded over 300 local earthquakes (with hypocenters between 0–75 km deep) of which 114 were used for shear-wave splitting analysis (Figure 1.5). The large changes in fast direction (61–137°) from station to station and delay times of 0.02–0.22 seconds led Gledhill (1991) to infer that the splitting was caused by anisotropy above the plate interface. He also identified more than three anisotropic bodies, of which the shallowest was concluded to be located in the top 2–3 km of the crust. Gledhill (1991) suggested the cause of anisotropy was a combination of extensive-dilatancy anisotropy (EDA) (Crampin, 1994) related to stress-aligned

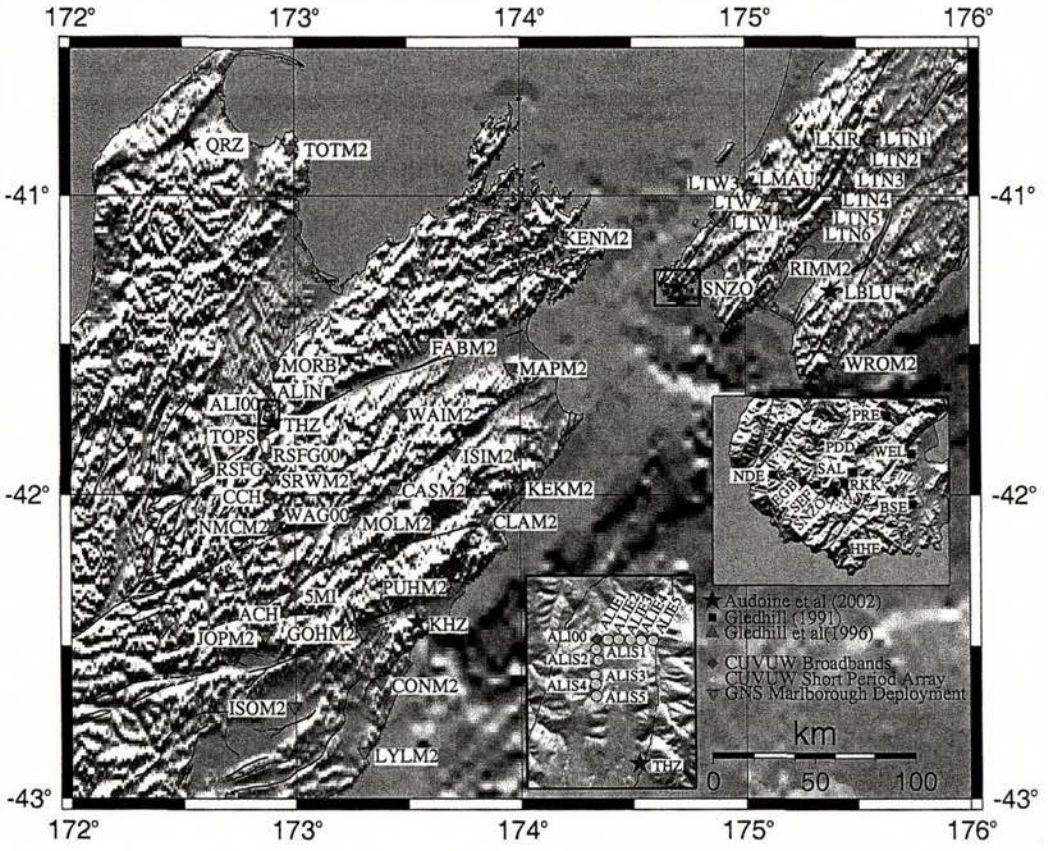

Figure 1.4 *Stations used in the seismic anisotropy study.*

microcracks and structure-related anisotropy.

Gledhill and Stuart's (1996) study of crustal anisotropy used 66 earthquakes of between 5 km and 42 km in depth from an L-shaped array, which crosses the Tararua Ranges north of Wellington (Figure 1.5). The average fast direction was 51° with delay times of 0.01–0.2 s. The results obtained with this array led to similar conclusions to those of Gledhill (1991), in which the fast direction is aligned with the geological structure dominated by the Tararua Ranges and NE–SW-striking faults. In this study, less station-to-station variation was seen than on the Wellington Peninsula, although one station gave a fast direction at 90° to that observed at other stations; this led Gledhill and Stuart (1996) to conclude that near-surface anisotropy was present.

Matcham *et al.* (2000) conducted a detailed study of crustal anisotropy beneath a permanent station in the Wellington region (SNZO, Figure 1.5). The results for events shallower

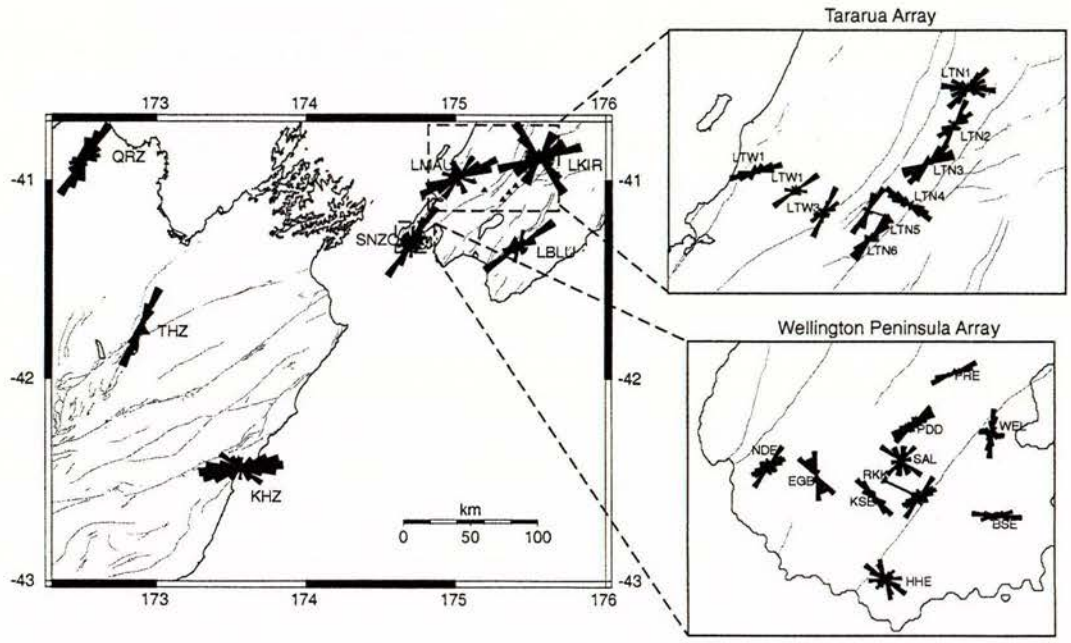

Figure 1.5 *Published splitting results from local S phases (Audoine et al (2000), Gledhill (1991) and Gledhill and Stuart (1996)). The stations LMAU and LKIR from Audoine et al's (2000) study are the same as LTW1 and LTN1 from Gledhill and Stuart's (1996) study.*

than 50 km exhibited similar delay times and variations in fast direction to those of Gledhill (1991) and Gledhill and Stuart (1996); that is, the delay times were 0.1–0.4 s and the fast direction showed two dominant orientations ~90° apart.

The results of Audoine *et al.*'s (2000) study of deeper earthquakes in the lower North Island indicated a fast direction of 57±28°, sub-parallel to the strike of the Hikurangi margin, and an average delay time of 0.3 s. However, there was scatter in the data, especially at station LKIR where there was a bimodal distribution with fast directions 90° apart. Audoine *et al.*'s (2000) and Matcham *et al.*'s (2000) studies produced larger delay times than those of Gledhill (1991) and Gledhill and Stuart (1996), which is most likely the result of using deeper earthquakes (>50 km) that travel a greater distance through any anisotropic material. Two of the stations in Audoine *et al.*'s (2000) study (LMAU and LKIR) are in the same location as those used in the study by Gledhill and Stuart (1996) (LTW1 and LTN1) and the fast directions from both studies are similar.

South Island

Audoine *et al.*'s (2000) study also covered the northern South Island. Their study was the first to use shear-wave splitting analysis of local S phases in the South Island; it was based on four stations and recorded events over a much longer period than the North Island deployments (Figure 1.3). The shallowest earthquakes used for analysis were less than 100 km in depth and the results indicated fast directions of 45±28°, sub-parallel to the strike of the faults (Figure 1.5). The anisotropy was interpreted to be due to a body of metamorphosed schist between 50 and 80 km depth. The east coast station (KHZ) showed a more varied fast direction with a predominant east-west trend, which is in the direction of the maximum horizontal compressive stress obtained by McGinty *et al.* (2000) (Section 1.3.2). Audoine *et al.* (2000) suggested that the variation might be due to multiple anisotropic bodies and used the distances between stations to constrain the dimensions of the bodies. Since most of the earthquakes used in their study were deeper than 50 km, it is likely that the observations include a mantle or subducted slab signature.

Other studies in the South Island have focused on teleseismic events and the results are indicative of anisotropy in the mantle rather than in the crust (Klosko *et al.*, 1999; Smith and Ekström, 1999).

1.3.2 Previous crustal stress studies

Geophysical studies of tectonic stress in central New Zealand

In this study we use focal mechanisms published by previous authors to carry out stress inversions (Figure 1.6). Stress inversion algorithms typically estimate the three principal stress directions (minimum, intermediate, and maximum compressive stress) and the stress ratio (R) (for more explanation and nomenclature see Section 2.2). The majority of the focal mechanism data were taken from a study of plate coupling in Marlborough and Wellington (Reyners *et al.*, 1997). Other focal mechanism data come from studies by Anderson *et al.* (1993), Doser *et al.* (1999), McGinty *et al.* (1997) and from the Harvard CMT (Centroid Moment Tensor) and NEIC (National Earthquake Information Centre) catalogues. Although over 280 focal mechanisms have been determined for the greater Marlborough region few

have been used to date for stress inversions. McGinty *et al.* (2000) calculated principal stress directions for three areas within the overlying plate in the northern South Island. The axis of maximum compressive stress was oriented (trend/plunge) at 162/46 in northwest Nelson, 300/30 in northern Marlborough, and 118/6 in southern Marlborough. Leitner *et al.* (2001) determined stress directions in the central Alpine Fault region using Michael's (1987) inversion technique (Chapter 2.2.4), which yielded a subhorizontal maximum compressive stress axis with an azimuth of 110–120°.

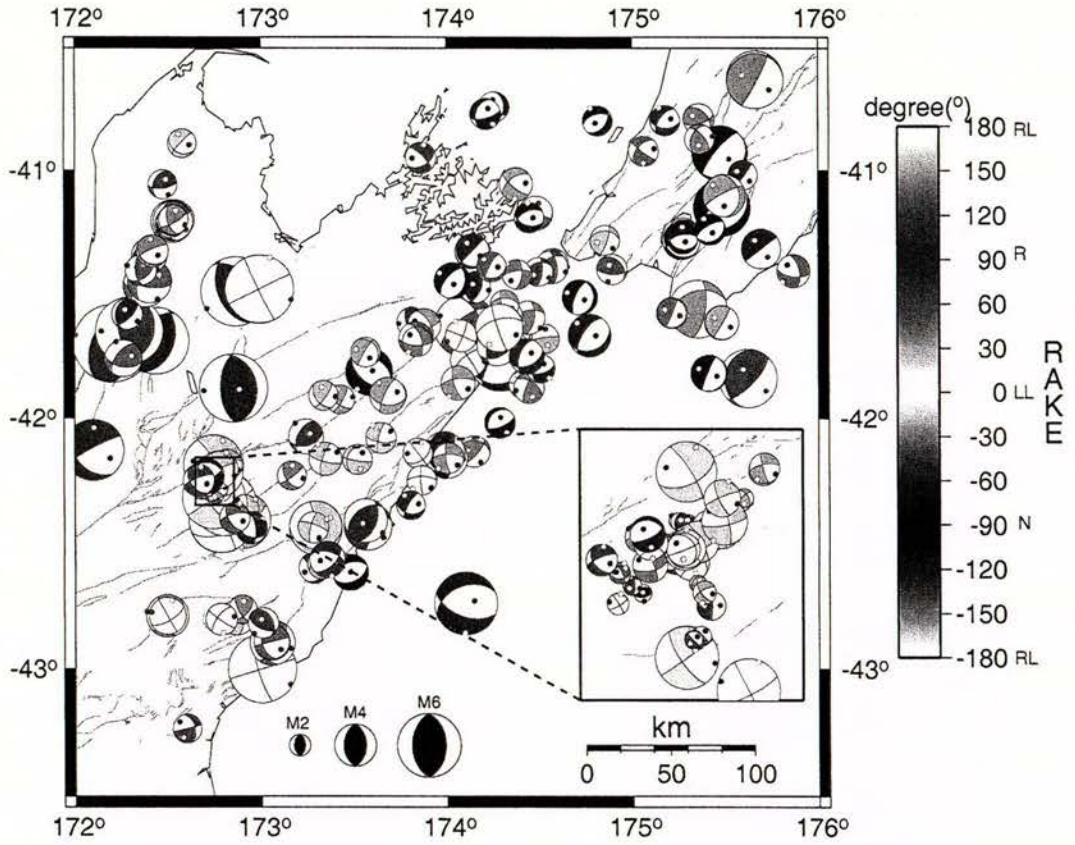

Figure 1.6 *Summary of published focal mechanisms used in this study. The compressional quadrant is shaded according to rake. On the colour scale, LL denotes left-lateral, RL right-lateral, R reverse faulting and N normal faulting. The solid dot in the focal mechanism is the P axis and the hollow circle is the T axis. The inset is an enlargement of the focal mechanisms associated with the Lake Tennyson earthquake.*

A region of dense seismicity associated with the 1990 Lake Tennyson earthquake (M_L =5.8) has been the dominant locus of activity in Marlborough during the last 15 years (Figure 1.6, enlarged region). McGinty *et al.* (1997) relocated the earthquakes and constructed focal

mechanisms using first motion data obtained during a deployment of portable seismographs. In this study we obtained both the first motion and focal mechanism data used by McGinty *et al.* (1997) and incorporated it in our stress inversions.

Liu and Bird (2002) modelled stress using a thin-shell finite element method that incorporates topography, heat flow and the geometry of active faults. The plate velocities were determined from the NUVEL-1A model and the boundary conditions were calculated using the Euler vector; however the velocity boundary conditions in the northeast of New Zealands caused complications in the central North Island and several models with different boundary conditions were used. Their results found that the average frictional strength of faults in New Zealand to be low, with an effective friction coefficient of 0.17.

Geological stress indicators

Geological stress estimates have been made in Nelson (Pettinga and Wise, 1994) and the Porters Pass Fault Zone (Nicol and Wise, 1992) and been used to compare the MFS to the SAF system. Pettinga and Wise (1994) used fault slickenside data from Nelson and obtained results indicating a maximum compressive stress direction at a high angle to the Waimea fault. The inversion technique used in that study assumes a low coefficient of friction of 0.4 and since one of the aims of the current project is to investigate the frictional strength of the major faults, we avoid using algorithms requiring a friction assumption. The study of the Porters Pass Fault zone by Nicol and Wise (1992) was similar to that in Nelson and used the same inversion technique; Nicol and Wise's (1992) results indicated that the azimuth of maximum compressive stress is 105–138°. Both Nicol and Wise (1992) and Pettinga and Wise (1994) argued that a SAF model cannot be applied to the MFS as the plate motion direction relative to the strike of the faults is different; however, their results reveal the maximum compressive stress direction to lie at a high angle to the faults, which is similar to what is observed in Southern California. The stress directions obtained from fault slickenside data exhibit more variation than those obtained from focal mechanisms. There is also a problem that arises over which episode of deformation the data are related to, as only the most recent episode of deformation will reflect the current stress regime and unless all the slip events were contemporaneous the stress result will represent a juxtaposition of possibly dissimilar

stresses.

Another geological study of stress and strain in Marlborough was by Little and Jones (1998) and used cobble extension fractures found in a conglomerate to estimate stress orientations. This was part of a broader study of slip partitioning around the northern end of the Awatere Fault. The slip data obtained from the fractures were inverted for stress using an algorithm by Gephart (1990). Results indicated an ESE direction of the minimum compressive stress, which Little and Jones (1998) suggested to be reminiscent of the regional stress regime during the Cenozoic.

Another reliable way to determine the stress tensor is to use in situ borehole data from hydraulic fracturing or borehole breakouts (Zoback and Zoback, 2002). Most of these data are collected when exploring for oil or gas reservoirs and unfortunately Marlborough contains few basins suitable for exploration. The closest drill hole was drilled by Indo-Pacific Oil in Northern Canterbury (Arcadia-1), however no dipmeter or oriented caliper data were collected and therefore stress directions have not be determined.

1.3.3 Previous studies of crustal strain

Triangulation surveys have been conducted in New Zealand since the late 1800s. However, it was not until the 1950s when survey stations were reoccupied that the observations could be used to calculate strain. Initially the surveys were believed to be too inaccurate to determine strain, but Bibby (1975) managed to successfully calculate the strain over the faults in Marlborough. Early work in Marlborough, reported by Bibby (1975), compared an early low-resolution survey, between 1878 and 1884, with a survey conducted by the DSIR in 1951–1960. Since then, repeated triangulation and GPS (Global Positioning System) surveys have provided a detailed data set with which to study deformation kinematics in Marlborough. Bibby (1981) and Bourne *et al.* (1998) observed a rotation in the azimuth of relative maximum shortening from NW–SE on the east coast to E–W near the Wairau Fault. Reilly (1990) used triangulation data to investigate horizontal deformation along the Hikurangi margin and found that between Hawke Bay and the Chatham Rise there was a consistent azimuth of relative maximum shortening of 110°. Recent calculations of strain from GPS measurements in the Wellington region have been made by Darby and Beavan (2001)

to investigate coupling of the plate interface. They found a 35° change in the orientation of the principal axis of relative maximum shortening from 102° in the west to 137° in the east, which they attributed to partitioning of fault-parallel and fault-perpendicular components of strain.

A study of strain throughout New Zealand indicates high shear strain rates of ~0.25 ppm/yr in the Marlborough region (Beavan and Haines, 2001). Strain rates calculated from Quaternary slip rates and rock uplift suggest the area undergoing the most strain in the northern South Island is between the Wairau and Hope faults (Bibby, 1981; Walcott, 1984; Holt and Haines, 1995).

1.3.4 Related studies for California

We compare results pertaining to the SAF system with our results from Marlborough as the two fault systems are geometrically similar and have been compared before (Yeats and Berryman, 1987) and since the SAF system has been studied extensively. The relevance of the two fault systems being geometrically similar has been disputed, as the MFS has a larger component of oblique-slip than the SAF (Nicol and Wise, 1992; Pettinga and Wise, 1994); however, our goal here is to determine whether they nevertheless have comparable frictional strength. Stress measurements from borehole and focal mechanism data suggest that the San Andreas fault is frictionally weak (Townend and Zoback, 2001; Hickman and Zoback, 2004; Townend and Zoback, 2004). The optimal angle between the strike of the fault and the maximum compressive stress direction for shear failure given a coefficient of friction of 0.6–1.0 ("Byerlee's friction" obtained from laboratory measurements) and Coulomb's faulting criterion is 22.5–30° (Sibson, 1985) (see Section 2.2.1) . The angles observed in California are 60–85°, implying that the faults are frictionally weak with an apparent friction coefficient of 0.2–0.3 in Southern California and ~ 0.06 the San Francisco Peninsula (Jones, 1988; Townend and Zoback, 2004). Heat flow studies support this, due to the absence of the heat flow anomaly expected for transform faults with Byerlee coefficients of friction and hydrostatic pore fluid pressures (Lachenbruch and Sass, 1992; Fulton *et al.*, 2004; Williams *et al.*, 2004).

Shear-wave splitting studies on local S phases in California are also numerous and sug-

gest that anisotropy is primarily controlled by the stress field (Boness and Zoback, 2004; Zinke and Zoback, 1994). Most of the studies show fast directions aligned with the maximum compressive stress direction, although fault-parallel fast directions are also present. Zinke and Zoback (1994) observed spatial variation in the fast directions; close to the Calaveras fault in central California, the fast directions are fault-parallel and further from the fault they are in the direction of the maximum compressive stress. This suggests that the stress field has a strong influence on the anisotropy and that only regions close to the fault (<3 km) are affected by the fault fabric. Zhang and Schwartz (1994) also observed two fast directions, but the bulk of the fast directions were parallel to the fault and they suggested that mineral alignment is the main source of anisotropy. Paulssen (2004) supported this claim but also gave evidence of transverse isotropy with a horizontal axis of symmetry due to foliation in schist, as well as azimuthal anisotropy. Recent evidence from the SAFOD (San Andreas Fault Observatory at Depth) pilot hole supports the hypothesis of stress-related anisotropy, as the fast directions recorded at various depths are consistently aligned with the axis of maximum compressive stress (Boness and Zoback, 2004). These studies shows that there are two causes for crustal anisotropy, both stress and structure.

CHAPTER 2

THEORY

The purpose of this chapter is to summarise the theory and mathematical background behind seismic anisotropy and tectonic stress. This may assist in understanding of the methods and results discussed in following chapters.

2.1 Seismic anisotropy

2.1.1 What is seismic anisotropy?

Anisotropy refers to a property of a medium that differs depending on orientation. Seismic anisotropy occurs when the wave speed depends on the direction of propagation and the orientation of an anisotropic medium. The following explanation of seismic anisotropy is based on that of Babuska and Cara (1991).

When seismic waves travel through an elastic medium, the stresses are proportional to the strains in accordance with Hooke's Law (equation 2.1), which is the most general representation of elasticity.

$$\sigma_{ij} = c_{ijkl}\varepsilon_{kl} \tag{2.1}$$

where

$$\varepsilon_{kl} = \frac{1}{2}\left(\frac{\partial u_k}{\partial x_l} + \frac{\partial u_l}{\partial x_k}\right) \tag{2.2}$$

In Equation 2.1, σ_{ij} are the components of the second-order stress tensor, ε_{kl} are components of the second-order strain tensor, where $\partial u_k/\partial x_l$ are derivatives of displacement, and c_{ijkl} are components of the fourth-order stiffness tensor that define the material properties of the

medium. In the most general form c_{ijkl} has 81 elastic constants; however since the stress and strain tensors are symmetric and taking into account thermodynamic considerations, the stiffness tensor is fully represented by at most 21 independent constants. Due to symmetry, even the most general anisotropy class (triclinic) can be described using the matrix below instead of the full stiffness tensor.

$$(C_{ij}) = \begin{pmatrix} c_{1111} & c_{1122} & c_{1133} & c_{1123} & c_{1113} & c_{1112} \\ c_{2211} & c_{2222} & c_{2233} & c_{2223} & c_{2213} & c_{2212} \\ c_{3311} & c_{3322} & c_{3333} & c_{3323} & c_{3313} & c_{3312} \\ c_{2311} & c_{2322} & c_{2333} & c_{2323} & c_{2313} & c_{2312} \\ c_{1311} & c_{1322} & c_{1333} & c_{1323} & c_{1313} & c_{1312} \\ c_{1211} & c_{1222} & c_{1233} & c_{1223} & c_{1213} & c_{1212} \end{pmatrix} \tag{2.3}$$

The number of elastic coefficients is further reduced when the symmetry of a material is higher. In an isotropic solid, the elastic moduli ultimately reduce to two elastic constants λ and ν (Lamé coefficients) and the stiffness tensor components reduce to the following equations:

$$c_{ijkl} = \lambda\delta_{ij}\delta_{kl} + \nu(\delta_{ik}\delta_{jl} + \delta_{il}\delta_{jk}) \tag{2.4}$$

$$(C_{ij}) = \begin{pmatrix} \lambda+2\nu & \lambda & \lambda & 0 & 0 & 0 \\ \lambda & \lambda+2\nu & \lambda & 0 & 0 & 0 \\ \lambda & \lambda & \lambda+2\nu & 0 & 0 & 0 \\ 0 & 0 & 0 & \nu & 0 & 0 \\ 0 & 0 & 0 & 0 & \nu & 0 \\ 0 & 0 & 0 & 0 & 0 & \nu \end{pmatrix} \tag{2.5}$$

2.1.2 Hexagonal anisotropy

Hexagonal anisotropy (or radial anisotropy) is a common form of anisotropy in the earth's crust and occurs in layered material. Consider a stack of homogenous isotropic layers with different velocities (Figure 2.1). Due to the symmetry of the system the elastic moduli can

be described by five independent coefficients, A, C, F, L and N. If the system has x_3 as the axis of symmetry then an S-wave traveling in that direction will have properties that are independent of its polarisation. However, when waves travel in any other direction, the velocity depends on the propagation direction. The stiffness tensor components are then described by Equation 2.6.

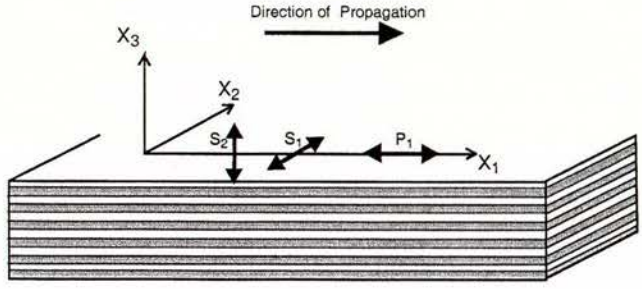

Figure 2.1 *Plane-waves propagating through an anisotropic medium where x_3 is the axis of symmetry.*

$$(C_{ij}) = \begin{pmatrix} A & A\text{-}2N & F & 0 & 0 & 0 \\ A\text{-}2N & A & F & 0 & 0 & 0 \\ F & F & C & 0 & 0 & 0 \\ 0 & 0 & 0 & L & 0 & 0 \\ 0 & 0 & 0 & 0 & L & 0 \\ 0 & 0 & 0 & 0 & 0 & N \end{pmatrix} \tag{2.6}$$

Next we will consider what happens to different waves that propagate through an anisotropic medium. We start with the elastodynamic equation in a homogeneous medium, which is expressed in Cartesian coordinates as,

$$\frac{\partial \sigma_{ij}}{\partial x_j} = \rho \frac{\partial^2 u_i}{\partial t^2} \tag{2.7}$$

where ρ is the density of the medium and u_i are components of the displacement vector $\mathbf{u}$. Equation 2.1 can be rewritten by applying Equations 2.2 and 2.7 to 2.7, to give

$$c_{ijkl} \frac{\partial^2 u_l}{\partial x_j \partial x_k} = \rho \frac{\partial^2 u_i}{\partial t^2} \tag{2.8}$$

The displacement vector **u** is described by the equation for particle motion,

$$\mathbf{u} = \mathbf{a} f\left(t - \frac{\mathbf{n}\cdot\mathbf{x}}{c}\right). \tag{2.9}$$

where c is the phase velocity, **n** is the normal vector in the direction of the plane wave propagation, **x** is the location of the particle at time t and **a** is the vector describing the amplitude and polarity of the wave. Using the derivatives of the displacement vector and the relationship expressed in Equation 2.8, one gets the eigenvalue problem:

$$m_{il}a_l = c^2 a_i \tag{2.10}$$

where m_{il} are elements of the Christoffel matrix,

$$m_{il} = \frac{c_{ijkl}n_j n_k}{\rho} \tag{2.11}$$

The vectors **a** are the eigenvectors of the Christoffel matrix and c^2 are the corresponding eigenvalues. To solve this problem in the case of hexagonal symmetry, consider the case of a wave propagating along the x_1 axis. Equation 2.11 can now be written as,

$$(m_{ij}) = \frac{1}{\rho}\begin{pmatrix} A & 0 & 0 \\ 0 & N & 0 \\ 0 & 0 & L \end{pmatrix} \tag{2.12}$$

where the diagonal terms are the eigenvalues of the matrix.

$$\lambda_1 = \frac{A}{\rho} \tag{2.13}$$

$$\lambda_2 = \frac{N}{\rho} \tag{2.14}$$

$$\lambda_3 = \frac{L}{\rho} \tag{2.15}$$

Therefore, three waves propagate along the x_1 axis with different velocities and polarisations. The velocities of the waves are described by the eigenvalues, while the eigenvectors give the directions of polarisation. The following equations are the velocities of the three different

waves in a medium where N>L, such as that which has plane layering with alternating high and low velocities, as in Figure 2.1.

$$P = \sqrt{A/\rho} \tag{2.16}$$

$$S_1 = \sqrt{N/\rho} \tag{2.17}$$

$$S_2 = \sqrt{L/\rho} \tag{2.18}$$

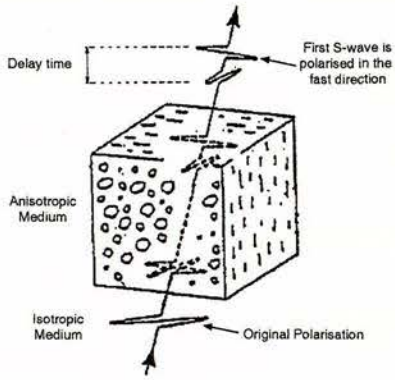

Figure 2.2 *Illustration of shear-wave spitting. As a shear-wave enters an anisotropic medium it is split into two orthogonal components that travel at different velocities.*

An S-wave propagating in this direction or any other in the x_1–x_2 plane will experience splitting as waves polarised in one plane will travel faster than waves polarised in the other plane (Figure 2.2). In the case of shear-wave splitting we measure two parameters, so that we can relate the phenomena to the anisotropy of the medium through which it travelled. Figure 2.2 shows the two parameters; the polarisation of the fast shear-wave (fast direction, ϕ) and the time difference between the fast and slow components of the shear-wave (delay time, δt).

If the S-wave propagation is in the x_3 direction (axis of symmetry) Equation 2.11 can be expressed as,

$$(m_{ij}) = \frac{1}{\rho}\begin{pmatrix} L & 0 & 0 \\ 0 & L & 0 \\ 0 & 0 & C \end{pmatrix} \tag{2.19}$$

and there are only two plane waves; one is polarised parallel to the propagation direction (the

P-wave) and the other perpendicular to the direction of propagation.

2.1.3 Causes of crustal anisotropy

The cause of anisotropy in the crystalline crust is often difficult to identify due to the crust's complex structure. Mineral alignment such as foliation in schist and shearing in fault zones is one possible cause for anisotropy. Okaya *et al.* (1995) investigated anisotropy of the Haast Schist near the Alpine Fault zone, New Zealand, and found that at elevated pressures shear-waves propagating parallel to the foliation travelled $\sim$1 km s^{-1} faster than waves propagating perpendicular to the foliation. This suggests that schist may contribute significantly to crustal anisotropy. Evidence from other metamorphic belts in Alaska, California and Vermont support this hypothesis (Godfrey *et al.*, 2000). Crustal anisotropy has also been linked with stress through the preferential alignment of cracks with the maximum compressive stress direction (Crampin, 1994). This hypothesis suggests crack compliance, such that only those cracks aligned with the maximum compressive stress direction will stay open and depending on the density of the cracks this can result in 1.5–10% differential shear-wave velocity anisotropy (Crampin, 1994). In many cases, however, distinguishing between stress-induced anisotropy and that due to mineral alignment in sheared fracture zones is difficult, especially if the direction of maximum compressive stress is subparallel to the plane of the fractures. This is an important issue for this project as we are trying to determine whether seismic anisotropy is stress- or structure-related. In the case of a weak fault, the direction of maximum compressive stress may be at a high angle to the strike of the fault ($>30°$), which makes it easier to distinguish between directions than if the fault were strong.

2.2 Focal mechanisms and stress

The following discussion on stress in the crust is based on descriptions by Zoback and Zoback (2002) and Stein and Wysession (2003).

2.2.1 Definitions and the stress tensor

If we are to describe the stress acting on a point in a homogeneous isotropic body, it is covenient to imagine an infinitesimally small cube and consider the forces acting on each surface. The traction is defined as the force acting over the area on which it is applied. This can be broken down into three components, one normal traction and two shear tractions (Figure 2.3). These components make up the stress tensor that can be represented by Equation 2.20,

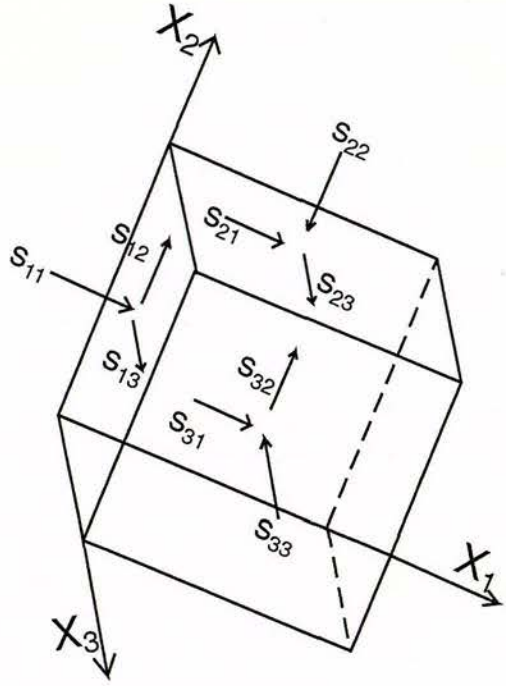

Figure 2.3 *Diagrammatic representation of the stress tensor in an arbitrary cartesian coordinate system.*

where the first subscript denotes the surface the traction is acting on and the second denotes the direction the traction is acting in.

$$\mathbf{S} = \begin{pmatrix} S_{11} & S_{12} & S_{13} \\ S_{21} & S_{22} & S_{23} \\ S_{31} & S_{23} & S_{33} \end{pmatrix} \tag{2.20}$$

We adopt the same convention as in geophysical literature, namely that compression is positive. The relationship between the effective and total stress is represented by the following equation:

$$\sigma_{ij} = S_{ij} - P_f \delta_{ij} \tag{2.21}$$

where S_{ij} is the total stress and σ_{ij} is the effective stress. For the cube to be in equilibrium, the following conditions must be true:

$$S_{12} = S_{21} \tag{2.22}$$

$$S_{13} = S_{31} \tag{2.23}$$

$$S_{23} = S_{32} \tag{2.24}$$

The most convenient coordinate system in which to consider stress is often the principal coordinate system (Figure 2.4), in which the stress tensor is diagonal (Matrix 2.25).

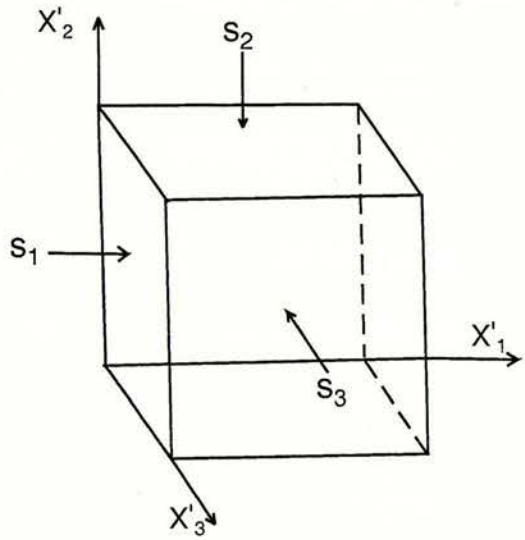

Figure 2.4 *This diagram shows the principal stresses. These are the result of a tensor transformation that eliminates shear stresses.*

$$\mathbf{S}' = \begin{pmatrix} S_1 & 0 & 0 \\ 0 & S_2 & 0 \\ 0 & 0 & S_3 \end{pmatrix} \tag{2.25}$$

Only six components of the stress tensor are independent, and these are all that are necessary to describe stress at depth. Another way of specifying the state of stress is using three principal stress magnitudes and three angles that transform the tensor from the principal stress coordinate system into a reference coordinate system. The stress tensor can be evaluated in any coordinate system by a tensor transformation using a rotation described by the direction cosines (Figure 2.5 and Equations 2.26 and 2.27).

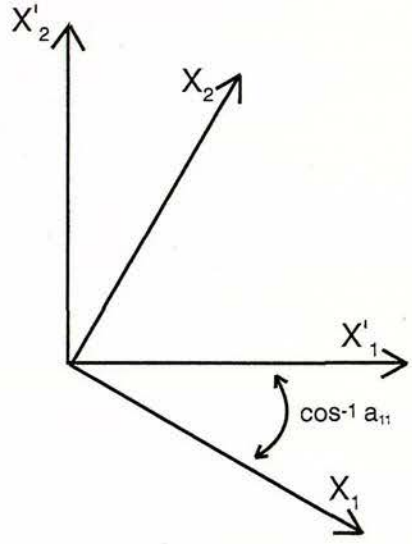

Figure 2.5 *Rotation of coordinate systems*

$$A = \begin{pmatrix} a_{11} & a_{12} & a_{13} \\ a_{21} & a_{22} & a_{23} \\ a_{31} & a_{23} & a_{33} \end{pmatrix} \tag{2.26}$$

$$\mathbf{S}' = A^T \mathbf{S} A \tag{2.27}$$

The relative magnitudes of the principal stresses are $S_1 \geq S_2 \geq S_3$. The earth's surface is a free surface and therefore cannot support shear stresses; this often simplifies analysis of the crustal stress tensor as one of the principal stresses is expected to be subvertical and the other two subhorizontal. Applying this assumption to the brittle crust allows one to describe stress at depth using four parameters: the magnitudes of the minimum and maximum horizontal compressive stresses, the vertical stress, and the azimuth of the maximum horizontal compressive stress. The vertical stress is presumed to be equal to the pressure of the overburden and therefore increases as a function of depth. When the stresses are not sub-vertical or sub-horizontal it is necessary to determine the azimuth of the axis of maximum compressive horizontal stress (S_{Hmax}), which is calculated in this study using an algorithm described by Lund (2000), and is equal to the normal stress on a vertical plane. To calculate this, we need to know the shape of the stress ellipsoid which is described by the stress ratio, R, and represented in the equation below:

$$R = \frac{S_2 - S_3}{S_1 - S_3} \tag{2.28}$$

When R=1 or 0 the intermediate stress is equal to either the maximum or minimum principal stress and when R=0.5 the intermediate stress is equal to half the maximum plus the minimum principal stress. Following the description given by Lund (2000) we can express the stress normal to the vertical plane as

$$-\mathbf{S_n} = (S_1 - S_3)[(S_{1N}n_N + S_{1E}n_E)^2 + (1-R)(S_{2N}n_N + S_{2E}n_E)^2]\mathbf{n^P} \qquad (2.29)$$

where S_{1N} and S_{1E} are the north and east components of the basis vectors in the S_1 stress direction, n_N and n_E are the north and east components of the normal vector and $\mathbf{n^P}$ is the plane normal in the principal stress coordinate system. The azimuth of the maximum or minimum horizontal stress (α) can be calculated by finding the stationary points of Equation 2.29 and is expressed by Equation 2.30.

$$tan2\alpha = \frac{2(S_{1N}S_{1E} + (1-R)S_{2N}S_{2E})}{(S_{1N}^2 - S_{1E}^2) + (1-R)(S_{2N}^2 - S_{2E}^2)} \qquad (2.30)$$

A test needs to be performed to calculate the relative magnitudes of the horizontal stress at each stationary point to determine whether α is the maximum (S_{Hmax}) or the minimum (S_{hmin}) horizontal stress.

Relative stress magnitudes and relation to faulting

The relative magnitudes of the maximum and minimum horizontal stress and the vertical stress can be related to faulting in the brittle crust using Anderson's theory of faulting (Anderson, 1951) and the Coulomb failure criterion (Byerlee, 1978). Anderson's theory of faulting related three endmember faulting regimes to specific relations of the principal stresses; normal faulting when $S_v = S_1$, strike-slip faulting when $S_v = S_2$ and reverse faulting when $S_v = S_3$ (Figure 2.6). For pre-existing faults to rupture requires the angle between S_1 and the strike of the fault to be $\sim 30°$ and Coulomb's frictional-failure criteria to be met. Coulomb's frictional-failure criteria is expressed by Equation 2.31;

$$\tau = \mu\sigma_n = \mu(S_n - P_f) \qquad (2.31)$$

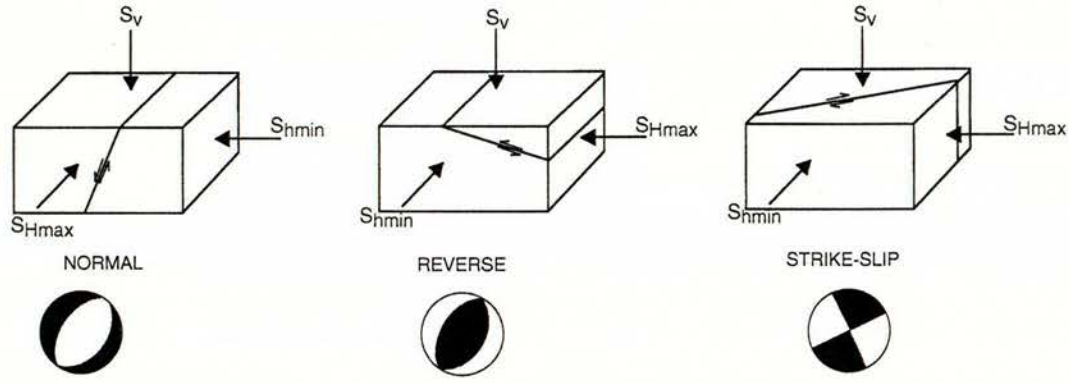

Figure 2.6 *Three types of faulting shown with relation to relative stress magnitudes, described by Anderson (1951). For normal faulting $S_v \geq S_{Hmax} \geq S_{hmin}$, reverse faulting $S_{Hmax} \geq S_v \geq S_{hmin}$ and strike-slip faulting $S_{Hmax} \geq S_{hmin} \geq S_v$. Below are the associated focal mechanisms where the shaded quadrant is compressional.*

where τ is the shear stress, σ_n is the effective normal stress, μ is the coefficient of friction and P_f is the pore fluid pressure.

When a fault is described as "weak" it means that the fault fails under a low ratio of shear stress to effective normal stress (a ratio <0.6), which cannot be explained by the hydrostatic pore fluid pressures and high coefficients of friction determined in laboratory experiments (Byerlee's friction of 0.6–1.0). The fault is therefore weaker than the surrounding crust, presumably because it has either a lower coefficient of friction or a higher pore fluid pressure (Equation 2.31). This is discussed in more detail in Section 4.4.

2.2.2 Stress indicators

A number of indicators can be used to determine various components of the crustal stress tensor. The World Stress Map project collates stress data from different sources and defined a grading system (Zoback, 1992). Hydraulic fracturing and borehole breakouts are the methods most commonly used to determine in situ stress, and are made from boreholes at depths greater than 100 m in order to avoid the effects of thermal stresses near the surface (Zoback and Zoback, 2002). Fault slip data and the orientation of igneous dykes are forms of geological data that are used, but they must be contemporaneous indicators, as they need to represent the most recent episode of deformation.

Focal mechanisms are an indication of the type of faulting that produces an earthquake.

They are determined by the polarity of a ray as it pierces the focal sphere or by a waveform inversion technique. P-wave polarities recorded by seismographs at different azimuths and distances are used to define compressional and dilatational quadrants of the sphere; the fault plane and auxiliary plane separate the quadrants. Examples of faults and their related focal mechanisms are shown in Figure 2.6.

A routinely employed method to determine stress is by inverting earthquake focal mechanisms. McKenzie (1969) demonstrates that a single focal mechanism alone puts little constraints on the stress tensor, as all that can be determined is that the axis of maximum compressive stress lies somewhere in the dilatational quadrant. Wallace (1951) and Bott (1959) hypothesised that slip on a fault plane will occur in the direction of maximum shear stress, which depends on both the orientation of the fault plane in the stress field and the relative sizes of the principal stresses. From this and the additional assumption that all motion on faults in a discrete volume of the crust are caused by the same stress tensor, it is possible to invert a group of fault slip data or fault plane solutions for the principal stress directions and the stress ratio. Lund (2000) explains that these inversions estimate four parameters of the stress tensor and that it is necessary to have at least four focal mechanisms to determine stress. Diversity of focal mechanism data is an important consideration when calculating the stress tensor and has been discussed in detail by Townend (2003). Focal mechanisms that are similar may appear to give a well constrained solution with some techniques but can actually be misleading, as seen by comparing the results with those from other techniques and also with a more diverse set of focal mechanisms.

2.2.3 Sources of stress

There are four main sources of stress that are discussed in relation to the earth's crust; these are: plate driving forces, topography, lithospheric buoyancy and lithospheric flexure (Zoback, 1992; Zoback and Zoback, 2002). Plate-driving forces differ depending on the tectonic regime; ridge-push forces act in mid-ocean spreading regions, while at transform boundaries there are forces resisting plate motion and at subduction zones there are a combination of slab-pull forces, slab-resistive forces, shallow collision forces and possibly suction forces. Topography also contributes to stress, such that crustal thickening, which results in

a positive density anomaly at the surface, generally produces extensional stresses and the opposite is true for crustal thinning. Stresses from lithospheric flexure are due to the emplacement (extensional stresses) or removal of loads (compressional forces) such as glaciers, sedimentary basins and volcanic edifices or by bending of the down-going plate at a subduction zone.

2.2.4 Stress inversion algorithms

Algorithm	Input data	Type	Notes	Developer
SLFAST	F.mech	Linear	Computationally efficient. Uses bootstrap resampling to determine confidence limits.	Michael (1984) Michael (1987)
FMSI	F.mech	Grid search	Performs a grid search over the four stress parameters. The best model is that with the smallest rotation necessary to match the predicted and observed slip directions.	Gephart and Forsyth (1984) Gephart (1990)
MOTSI	F.mot	Grid search	Performs a grid search over the four stress parameters, but uses a different definition of misfit to that of FMSI.	Abers and Gephart (2001)
GETSTRESS	F.mot	Grid search	Assumes a coefficient of friction. Performs a grid search over S_1 and S_3. Uses a resampling technique to define confidence limits.	Robinson and McGinty (2000)

Table 2.1
Summary of the stress inversion algorithms. "F.mech" stands for focal mechanisms and "F.mot" for first motion data.

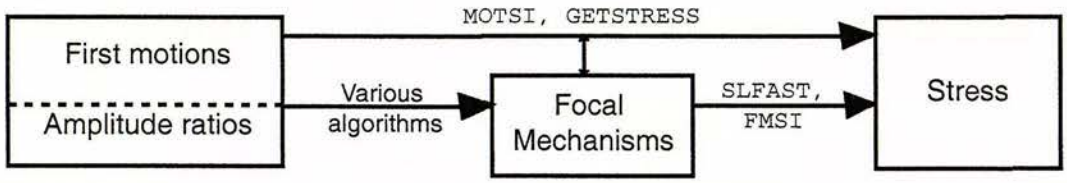

Figure 2.7 *Schematic representation of obtaining stress from different input data. First motions from a number of stations are used to define a focal mechanism for an event. Many events are then used in an inversion for the stress tensor.*

Here we introduce the inversion algorithms and discuss their different assumptions, constraints and error analysis. The aim of all stress inversion algorithms is to find the set of

stresses that is most consistent with all the focal mechanisms. Table 2.1 summarises the basic information regarding each algorithm's input data and characteristics. The common method of determining the stress tensor is by performing a grid search over all four stress parameters (S_1, S_2, S_3 and R), then choosing the stress model that best fits all the focal mechanism data. Figure 2.7 is a schematic representation of the process for obtaining stress from different types of input data, as two of the algorithms use focal mechanisms and two use first motions directly. The definition of the misfit, between the stress model and the focal mechanism data, varies between algorithms.

SLFAST (Michael, 1984; Michael, 1987)

SLFAST was developed by Michael (1984) for the inversion of slickenside data and was later extended to focal mechanisms (Michael, 1987). A unique feature of this inversion is that it behaves linearly by making the simplifying assumption that, on each plane that ruptures, the magnitude of shear traction is similar. The key benefit of linearizing the inversion is that it is computationally efficient and makes it easy to calculate confidence limits. Two assumptions are required to compute the stress parameters; the first is that the stress field is uniform throughout the crustal volume represented by the data; and the second, that the shear traction on the fault plane is parallel to the slip direction. A problem with all inversions using focal mechanisms is that the fault plane cannot be distinguished from the auxiliary plane. Michael (1987) tried to account for this problem by using both planes and applying bootstrap statistics to the inversion results. This attempts to quantify the uncertainties involved in determining the fault plane.

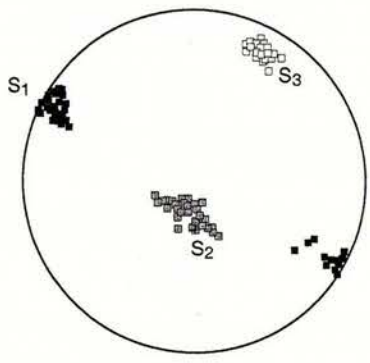

Figure 2.8 *An example of the output from SLFAST. The squares represent models that lie within the 95% confidence limit of the best solution. The shading of the squares indicates the principal stress directions, S_1 (black), S_2 (grey) and S_3 (white).*

FMSI (Gephart and Forsyth, 1984; Gephart, 1990)

FMSI (Focal Mechanisms Stress Inversion) was developed by Gephart and Forsyth (1984) for fault slip data and later modified for focal mechanisms (Gephart, 1990). It determines the best-fitting principal stress directions and relative stress magnitude parameters by performing a grid search over all four resolvable stress parameters. The best stress model identified from the grid search is the one that requires the smallest total rotation of all fault planes to align the predicted and observed slip directions. If the fault plane is not known, the algorithm samples both nodal planes with respect to each stress model and calculates the misfit of each, then uses the plane that is most consistent with the best stress model. The method does not make any additional constraints based on the failure criterion of faults, and in principle allows faults to be weak. All inversions performed with this code use a 10° grid search.

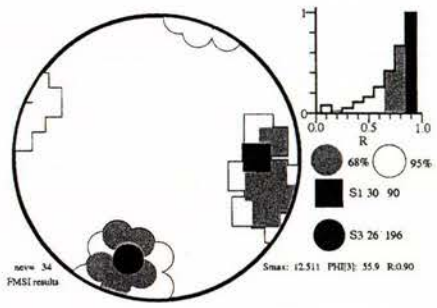

Figure 2.9 *An example of the output from FMSI. The squares represent S_1 solutions and the circles S_3. The best solution is in black and solutions within the 68% and 95% confidence intervals in grey and white respectively. Values of R are also indicated in the histogram where the shading has the same meaning as for the stress orientations.*

MOTSI (Abers and Gephart, 2001)

The MOTSI inversion code was developed by Abers and Gephart (2001) and differs from the two inversions described above in that it calculates the stress tensor from first motion data rather than focal mechanisms. First motions may be compatible with a large number of focal mechanisms that are not taken into account in the previous inversions and could lead to underestimates of the uncertainty. By inverting directly from first motions, the stress tensor can then be used to constrain the focal mechanisms. This inversion is similar to FMSI (Gephart, 1990) as it also uses a grid search to determine the four stress parameters (refer to Section 2.2) but it also adds an additional search for the focal mechanism. For each stress model, a search is performed over a grid of fault planes and identifies for each event the focal mechanism that best fits the first motion data, avoiding those that are inconsistent with

the stress model. The uncertainties resulting from this type of inversion depend on the data distribution and the reliability of the first motions. Other errors considered in this method are related to the incomplete coverage of the focal sphere, which may result in poorly constrained focal mechanisms, and whether there is an incomplete range of fault planes, which may produce a large number of stress models that fit the focal mechanisms (using `MOTSI-1sm` code). To be consistent with the `FMSI` algorithm, a 10° grid search was also used for this inversion method.

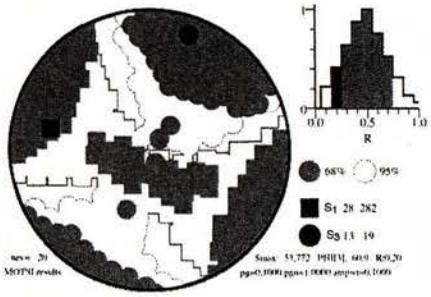

Figure 2.10 *An example of the output from* `MOTSI`*. The squares represent* S_1 *solutions and the circles* S_3*. The best solution is in black and solutions within the 68% and 95% confidence intervals in grey and white respectively. Values of R are also indicated in the histogram where the shading has the same meaning as for the stress orientations.*

`GETSTRESS` (Robinson and McGinty, 2000)

Like `MOTSI`, `GETSTRESS` is another inversion algorithm that inverts first motions for stress. It was developed by Robinson and McGinty (2000) so that data from small aftershocks that did not define a focal mechanism could be included in a stress inversion. The method searches over a range of S_1 and S_3 orientations that define two fault planes which are optimally oriented to fail, using the assumption that the coefficient of friction defines the angle between the two planes and S_1. All earthquakes are assumed to occur on one or other of the planes and slip is assumed to be in the direction of resolved shear stress. This technique uses the Coulomb failure criterion to constrain the number of possible stress models and therefore the coefficient of friction must be defined. Since an objective of this study is to investigate the frictional strength of faults, we do not want to make this assumption and therefore `GETSTRESS` was not used in this study. However, since this method has already been used by McGinty *et al.* (2000) in the Marlborough region, their results are used as a comparison.

CHAPTER 3

SEISMIC ANISOTROPY

3.1 Introduction

We have used several different data sets to study crustal anisotropy in the Marlborough and Wellington regions. The purpose of this study is to investigate anisotropy in the region and determine whether it is related to the stress field or to geological structure.

Initially we used data from an experiment conducted by both the University of Colorado and Victoria University of Wellington (CU/VUW), which deployed twelve 3-component broadband seismographs, most of which had an accompanying array of short-period instruments. The processing of this data involved shear-wave splitting analysis on ten broadband stations and one short-period array (ALI00) containing ten seismographs. Figure 3.1 shows the locations of the instruments from which data were collected for shear-wave splitting analysis.

GNS (Institute of Geological and Nuclear Sciences) deployed a temporary network of thirty-nine short-period seismographs covering northern South Island, including two stations in the lower North Island (Figure 3.1; orange inverted triangles). Reyners *et al.* (1997) and Eberhart-Phillips and Reyners (1997) used these stations for other studies on crustal structure, but this is the first time shear-wave splitting analysis is being performed on the data. As time was limited for this project and the deployment was very large (39 original stations), only sixteen stations and events with corresponding focal mechanisms were chosen for shear-wave splitting analysis. We confirm that the anisotropy is not related to a source effect by comparing the initial polarisation from the shear-wave splitting code with that calculated from focal mechanisms.

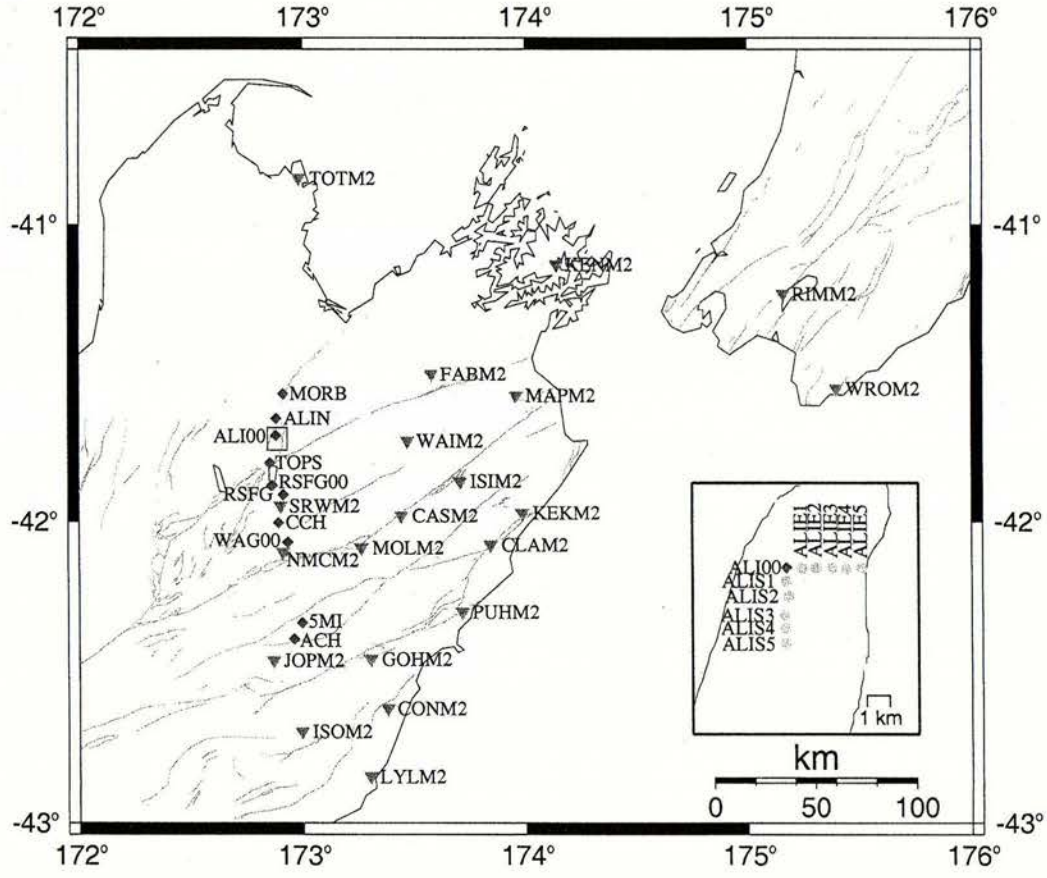

Figure 3.1 *Locations of stations used for shear-wave splitting analysis. Green diamonds are the CU/VUW Broadband stations, yellow dots are the CU/VUW short period stations and the orange inverted triangles are the GNS short period seismometers*

3.2 Data selection

There are three important criteria on which the data were selected and graded. The first of these is hypocenter depth; since the objective is to look at crustal anisotropy it is important to look at earthquakes whose ray paths travel through the crust (Section 3.2.1). The second is the shear-wave window, which is defined by incidence angles less than 45°; this is to avoid scatter and other converted phases (Section 3.2.2). The third is signal-to-noise ratio, to remove any poor quality data (Section 3.2.3).

3.2.1 Depth-dependance of observations

Shear-wave splitting measured on a wave recorded at the surface reflects the anisotropic media it is exposed to along its path length, from source to receiver. To study crustal anisotropy it is necessary to eliminate contamination from sources of anisotropy elsewhere, such as crystal alignment of olivine in the upper mantle. A simple way of doing this is by looking only at earthquakes that occur in the crust. From seismological studies, the crust is 20–25 km (Robinson, 1986) and 15–20 km (Eberhart-Phillips and Reyners, 1997) thick in Wellington and Marlborough respectively.

Most of the earthquakes we used had depths of 50 km or less; this limit is greater than the thickness of the crust because a shallower limit would significantly reduce the data set at many stations. It is also acceptable as the majority of the path length is travelling through the crust. At one station (WAG), data were analysed for earthquakes with depths of 50–100 km so that the results might be compared with those of Audoine *et al.* (2000). WAG was chosen for this purpose since it had the largest number of usable events and the longest deployment time.

3.2.2 Importance of the shear-wave window

If the shear-wave arrives at the surface with an incidence angle greater than the critical angle (35–45°) it can be distorted due to P-S conversion causing an associated phase change on the radial and transverse components (Nuttli, 1961; Evans, 1984). The critical shear-wave angle is calculated using Equation 3.1, where the the V_s/V_p ratio for near-surface crustal rocks is $\sim 1/\sqrt{3}$, which yields an angle of 35°.

$$i_c = arcsin\left(\frac{V_s}{V_p}\right) \tag{3.1}$$

Shear-waves arriving at an angle larger than this result in elliptical particle motion, which can be misinterpreted as shear-wave splitting. However, Paulssen (2004) argued that this is not always the case and that results with shallower incident angles may have components of both transverse isotropy and azimuthal anisotropy. Paulssen's (2004) results show delay times larger than half the dominant period and therefore the time difference cannot be ex-

plained by a phase change at the free surface. This suggests that shallower incident angles may be used with caution.

Incidence angles were determined by first calculating the ray parameter (p). This was done using the GNS locations and the IASPEI velocity structure using the code from Buland and Chapman (1983). The incidence angle (i) was then determined using the equation below.

$$i = sin^{-1} \frac{pV_s}{111} \tag{3.2}$$

In this case the near-surface shear-wave velocity (V_s) used was 2.65 kms^{-1} (as used previously by Audoine *et al.* (2000) and in agreement with the P-wave velocity and V_p/V_s ratio obtained by Eberhart-Phillips and Reyners (1997)). The results of calculating the ray parameter and incidence angle are listed in the tables in Appendix B.

Earthquake locations were obtained from GEONET quake search (http://data.geonet.org.nz/QuakeSearch/). The search looked for earthquakes within a 100×100 km square, centred on each station. This is approximately the shear-wave window (35–45°angle of incidence) at 50 km depth. The waveform data were requested from the IRIS (Incorporated Research Institutions for Seismology) data centre (http://www.iris.edu/SeismiQuery) for the CU/VUW deployment and from GEONET for the GNS deployment.

3.2.3 Quality of the data

The arrivals were sorted into three categories depending on the quality of the records; "discard" for disrupted records, "noisy" for possibly usable records, and "good". Many events had to be discarded due to irremovable noise that, according to the field records, was caused by cattle destroying cables and most of the time led to equipment failure. This affected recording at almost every station in the CU/VUW deployment. However if only the vertical component was affected then the horizontal components were still used for splitting analysis.

Frequency filters were designed and applied to the individual records using a SAC (Seismic Analysis Code) macro developed by Gerst (2003), which allows the user to view different filters before writing new filtered files. Filtering improved the signal to noise ratio and was chosen so that the S-wave arrival was most impulsive. Records that did not show a

clear S-wave arrival after filtering were discarded. We used Butterworth bandpass frequency filters with corner frequencies of 0.1–3 Hz and 2–6 Hz.

3.3 Data processing

Initially two methods were used for determining shear-wave splitting measurements, a manual method (Gerst, 2003) and an automated method (Teanby *et al.*, 2004) (Figure 3.2). Both methods produced similar results and since the automated method also gives an indication of the stability of the result it was used for the rest of the processing. All processing was done using SAC (Tapley *et al.*, 1990).

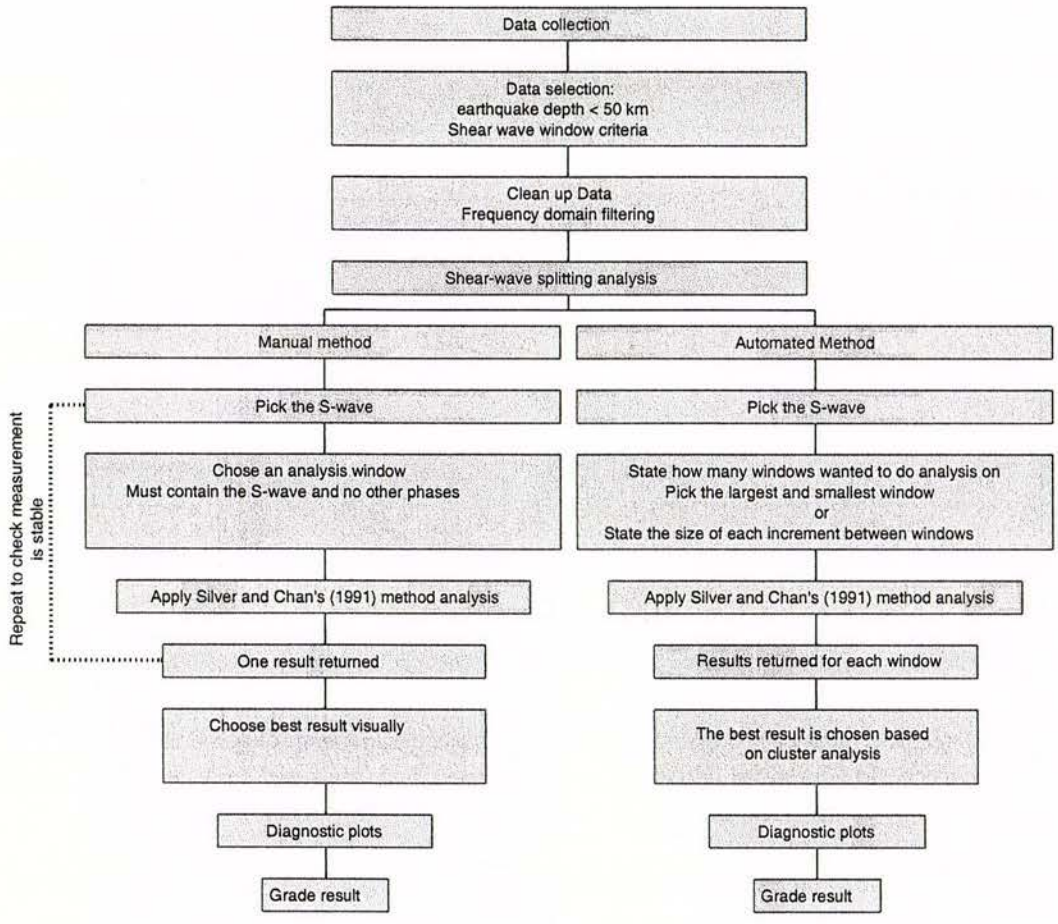

Figure 3.2 *Flow diagram comparing manual and automated shear-wave splitting analysis techniques.*

3.3.1 Automated shear-wave splitting technique

We used the automated S-wave splitting technique developed by Teanby *et al.* (2004) to analyse the data. Most shear-wave splitting programs involve manually picking the analysis window. This creates some uncertainty as the measurement may change over different windows. Teanby *et al.* (2004) developed an algorithm that performs splitting analysis on a range of window lengths and positions, and then picks the window with the most stable measurement, therefore reducing the uncertainty in the stability of the measurement. Cluster analysis is used to find the most stable measurement.

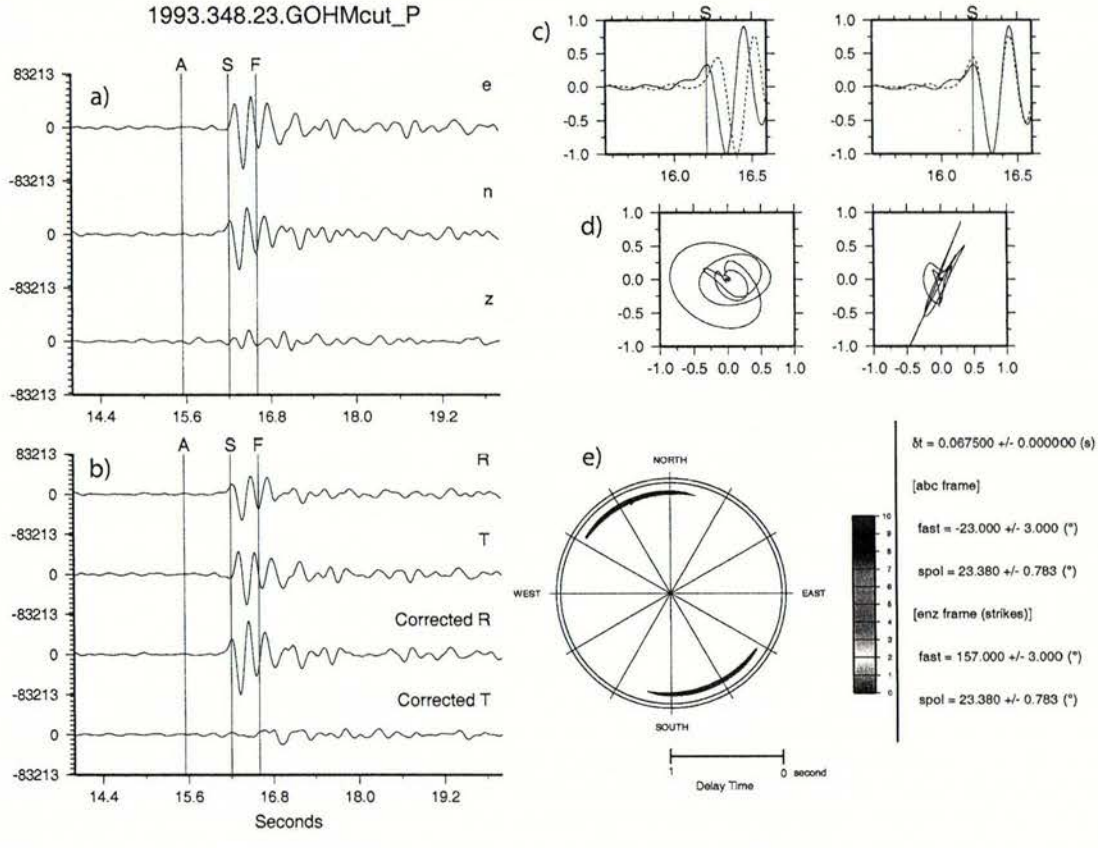

Figure 3.3 *Diagnostic plots of a single shear-wave splitting measurement. Original east, north and vertical components (a) are rotated into radial and transverse components and corrected for splitting (b). The fast and slow component of the shear-wave before and after splitting is shown in (c) along with the associated particle motion (d). The error surface, which is contoured according to confidence regions (1 is the outline of the 95% confidence region), and the solutions statistics are shown in (e).*

Each earthquake recorded at a given station is run through the automated shear-wave

splitting program. First the shear wave arrival is picked, displayed in Figure 3.3a as the line marked S. Then a window is defined around the shear wave (Figure 3.3a between lines A and F) and the Silver and Chan (1991) method of determining splitting measurements applied. Particle motion will be elliptical if anisotropy is present (Figure 3.3d, left). A grid search is performed over the fast direction and delay time. Both components are rotated by the fast direction and one component is lagged by the delay time. The eigenvalues of the corrected covariance matrix of particle motion are a measure of the linearity. When searching for the best result the program looks for the ϕ and δt pair that has the smallest second eigenvalue and therefore the most singular corrected covariance matrix. Then an F-test is performed to calculate the 95% confidence interval, as described by Silver and Chan (1991). These steps are then repeated for more windows. Any number of windows can be chosen, but the running time of the program strongly depends on the number of windows. The bounds of the windows are either defined manually by picking the maximum and minimum window size, or automatically by stating the size of the increments at the start and end of the window. In this study 50 windows were used, varying the start of the window by 2 increments and the end of the window by 25 increments. The program then returns a measurement for each window, which is displayed in diagnostic plots (Figure 3.4).

Cluster analysis is then used to determine the optimum result, which is defined to be that with the lowest error in the cluster with the lowest variance (see Teanby *et al.* (2004) and Section 3.3.2).

The program produces a series of diagnostic plots (Figure 3.3 and Figure 3.4) that are used to evaluate the stability of the result. The measurement is considered reliable if it fits the following criteria, which are based on visual checks of the plots:

- The energy on the component orthogonal to the incoming polarisation direction that has been corrected for splitting is minimised (Figure 3.3b).
- The fast and slow waveforms are similar and correlated after correcting for splitting (Figure 3.3c).
- As mentioned on pages 36–37, particle-motion is elliptical before and linear after the correction (Figure 3.3d).

- The error surface has a unique and well-defined solution (Figure 3.3e), as unstable events often exhibit multiple highs.

- The "window plot" exhibits a plateau containing many points of low error; one point on the plateau should be the solution (Figure 3.4f).

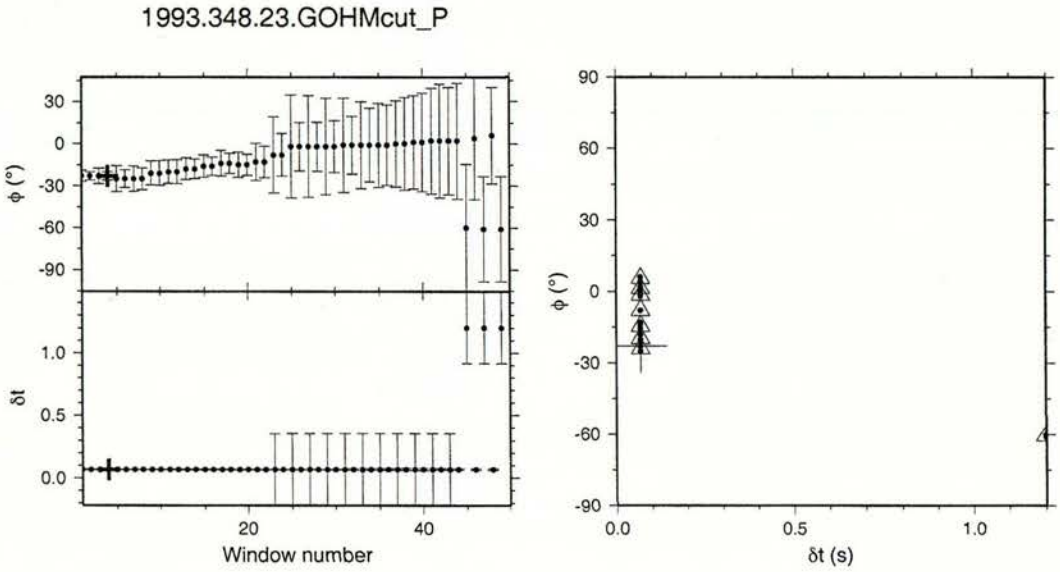

Figure 3.4 *Diagnostic plots from the cluster analysis. On the left are the results from all windows on which shear-wave splitting analysis was performed. On the right are the clusters (triangles) and solutions from each window. The best solution is indicated by a cross in both plots.*

Finally, with the processing completed, each event is given one of five grades, A, B, NULLA (where there is no defined delay time and there are two fast directions at 90° from each other), NULLB (when the delay times are not defined and there is one fast direction) and unusable (when there is no stable solution). An A quality result is one that fits all of the above criteria, while a B quality measurement fits a majority of the criteria.

3.3.2 Cluster analysis and identification of the result

This is an overview of the technique described in more detail by Teanby *et al.* (2004). We have used this automated technique so that we can be confident that the result chosen is stable over many windows. One can assume that the most reliable measurement will reside

in a cluster of many similar measurements. Below we describe the method of determining the best cluster and therefore the best measurement.

After the splitting measurements have been obtained for each window, cluster analysis is applied to the results. An essential part of cluster analysis is the calculation of the distance between measurements in the "measurement space". Each measurement of shear-wave splitting has two components, a fast direction ϕ and delay time δt; since these variables have different scales a correction must be made so that they are weighted equally. Then we can begin the cluster analysis. Initially each measurement is considered to constitute its own cluster and the inter-cluster distances are calculated, taking into account the periodicity of ϕ. The two closest clusters are then combined, resulting in one fewer cluster. This is repeated until all the data points are in one cluster, leaving a hierarchy of clusters. For each cluster defined throughout the process, the number of data points and the average location within the cluster is noted.

The next step is to find the optimal number of clusters. The best results will be in the stable plateau region and will relate to tight clusters with a large number of data points, so it can be assumed that these will be found first in the hierarchy. This means that clustering can be stopped after certain conditions are reached. The stopping criteria is based on two methods explained in Teanby *et al.* (2004), one involving the within-cluster variance and the between-cluster variance and the other involving the ratio of the within-cluster variance when two clusters are merged.

Once the optimum number of clusters is determined, the best cluster is selected. This is based on the number of points in the cluster and the variance within the cluster $var_{c_j}^2$. An overall variance $var_{o_j}^2$ is defined as $\max(var_{c_j}^2, var_{d_j}^2)$, where $var_{d_j}^2$ is the mean data variance. The best cluster is that for which $var_{o_j}^2$ is smallest; this avoids the selection of tight clusters with high errors and diffuse clusters with small errors. The best measurement can then be chosen from the best cluster as the one with the lowest variance.

One concern with this technique is that NULL measurements are considered an unstable result due to their large uncertainty in delay time. Instead a result may be chosen that has a poor waveform correlation or non-linear particle motion after the correction for splitting. This problem is surmountable by manually checking and grading the results.

3.4 Results

The consistency of results between stations is strongly dependent on the spacing between stations. The delay times are very similar throughout the study (~0.1 s), but the fast directions show some variation.

3.4.1 Statistics

The fast direction is directional data with 180° periodicity; therefore typical error statistics cannot be applied. Instead, each fast direction measurement is taken as a vector. The vectors are added together and divided by the number of measurements, to produce the resultant vector (equation 3.3). We can then calculate the mean (equation 3.4) and standard deviation (equation 3.5) as described by Mardia (1972). The fast direction must be doubled to allow for the bimodal distribution due to the 180°periodicity.

$$\mathbf{R} = \begin{pmatrix} \frac{1}{n}\sum_{i=1}^{n}\cos(2\Phi_i) \\ \frac{1}{n}\sum_{i=1}^{n}\sin(2\Phi_i) \end{pmatrix} \tag{3.3}$$

$$\bar{\phi} = \frac{1}{2}\arctan\left(\frac{1}{n}\sum_{i=1}^{n}\sin(2\Phi_i) \Big/ \frac{1}{n}\sum_{i=1}^{n}\cos(2\Phi_i) \right) \tag{3.4}$$

After calculating **R**, Rayleigh's test for non-randomness is applied (Mardia, 1972). By consulting tables given by Mardia (1972), one can say to what degree of confidence the data is non-random. The Rayleigh test for non-randomness was applied to the fast direction data from each station as well as for averages within each deployment. The data from the CU/VUW broadband and short-period deployments showed a high degree of non-randomness (> 90% confidence) while the results from the GNS deployment were more random (Table 3.4.1). This is likely to be due to the spacing between the stations and the variation in raypaths causing different regions to be sampled. The mean direction of the data is the direction of the resulting vector and is calculated using Equation 3.4. The spread of the data is related to the length of **R** (r), and the more inconsistent the data the smaller the vector, therefore if r equalled 1 the all measurements would be aligned. The standard deviation can

be calculated by equation 3.5,

$$s = \sqrt{-2ln(1-S_0)} \tag{3.5}$$

where S_0 is the circular variance defined by:

$$S_0 = 1 - r \tag{3.6}$$

Statistical analysis was applied to each of the stations with more than one result using a program by Gerst (2003) and is presented in tables in the following sections. Stations with fewer than five measurements or with a low degree of non-randomness (< 90%) are marked by a star. The overall results for each deployment are presented in Table 3.1.

Deployment	$\overline{\phi}$	$\pm\phi$	$\overline{dt}$	$\pm dt$	#	r	Confidence
CU/VUW SP	49.6	35.5	0.15	0.09	34	0.47	99.9%
CU/VUW/BB	84.2	50.7	0.11	0.09	70	0.21	95%
GNS*	63.4	52.4	0.124	0.09	39	0.19	<90%

Table 3.1

Overall mean and standard deviation of fast direction ($\overline{\phi} \pm \phi$) and delay time ($\overline{dt} \pm dt$) from each deployment. The number of A and B quality measurements (#) used, the length of the resultant vector and the confidence that the results are not random, is also given.

The results of the shear-wave splitting analysis are presented separately for each deployment in the following sections. First however we will discuss Fresnel zones as they pertain to the regions sampled by each deployment.

3.4.2 Fresnel zones

The Fresnel zone is the region at depth that is sampled by incoming rays. The radius of the first Fresnel zone (F) is calculated using Equation 3.7 (Sheriff and Geldart, 1995) and is dependent on the wavelength of the wave (λ) and the depth of interest (z).

$$F = \sqrt{\frac{\lambda z}{2}} \tag{3.7}$$

To make these calculations we used a one-dimensional velocity model suggested by Eberhart-Phillips and Reyners (1997) and used a frequency range of 1–4 Hz. To calculate the extent

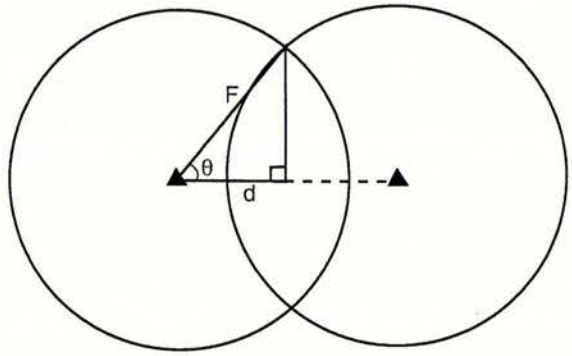

Figure 3.5 *Geometry of overlapping Fresnel zones used to calculate the percentage of overlap.*

to which the Fresnel zones from adjacent stations overlap, we used the method described by Matcham (1997). The percentage overlap is that of two overlapping circles (Figure 3.5 and calculated using Equation 3.8.

$$\%Overlap = \frac{2}{\pi}\left(cos^{-1}\left(\frac{d}{F}\right) - \frac{d\sqrt{F^2-d^2}}{F^2}\right) \tag{3.8}$$

3.4.3 CU/VUW broadband array

We requested 267 records for earthquakes from 0–50 km depth and within 50 km distance from the respective stations, of which 168 were processed and 81 produced usable results. Measurements from the broadband array show a variety of fast directions and delay times. The data are displayed in two different ways: as rose diagrams (Figure 3.6) and by plotting the splitting result half-way between the source and receiver (Figure 3.7). There appear to be two principal directions, one being fault-parallel with an average fast direction of 50–80° and the other that is evident at four stations (5MI, CCH, RSF00 and MORB) has an average fast direction of 300°to 330°. The changes between the two fast directions can occur between two closely spaced stations as is the case between stations 5MI and ACH (Figure 3.6). The Fresnel zone at each station is 5–11 km in radius at 50 km depth, which is less than the spacing between them, indicating there is some overlap. For example, stations in this array that are ~12 km apart would have Fresnel zones that overlap by 33% at 50 km depth and

wouldn't overlap for depths shallower than 15 km. We conclude that the broadband stations, such as 5MI and ACH, may be sampling the same regions in the crust, if the earthquakes are deeper than 15 km; and variations between stations are probably due to lateral changes in the top 15 km of the crust.

Station	$\overline{\phi}$	$\pm\phi$	$\overline{dt}$	$\pm dt$	#	r	Confidence
MORB*	-61.0	38.8	0.19	0.06	5	0.40	<90%
ALIN*	39.7	38.3	0.15	0.11	4	0.41	<90%
ALI00	51.3	24.7	0.22	0.14	5	0.69	90%
TOPS	38.8	23.9	0.14	0.07	7	0.70	97.5%
RSF00*	-87.2	13.0	0.14	0.06	3	0.90	<90%
RSFG	74.2	34.5	0.06	0.02	10	0.49	99%
CCH	-44.0	33.2	0.09	0.06	9	0.51	90%
WAG	85.2	26.0	0.10	0.08	12	0.66	99%
5MI	-34.0	30.2	0.07	0.08	12	0.57	97.5%
ACH*	65.7	4.1	0.10	0.06	3	0.99	<90%

Table 3.2

Mean and standard deviation of the results for each station in the CU/VUW deployment of broadband instruments. The # is the number of measurements and r is the length of the resultant vector.

Since the anisotropic medium could be anywhere along the path length, it is also helpful to look at Figure 3.7 in which the measurement is shown half-way between the source and receiver. The length of the bowties is related to the delay time and the angle is related to the uncertainty in the result. Some stations show the fault parallel fast direction more strongly than others and their measurements tend to have ray paths that travel through major faults before reaching the station (e.g. ALI, TOPS and ACH). This suggests that the anisotropy is controlled by geological structures that are near the station.

At station WAG, events with depths of 50–100 km were also analysed. The results (Figure 3.8) show that the fast direction varies with depth and is similar to that of previous studies (Audoine, 2002). Fast directions from events at depths of 0–50 km appear bimodal with a primary direction of 80° and a secondary direction at ~300°. For events at depths of 50–100 km the predominant trend is north–south. Errors from these deeper measurements suggest there is more variation in the fast direction, but the region defined by the standard deviation does not overlap with those from the shallower events. Figure 3.8 shows there is an increase in maximum delay time for events deeper than 70 km, however there are still small delay

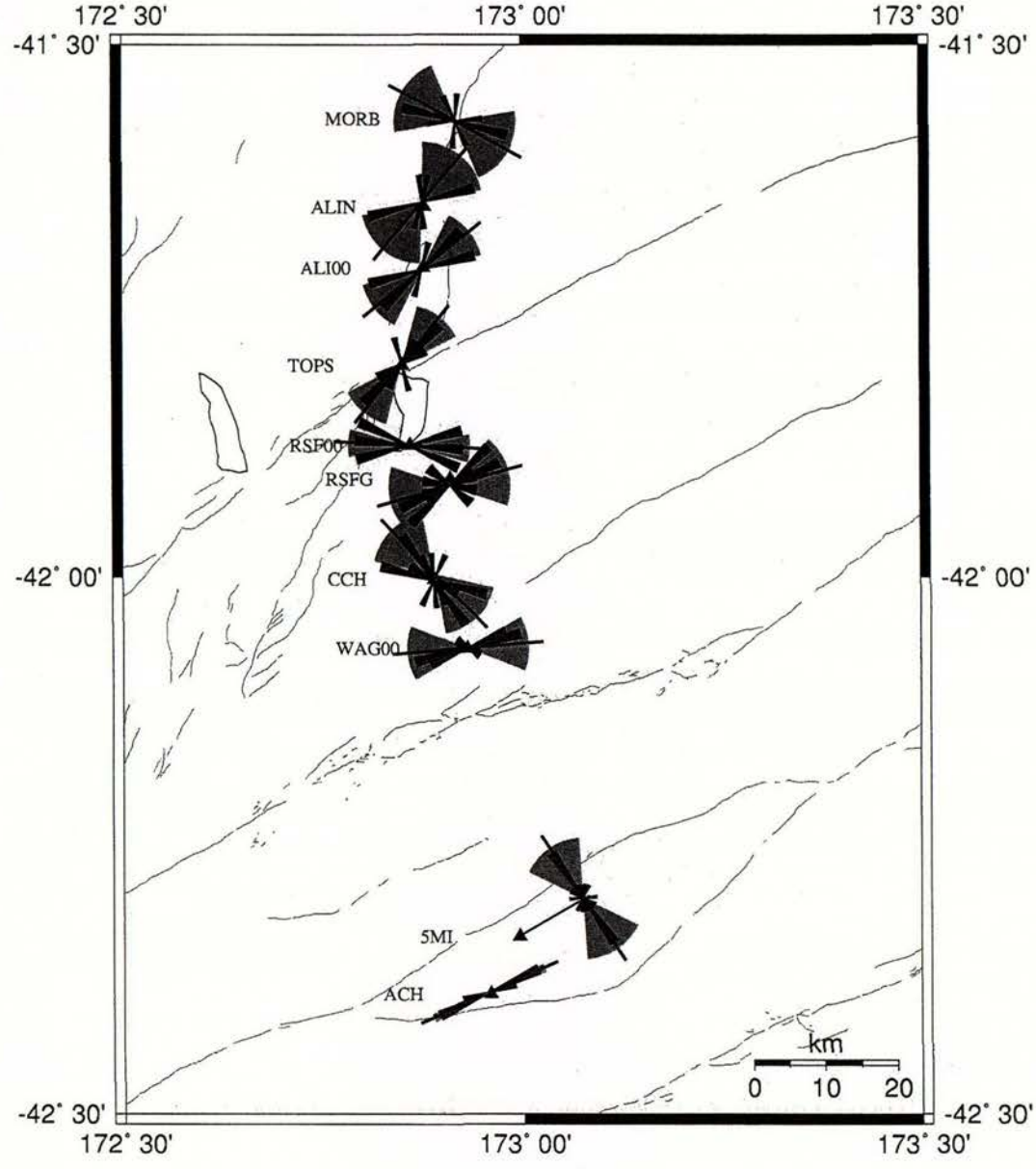

Figure 3.6 *Rose diagrams of the fast direction at each station in the broadband array. Includes the mean (red) and standard deviation (light blue).*

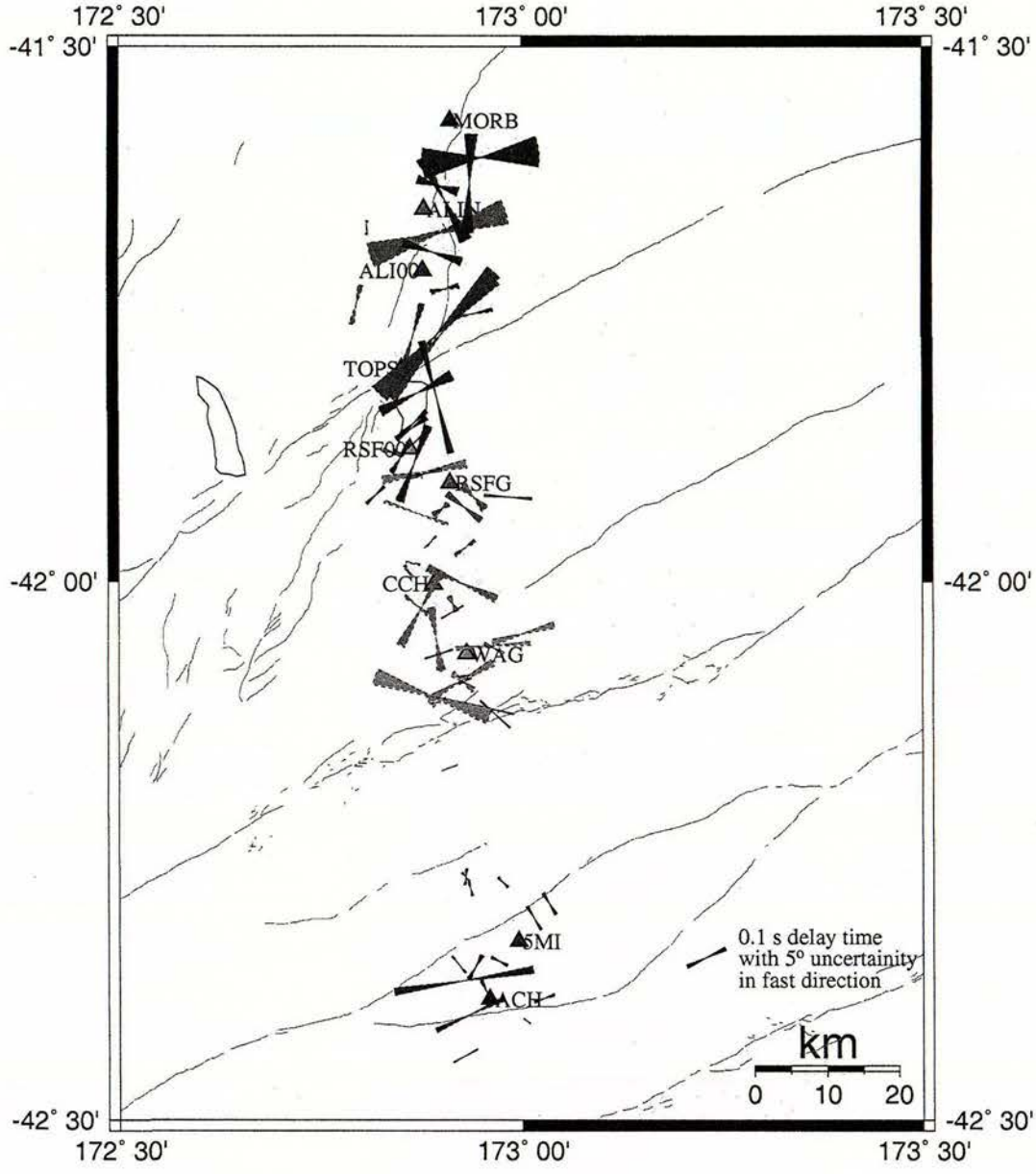

Figure 3.7 *Shear-wave splitting results for the broadband stations of the CU/VUW deployment. Measurements are projected to half-way between the hypocenter and station. Results with bold outlines are A quality and those with dotted outlines are B quality (see text). The length of the bowtie is scaled linearly according to the delay time, while the direction and the angle correspond to the fast direction and its uncertainty respectively. The measurements are the colour of the corresponding station.*

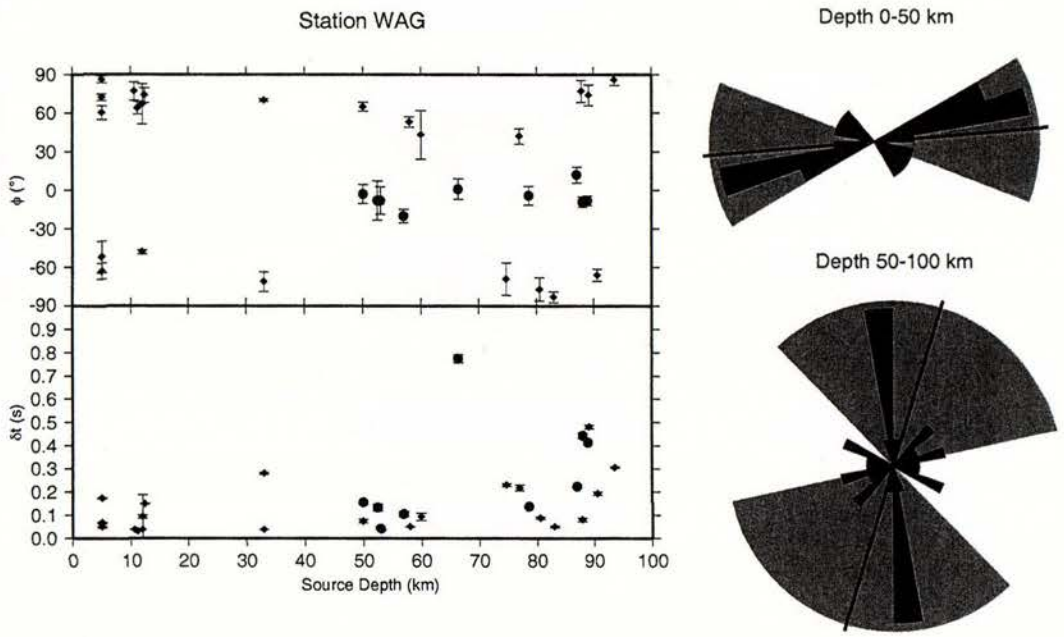

Figure 3.8 *Shear-wave splitting results at WAG. The rose diagrams show the variation of fast direction for events grouped by depth (right), while on the left is a graph displaying the splitting measurements with depth (red dots indicate hypocenter depths greater than 50 km that are also north-trending)*

times. The variation of both fast direction and delay time from events deeper than 50 km suggests incoming rays may be resplit due to multiple sources of anisotropy from the mantle and the crust.

3.4.4 CU/VUW short-period array

The fast-directions are fairly consistent across the short-period array and with the associated broadband seismograph, ALI00 (Figures 3.6 and 3.9). The spacing between stations is 0.5–1 km, which is less than the radius of the Fresnel zone (4 km) at 10 km depth, therefore the measurements sample similar regions. The percentage of overlap of Fresnel zones from adjacent stations is 70% at 3 km depth. Some of the stations only have a couple of usable measurements (E1, E2, E3 and E4), but the results at these stations are generally similar to those at stations with a large number of measurements (ALI00 (broadband), S3 and S4). Fast directions from two stations (S1 and S2) trend northwest but only a few usable events were recorded at each station and more would be needed to establish whether this is representative of the overall result for the station. Combining the measurements from all the stations results

in an average fast direction of 50° (Figure 3.9 and Table 3.3). This result is consistent with a study of shear-wave splitting from SKS phases on the same array (Köhler, 2003). The broadband station from Köhler's (2003) study, ALI00, has a fast direction that is north-trending and similar to Audoine *et al.*'s (2000) result from local S phases on a station THZ that is ~35 km away (Audoine, 2002).

Station	$\bar{\phi}$	$\pm\phi$	$\bar{dt}$	$\pm dt$	#	r
E1*	36.5	6.5	0.08	0.01	2	0.97
E2*	53.0	28.2	0.14	0.01	2	0.62
E3*	46.0	±5.5	0.33	±0.01	1	N/A
E4*	32.0	±10.5	0.07	±0.01	1	N/A
E5*	-22.6	53.5	0.16	0.1	4	0.18
S1*	-68.5	20.3	0.13	0.06	2	0.78
S2*	-64.5	47.1	0.22	0.06	2	0.26
S3	64.4	24.7	0.16	0.08	7	0.69
S4	44.8	24.1	0.15	0.10	10	0.70
S5*	33.3	26.1	0.14	0.06	3	0.66

Table 3.3

Mean and standard deviation of the results for each station in the CU/VUW deployment of short-period instruments. The # is the number of measurements and r is the length of the resultant vector. The results the has ± indicate that it is a single measurement and following number is the error in the result.

Scaling the results linearly according to delay time (Figure 3.10) reveals any relationship between the fast direction variation and delay time. The two trends in fast direction (northeast and northwest) show consistent delay times of 0.05–0.2 s, while the northeast fast direction is still prominant. Most of the anomalously large delay times of more than 0.2 seconds have inconsistent fast directions of north–south or east–west and could be related to another source of anisotropy, especially since these directions agree with studies of the mantle and lower lithosphere (Köhler, 2003; Audoine, 2002).

The most interesting result is at station E5, where the fast directions seem entirely random. From studying ray paths, those that cross the fault just before reaching the station result in a northwest fast direction while the others have a northeast fast direction (Figure 3.11). This station is the closest to a fault (~200 m away), which may be the cause of the variation in results; however, we would expect the fast direction to align with the strike of the fault, which is not the case here and an investigation of other stations close to faults is required.

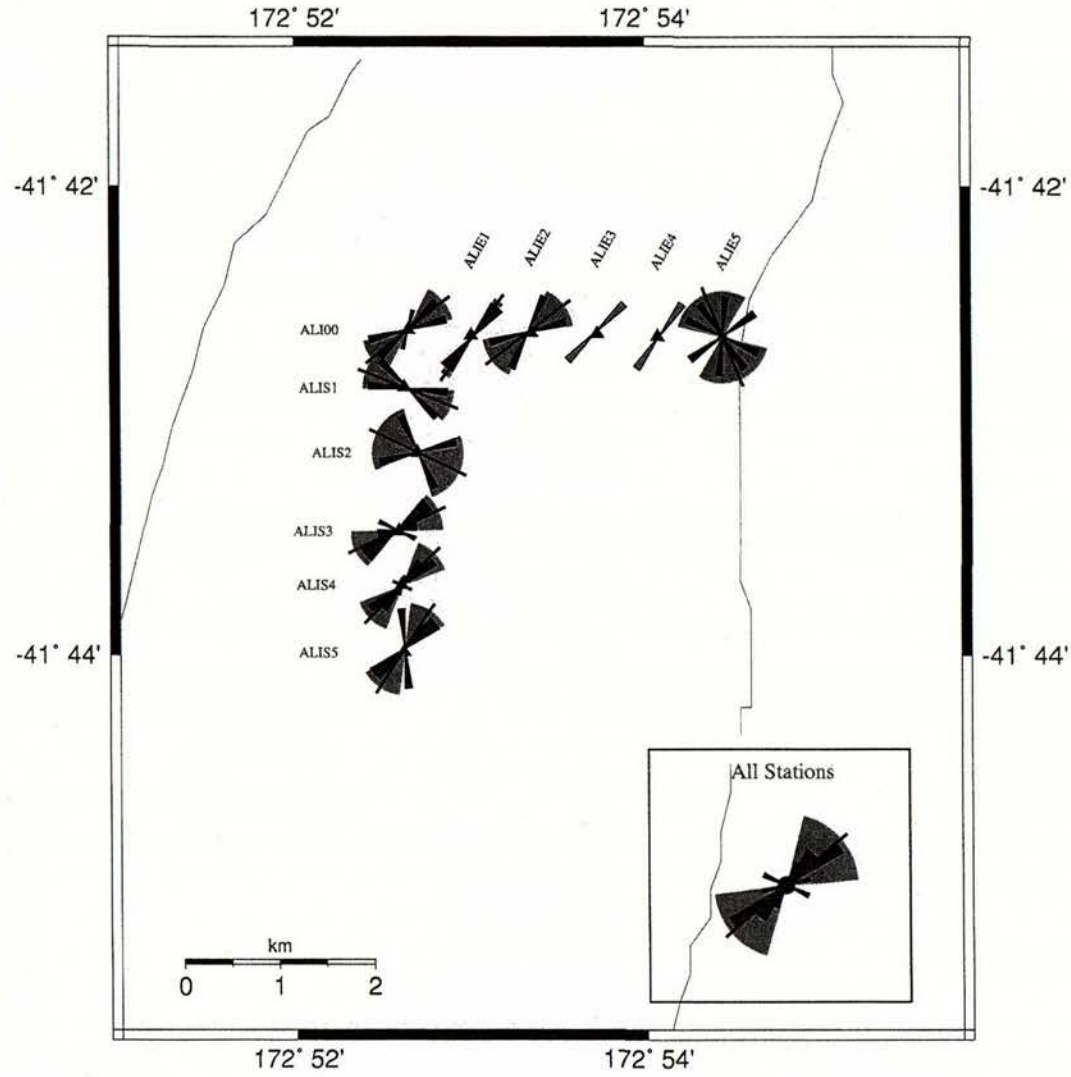

Figure 3.9 *Rose diagrams of the fast direction for each station in the CU/VUW short-period array, which include the mean (red) and standard deviation (light blue). Results from stations with only one measurement are represented in green. The inset shows the results and associated statistics from all the stations in the array.*

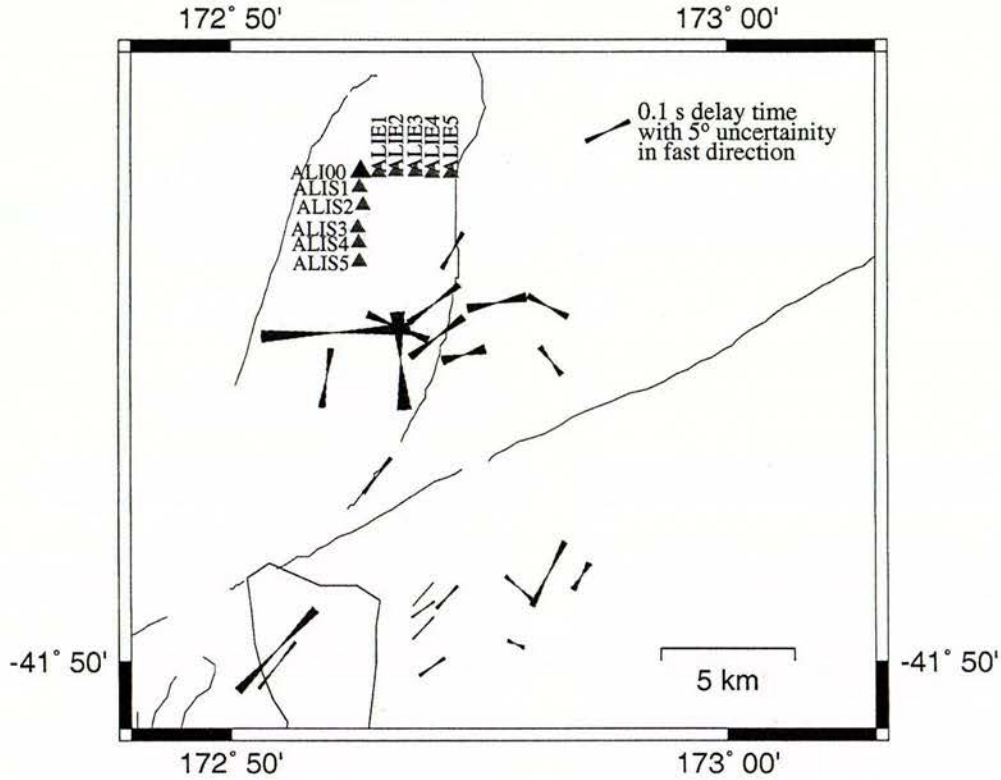

Figure 3.10 *Shear-wave splitting results for the short-period stations of the ALI00 array from the CU/VUW deployment. Measurements are projected to half-way between the source and station. Results with bold outlines are A quality and dotted outlines are B quality (see text). The length of the bowtie denotes the delay time, while the direction and the angle corresponds to the fast direction and its uncertainty.*

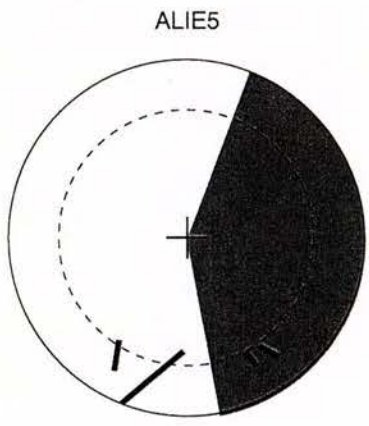

Figure 3.11 *Splitting measurements obtained from station ALIE5 as a function of back-azimuth and incidence angle. The dotted circle indicates the extent of the shear-wave window (45°) and the circumference of the circle corresponds to an incidence angle of 60°. The shade represents the range of back-azimuths where incoming rays may be affected by the fault, ~200 m to the east.*

3.4.5 GNS short-period results

Since the focal mechanisms of these events are available, we can calculate the polarisation of the incoming wave. The purpose of this is to see whether a single layer of anisotropy can explain the results; this is done by comparing the initial polarisation determined from correcting for shear-wave splitting with the predicted polarisation from the focal mechanism. In the case of only one layer of anisotropy, the initial polarisation determined by the shear-wave splitting analysis should be the same as that calculated from the focal mechanisms. Figure 3.14 shows that there is no correlation between the polarisation calculated using the different techniques and we can therefore conclude that a single layer of anisotropy cannot account for our splitting observations. Figure 3.12 shows that there is no correlation between the fast direction and the initial polarisation calculated by the automated shear-wave splitting program, which indicates that our results are not dependant on the initial polarisation. We can also test whether the shear-wave splitting is a product of the source mechanism by plotting the fast direction, obtained from the automated shear-wave splitting analysis, against the initial polarisation calculated from the focal mechanisms; we see that there is no correlation (Figure 3.13).

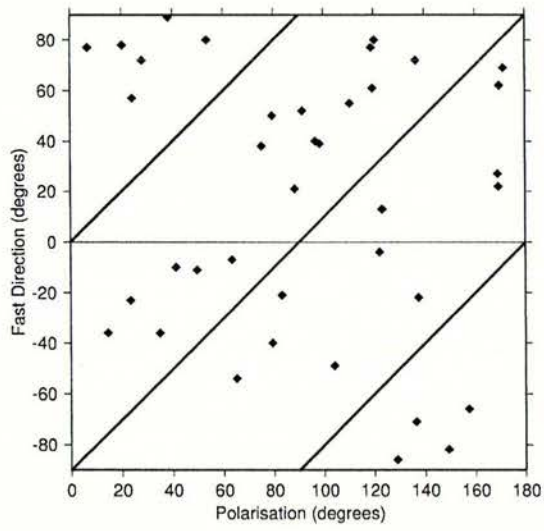

Figure 3.12 *Variation of the fast direction and initial polarisation, both of which were obtained using the automated shear-wave splitting technique. The blue bands indicate the zones that is due to the removal of NULL measurements from the results.*

After determining the predicted polarisation, we reprocessed the data with a fixed polarisation to see whether we could get better results. The manual method was used and the analysis window was picked so that it was similar to that chosen by the automated method.

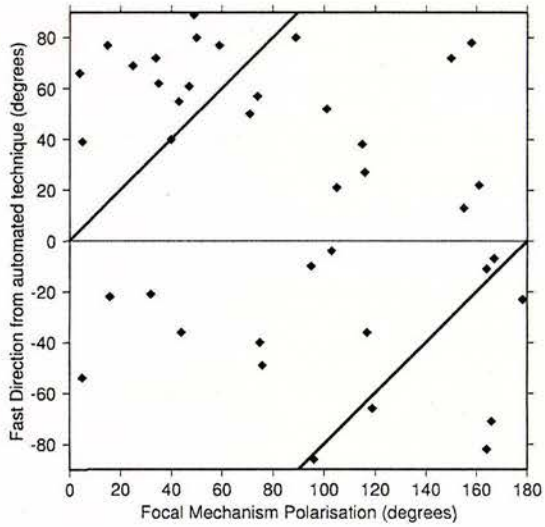

Figure 3.13 *Variation of the fast direction from the automated shear-wave splitting technique with the initial polarisation determined from the focal mechanisms. Red lines indicate values at which the source polarisation and the fast direction are equal.*

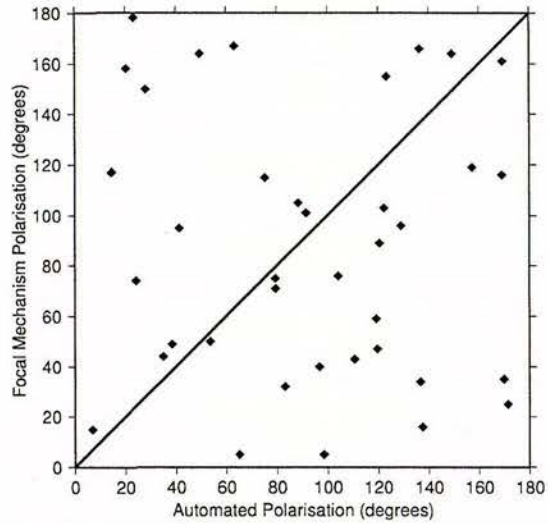

Figure 3.14 *Comparison of the initial polarisation determined from the automated shear-wave splitting analysis with those calculated using the focal mechanisms. The red line represents polarisations that are the same using both methods.*

Only nine out of the 39 events appeared to have improved by showing a more tightly defined error surface; on the contrary, sixteen deteriorated due to cycle-skipping. The manual method appears to be more sensitive to cycle-skipping and measurements from this were not considered in the final analysis.

The fault-parallel fast direction that is evident in the other deployments is also present in these results (Figure 3.15). Other trends appear to be forming at an angle to the strike of the faults, but more measurements are necessary to distinguish a trend. The delay times (0.03–0.3 s) are similar to those of the CU/VUW arrays. The spacing between stations (30–160 km) is significantly larger than the Fresnel zone, so each station samples a different volume of the crust. The variation in fast direction is similar to that seen in the other deployments

and there appears to be little relationship between the delay time and the fast direction.

Station	$\bar{\phi}$	$\pm\phi$	$\bar{dt}$	$\pm dt$	#	r
GOH*	8.9	36.5	0.13	0.141	7	0.44
ISI*	67.9	29.7	0.10	0.04	5	0.59
ISO*	77.1	19.5	0.16	0.09	3	0.79
LYL*	1.4	37.2	0.11	0.05	5	0.43
MAP*	-78.5	26.3	0.12	0.03	2	0.66
WAI*	-61.0	50.8	0.04	0.00	2	0.21
WRO*	89.0	±12.8	0.13	±0.01	1	N/A
CAS*	69.0	±1.8	0.10	±0.00	1	N/A
CON*	77.0	±4.5	0.23	±0.01	1	N/A
JOP*	-66.0	±4.5	0.09	±0.01	1	N/A
KEK*	50.0	±5.0	0.33	±0.01	1	N/A
KEN*	-40.0	±10.3	0.06	±0.00	1	N/A
MOL*	-21.0	±2.8	0.15	±0.01	1	N/A
NMC*	72.0	±8.0	0.075	±0.01	1	N/A
PUH*	46.0	34.2	0.12	0.06	5	0.49
RIM*	66.0	±4.8	0.20	±0.01	1	N/A
SRW*	-36.0	±3.8	0.13	±0.13	1	N/A

Table 3.4

Summary of statistics for each station in the GNS deployment of short-period instruments. # is the number of measurements and r is the length of the resultant vector (see text for more details). The ± indicates that it is a single measurement and the following number is the standard error in the result

There is more variation in the results at each station than in the other deployments (Figure 3.16). Nine stations had only one usable measurement and due to the large station spacing the measurements could not be combined. Performing Rayleigh's test for non-randomness, on the stations that have enough measurements to perform statistics, shows an amount of random behaviour that makes it difficult to define a trend in the results.

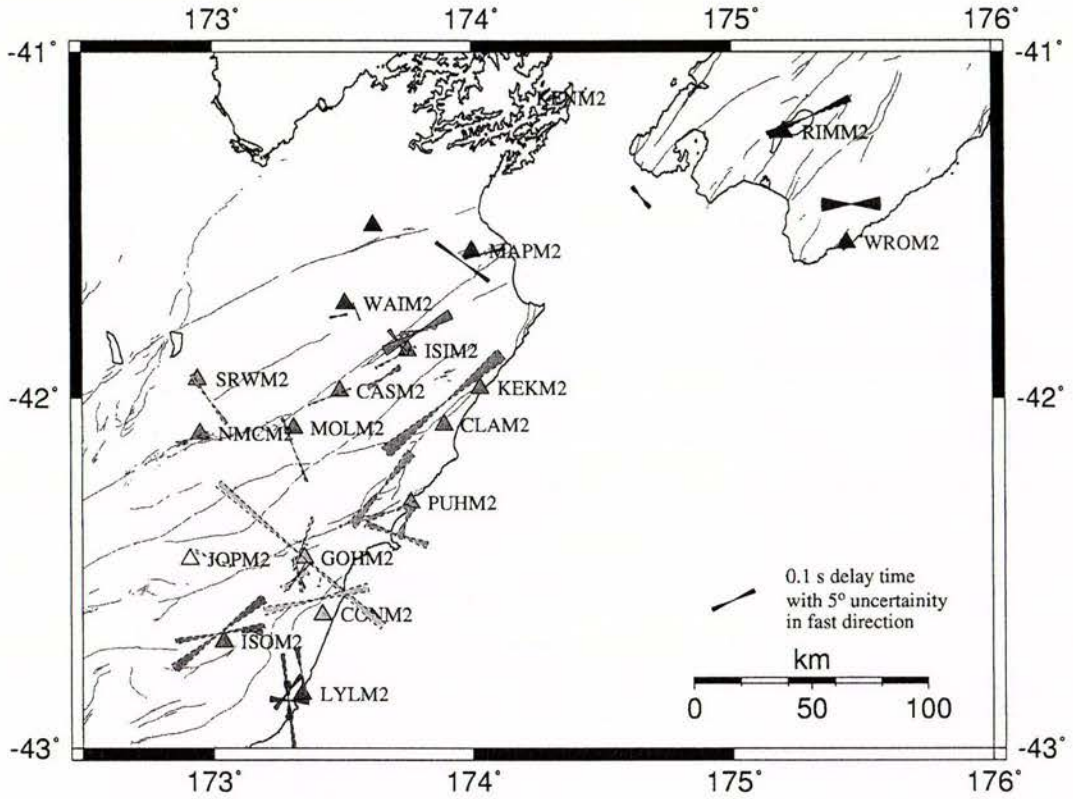

Figure 3.15 *Shear-wave splitting results for the short-period stations of the GNS deployment. Measurements are projected to half-way between the source and station. Results with bold outlines are A quality and dotted outlines are B quality (see text). The length of the bowtie is proportional to the delay time, while the direction and the angle corresponds to the fast direction and its uncertainty.*

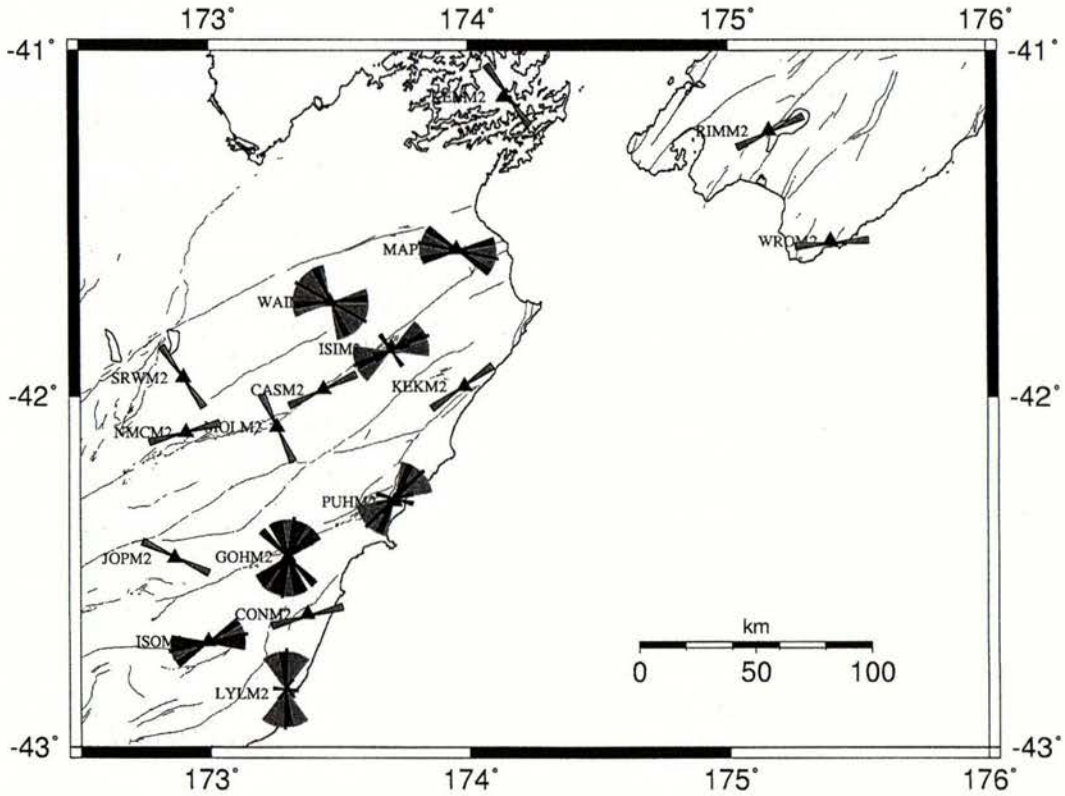

Figure 3.16 *Rose diagrams of the fast direction for each station in the GNS short-period deployment, which include the mean (red) and standard deviation (light blue). Results from stations with only 1 measurement are represented in green.*

3.5 Discussion

The results from both the broadband and short-period arrays suggest that the location of anisotropy is near the surface, based on the observed variation in fast directions and the spacing between stations. The change in fast direction between closely spaced stations suggests that the source of the anisotropy must be shallower than the maximum depth at which the two stations' Fresnel zones overlap. Stations WAG and CCH from the CU/VUW broadband array show a change in fast direction and are only 10 km apart. This requires the source of anisotropy to be shallower than ~15 km. The broadband stations from the CU/VUW deployment show a general consistency at each station while being inconsistent between stations. This pattern has also been observed in studies of crustal anisotropy in the lower North Island, on the Wellington Peninsula (Gledhill, 1991) and Tararua Range (Gledhill and Stuart, 1996). The delay times from these North Island studies are similar (0.02–0.22 s) to the results here (0.05–0.3 s). Gledhill (1991) suggested that the estimated 10% shear-wave velocity anisotropy is confined to the top 2–3 km of the crust in the Wellington region as the average station spacing is 5 km and there are large variations in fast direction between stations. Results from the Tararua array also reveal large station-to-station variations and suggest the depth of anisotropy to be 5–10 km. Figure 3.7 shows that there is little consistency when the results are projected to depth, strengthening the possibility that the source of the anisotropy is near the surface.

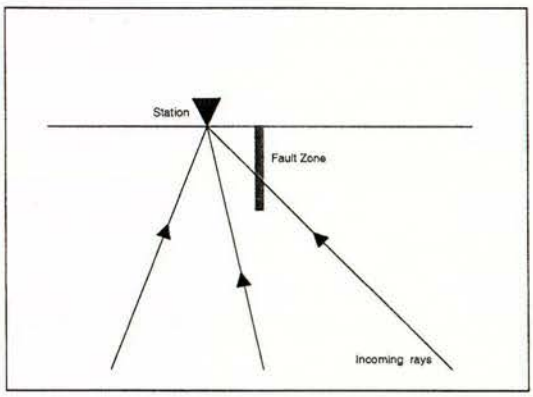

Figure 3.17 *This diagram illustrates how incoming rays may be affected by faults near the station.*

The results from the short-period array show that the fast direction is consistent across the array. This is expected as the Fresnel zones suggest the stations sample the same region. The inconsistent results at station E5 suggest that fast directions may be different if the

ray travels through a fault immediately before reaching the receiver. This could be used to indicate the depth extent of the fault, as ray paths that cross the fault further from the station will cross the region at a greater depth and may not go through the fault zone, in which case the fast direction will not be affected (illustrated in Figure 3.17). This may depend not only on the incidence angle but also the width of the fault zone and the back-azimuth, as these elements affect the amount of time the ray travels through the fault. Figure 3.18 shows a single event that has corresponding splitting results from several stations at a variety of back-azimuths. Stations that are immediately adjacent to faults (PUHM2 and CONM2) have fast directions that are parallel to the fault strike, while at the other stations the fast direction is almost perpendicular to the faults. This behaviour is seen for two other events but since the stations are far apart, there are only nine events where shear-wave splitting analysis could be performed on multiple stations and none of the other six showed this behaviour due to the geometry.

Paulssen (2004) explained the variation in fast directions observed in California as a combination of azimuthal anisotropy and transverse isotropy. Results from local S phases at shallow angles of incidence showed that fast directions are consistently either perpendicular to the ray paths or parallel to the strike of the San Andreas fault. The fast directions that are perpendicular to the ray paths suggest that SH polarisation is leading SV particle motion and therefore cannot be explained by the free surface effect, which results in early P-SV particle motion. Paulssen's (2004) study suggested that the observed fault parallel fast direction is due to azimuthal anisotropy and measurements that are perpendicular to the ray paths are due to transverse isotropy with a vertical axis of symmetry. By applying this analysis to our results from the GNS deployment we can come up with similar conclusions. Figure 3.19 shows splitting measurements plotted along their ray path for station PUH; they display both fault-parallel and ray path-perpendicular fast directions. Here the events closest to the station that have an incidence angle well within the shear-wave window, show fault-parallel fast directions, which we interpret as due to azimuthal anisotropy; while those with larger angles of incidence have fast directions perpendicular to the ray paths. Using the arguments from Paulssen (2004), we interpret these as caused by transverse isotropy with a vertical axis of symmetry, likely to be caused by foliated schist in the upper crust.

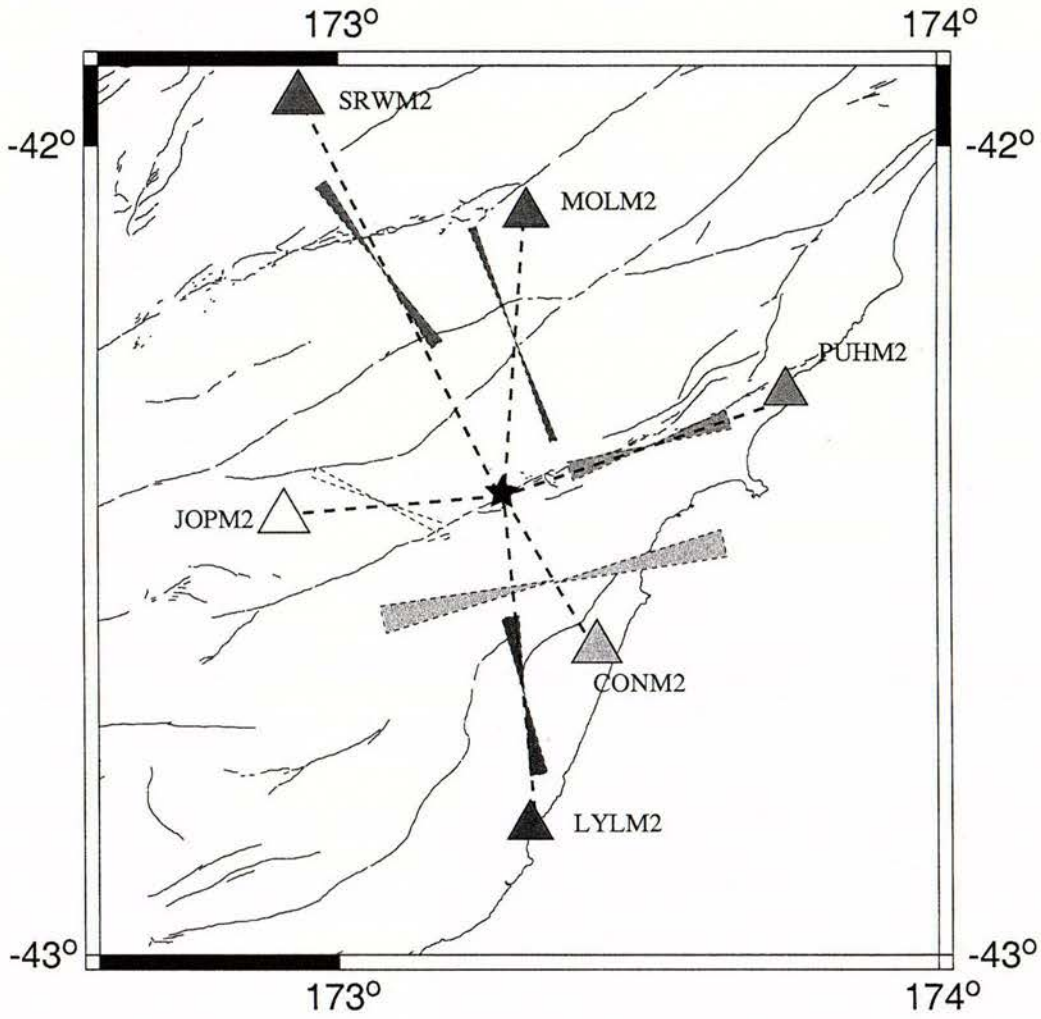

Figure 3.18 *Shear-wave splitting measurements from stations recording the same event. Ray paths are indicated by the dotted lines and the stations are marked by triangles.*

There are a variety of fast directions from deep events; two are fast directions that are also seen at shallow depths, which have possibly been resplit and another is a new direction that is north-trending. At depths greater than 50 km, we are likely to be sampling anisotropy from the mantle as the ray path travels a greater distance through the mantle than the crust. However, we also see multiple layers of anisotropy in the crust, as initial polarisations calculated from focal mechanisms are different to those determined from shear-wave splitting analysis. This suggests that crustal anisotropy in Marlborough is complex, and varies with depth as well as laterally.

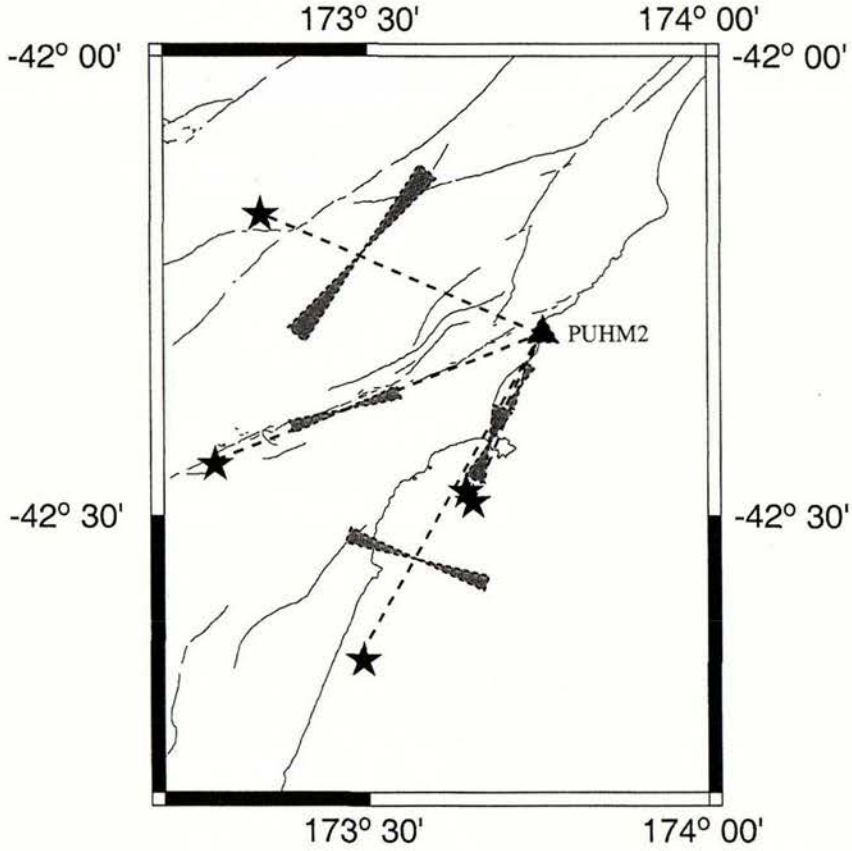

Figure 3.19 *Shear-wave splitting results plotted along their ray path for station PUH. Fast directions perpendicular to the ray paths suggest transverse isotropy with a vertical axis of symmetry.*

CHAPTER 4

FOCAL MECHANISMS AND STRESS ORIENTATIONS

4.1 Introduction

The relation between stress and faulting is important since field experiments show that frictional relationships suggested by laboratory measurements cannot always be applied directly to real faults, and recent studies in California have suggested that plate-bounding transform faults are weak (Provost and Houston, 2001; Hickman and Zoback, 2004; Townend and Zoback, 2004). To investigate the frictional strength of faults in Marlborough, it is necessary to understand the state of stress within the region. The S_{Hmax} direction also needs to be determined so that we can distinguish between geologic structure and stress when investigating what controls the crustal anisotropy. The following chapter explains that we obtain repeatable and consistent S_{Hmax} directions at a high angle to the strike of the major faults using a variety of inversion algorithms on either first motion or focal mechanism data. Throughout this chapter, focal mechanisms and stress results are displayed using a lower hemisphere, equal-area projection.

We have collated focal mechanism data from published sources (Anderson *et al.*, 1993; Reyners *et al.*, 1997; McGinty *et al.*, 1997; Webb and Anderson, 1998; Dowrick and Rhoades, 1998; Doser *et al.*, 1999) and the Harvard CMT (http://www.seismology.harvard.edu/CMT search.html) and NEIC (http://neic.usgs.gov/neis/sopar) catalogues. No composite mechanisms are included in the data set. First motion data obtained by the Institute of Geological and Nuclear Sciences (GNS) from the studies of Lake Tennyson (McGinty *et al.*, 1997) and Marlborough seismicity (Reyners *et al.*, 1997) are also used. Since this study focusses on the stress regime in the crust, we restrict our analysis to earthquakes with hypocentral depths

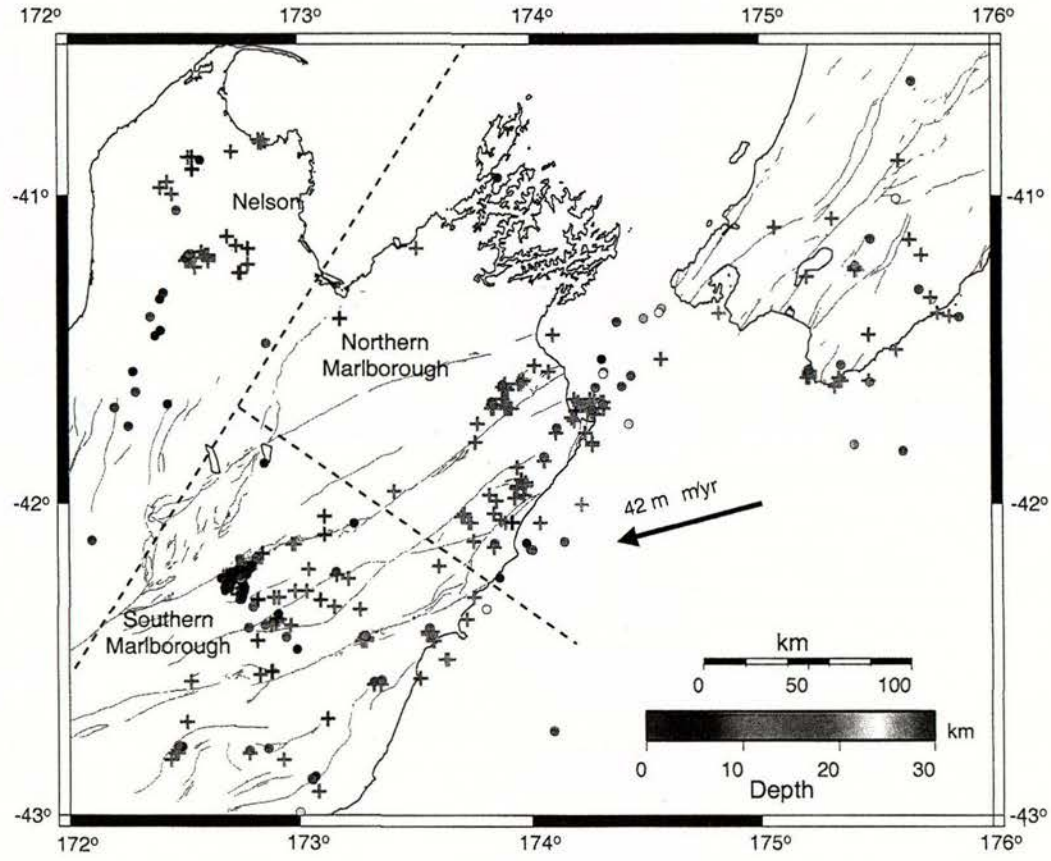

Figure 4.1 *Epicenters of the events used for stress calculations, colour coded according to depth. Earthquakes that include first motion information are represented by a cross and those where only the focal mechanism have been obtained are shown with a circle. The arrow indicates the plate motion vector (DeMets et al, 1990). Regions outlined in the figure are those defined by McGinty et al (2000).*

shallower than 30 km (Figure 4.1).

Table 4.1 presents the groups of data that are discussed in the rest of the chapter. The table also shows which stress inversion algorithms were performed on the group and what the results were used for.

Focal mechanisms obtained by Reyners *et al.* (1997) have previously been used in stress inversions with the GETSTRESS algorithm (McGinty *et al.*, 2000). As a test, we attempted to replicate McGinty *et al.*'s (2000) results using Michael's (1987) SLFAST algorithm on the same data set. The focal mechanism data were divided into three clusters (Appendix C), according to the boundaries shown by McGinty *et al.* (2000) (Figure 4.1). The focal mechanisms within each region were used in separate inversions. The results from the Marl-

Name	#	Data type	Inversions	Purpose	Sources
TEN90	34	F.mot F.mech	SLFAST FMSI MOTSI	Inversion comparison, focal mechanism comparison, and overall stress results.	McGinty *et al.* (1997)
MARL93	229	F.mot	SLFAST FMSI MOTSI	Inversion comparison and overall results for Marlborough.	Reyners *et al.* (1997)
FMOT93	150	F.mot (no related F.mech)	MOTSI	Investigating the effect of applying a stress constraint when determining focal mechanisms	Reyners *et al.* (1997)
ALLFM	177	F.mech	SLFAST	Overall results for the Marlborough region.	Anderson *et al.* (1993) McGinty *et al.* (1997) Reyners *et al.* (1997) Webb and Anderson (1998) Dowrick and Rhoades (1998) Doser *et al.* (1999) CMT catalogue NEIC catalogue

Table 4.1
Summary of data sets used in stress inversions (Appendix C). F.mech stands for focal mechanisms and F.mot for first motions.

borough regions are reasonably similar to those obtained by McGinty *et al.* (2000), as shown in Table 4.2 and Figure 4.2. In the Nelson region, the results from the two methods do not agree, with McGinty *et al.*'s (2000), suggesting that both S_1 and S_3 are moderately plunging ($\sim$45°) while the results calculated using SLFAST show them to be near horizontal.

Two faulting regimes are evident from the results. In southern Marlborough, the stress orientations correspond to a strike-slip faulting regime in which the intermediate stress is vertical and the other stresses are horizontal. To the north, and further from the plate boundary, S_2 and S_3 have larger confidence regions and are rotated so that S_2 is close to horizontal. This may reflect a more dominant reverse component of faulting, which is evident in the geology. The result from the Nelson region shows a distinct rotation in the S_{Hmax} direction; this area is further from the the plate boundary. Focal mechanisms here indicate more reverse faulting, which is also implied by the stress result with S_3 being close to vertical.

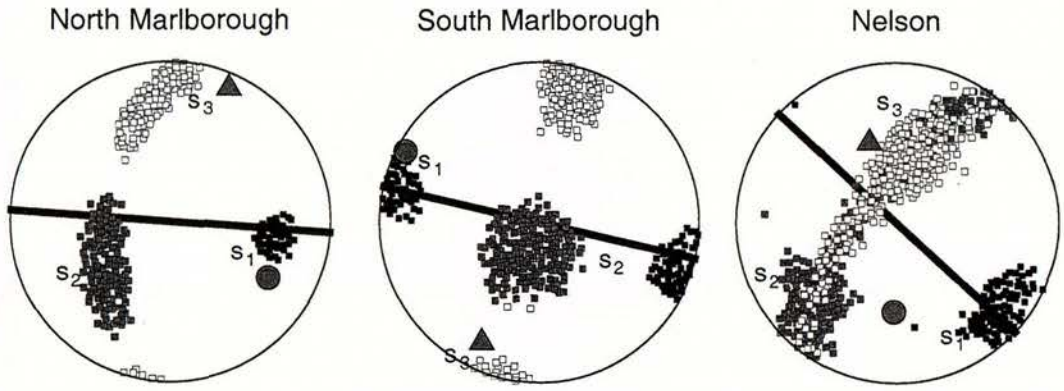

Figure 4.2 *Results obtained by applying the SLFAST inversion on focal mechanisms within regions described in McGinty et al (2000). Squares indicate the solutions computed from the bootstrap statistics to lie within the 95% confidence interval. The S_{Hmax} direction, computed using the transformation described by Lund (2000), is shown by the solid red line. The green symbols indicate the results obtained by McGinty et al (2000) using the GETSTRESS inversion; S_1 is marked by a circle and S_3 by a triangle.*

		GETSTRESS(McGinty *et al.*, 2000)		SLFAST			
Region	Stress	trend	plunge	trend	plunge	S_{Hmax}	#
N. Marlborough	S_1	120	30	102	33	274	87
	S_3	024	10	355	24		
S. Marlborough	S_1	298	6	283	1	283	39
	S_3	206	18	13	19		
Nelson	S_1	342	46	136	10	313	22
	S_3	182	42	33	51		

Table 4.2

This table shows the comparison of stress results using two different inversion techniques based on the same set of focal mechanisms. The GETSTRESS results were obtained by McGinty et al (2000) and the SLFAST results were computed in this study. The S_{Hmax} calculations are based on the results from SLFAST and computed using the algorithm described by Lund (2000) (Section 2.2).

4.2 Comparison of stress inversion techniques

We work with a variety of stress inversion algorithms to ensure that the results are not dependant on the particular algorithm used. The following section inspects the differences in results obtained using various techniques and discusses the benefits of each approach.

4.2.1 A comparison of inversion algorithms

By using compatible first motion and focal mechanism data we can make a direct comparison of the various inversion algorithms' ability to constrain the stress tensor.

Figure 4.3 *Stress results from near Lake Tennyson (TEN90 data). Large circles in the boxes are output from different stress inversion algorithms; examples and further explanation of the large circles are in figures 2.8, 2.9 and 2.10. The outline of the box indicates the group of related events, where red denotes events on the main fault, black is off-fault earthquakes and the dashed outline means all events were used in the inversion. The red line indicates the S_{Hmax} direction, calculated using the transformation described by Lund (2000)*

Data from the 1990 Lake Tennyson earthquake and its aftershocks (TEN90) obtained by McGinty *et al.* (1997) were used with the `SLFAST`, `FMSI` and `MOTSI` algorithms (Section

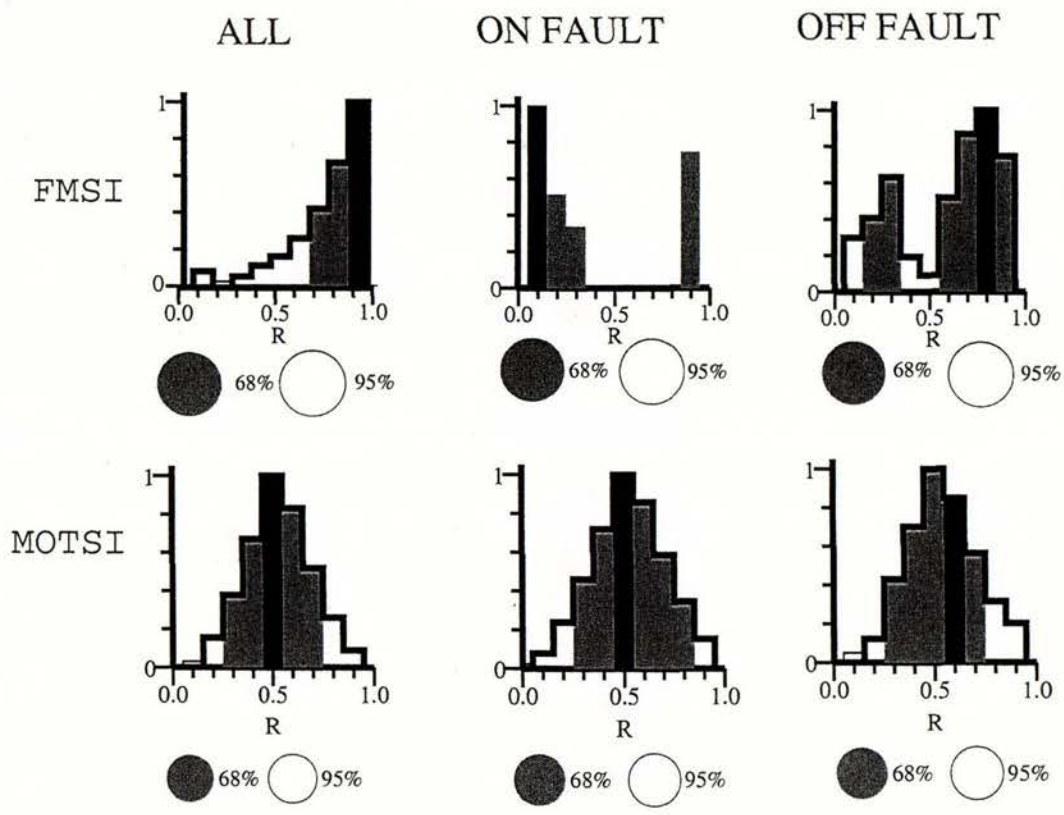

Figure 4.4 *Histograms of the stress ratio estimates (R) from* `FMSI` *and* `MOTSI` *for the Lake Tennyson data.*

2.2.4) and even though the techniques yielded very similar "best-fitting" solutions, the confidence intervals were significantly different (Figures 4.3 and 4.4). The inversions that used focal mechanisms alone tended to yield smaller confidence regions than those produced by `MOTSI`. This difference was noted by Abers and Gephart (2001) when testing their algorithm and they attributed it to the exclusion of errors related to poorly constrained mechanisms. The shape of the stress ellipsoid is described by the stress ratio, R (Section 2.2) and is consistent between groups but varies with each inversion program. `MOTSI`, `SLFAST` and `FMSI` give optimum R values of 0.5, 0.3 and 1 respectively. From the histograms of R plotted from `FMSI` and `MOTSI` (Figure 4.4), it appears that `MOTSI` gives the most stable result.

The result from the Lake Tennyson data on the fault defined by McGinty *et al.* (1997) shows that the stress result is not well constrained due to the large confidence regions and unusual shape of the confidence region from the `FMSI` inversion (Figure 4.3, "on-fault" group), this could occur for two reasons; the first is that the focal mechanisms have low diversity,

and the second is that there are only 13 focal mechanisms in the group. The problem of focal mechanism diversity occurs when focal mechanism parameters are similar. As mentioned in Section 2.2.2, one focal mechanism places very little constraint on the stress: consequently if all the focal mechanisms are similar, they jointly impose little constraint on the stress orientations since all the data essentially act as one mechanism.

These differences between the results from the three algorthims were also examined with the Marlborough data of Reyners *et al.* (1997)(Figure 4.5). As with the results from Lake Tennyson, the difference between the results computed with different algorithms lies predominantly in the uncertainties. The confidence regions of results obtained from algorithms using solely focal mechanism data (`SLFAST` and `FMSI`) are smaller than for results from algorithms that compute the stress directly from first motions (`MOTSI`). Once again, this difference can be attributed to the inclusion in `MOTSI` of errors due to mispicked first motions and unconstrained focal mechanisms. Another difference between the inversions is that results obtained from `MOTSI` and `FMSI` often show S_1 or S_3 plunging steeply, whereas results from `SLFAST` are close to horizontal.

It appears that the parameter of the best stress model with the most variation between the inversions is the stress ratio (R). The histogram plots from `MOTSI` and `FMSI` can be used to check whether the solution is stable (Figure 2.9 and 2.10). The output from the Lake Tennyson data (Figure 4.4) demonstrates that `FMSI` does not always choose the best value of R, this is also seen in comparisons made by Abers and Gephart (2001). It appears that `FMSI` favours either large or small values of R, jumping between 0.1 and 0.9. The R values from `MOTSI` and `SLFAST` tend to agree and range between 0.2–0.8.

By comparing the stress results obtained using three different inversion algorithms, it can be seen that although the optimal solution is the same for each technique, the confidence regions vary significantly. Since the scope of this project is to look at the regional stress field in Marlborough and not small-scale variations, the uncertainties are not a concern as the chosen solutions from the algorithms appear consistent.

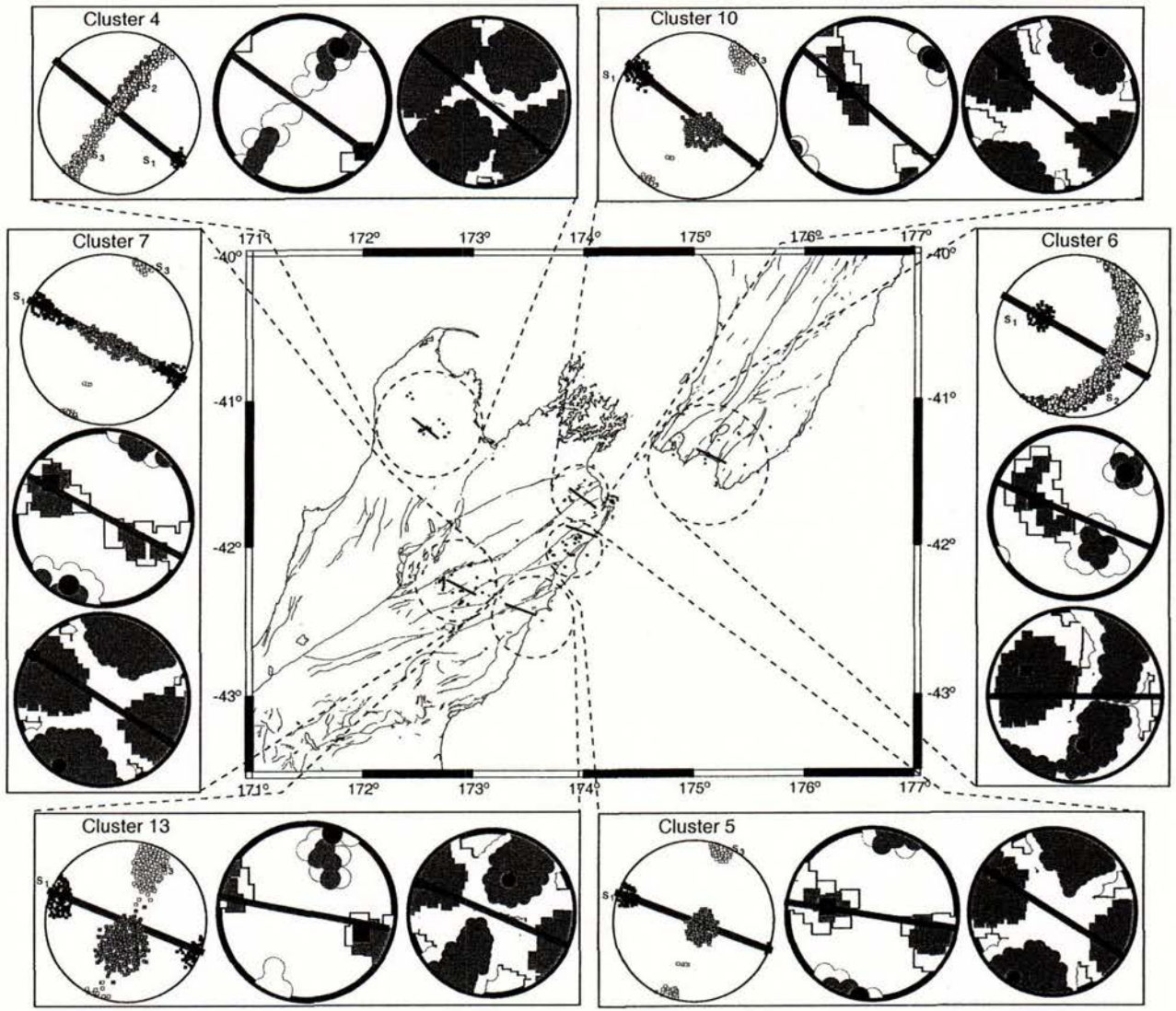

Figure 4.5 *Stress results using different inversion techniques on focal mechanisms and first motion data in the Marlborough region (MARL93 data). There are three results for each cluster contained in the boxes,* `SLFAST` *(left),* `FMSI` *(middle) and* `MOTSI` *(right). Events in different clusters are colour coded. The result on the map is the* S_{Hmax} *direction from the* `SLFAST` *results.*

4.2.2 A comparison of methods for constructing focal mechanisms

The purpose of this section is to see whether the stress constraint can help define focal mechanisms when other methods have failed, due to insufficient first motion data or poor station coverage. In Marlborough, events with focal mechanisms previously determined by Reyners *et al.* (1997) are removed from the first motion data, so that only events without pre-existing focal mechanisms are left (FMOT93). These events are then put through the `MOTSI` stress inversion program and their focal mechanisms calculated with and without applying the constraint that the focal mechanisms must fit a single stress model.

Figure 4.6 shows the extent to which focal mechanisms within a cluster can be improved using the stress constraint. On the right of the figure is a comparison of the P and T axes of focal mechanisms with (bottom) and without (top) the stress constraint. The plot on the left of the figure displays just how much improvement has been made and can be used to pick out events that don't agree with the condition of a homogenous stress field. In the plot dS is the difference in the misfit of the two focal mechanisms where high positive values (dS>2.32) indicate a poor fit to the first motions and negative values show improvement in the fit, and where dM is the similarity between the constrained and unconstrained focal mechanisms (dM=1 indicates no change). Figure 4.6 is an example of a good response to the stress constraint. There is little degradation from the change in the focal mechanism, suggesting that the first motions are consistent with the stress model. Only six events show significant change in the focal mechanisms (dM $<$ 0.8). The statistic dM is described by Equation 4.1, which is the double inner product (:) of the unconstrained (M_j) and stress-constrained (M_j^c) moment tensors.

$$dM_j = \frac{1}{2} M_j : M_j^c \tag{4.1}$$

Three sets of focal mechanisms have been computed for the Lake Tennyson data set (Figure 4.7). McGinty *et al.* (1997) constructed focal mechanisms using both first motions and amplitude ratios. Here we use `MOTSI-fp`, which computes focal mechanisms solely from first motions and without any additional information, and then, once a stress model has been determined, use `MOTSI-1sm`, which uses both the first motions and the stress model to

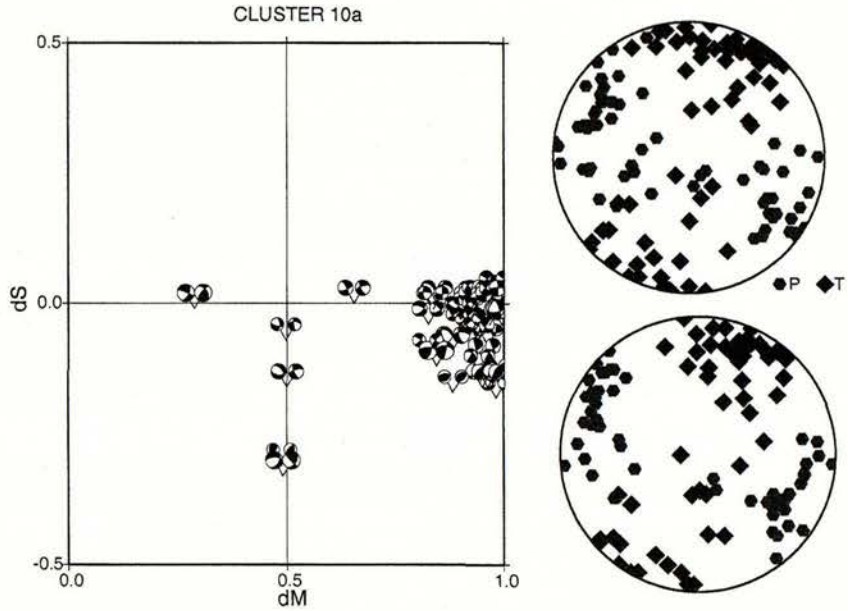

Figure 4.6 *The result of focal mechanisms (FMOT93 data) computed with the stress constraint using* `MOTSI-1sm` *and the computed stress result in Table 4.3. On the left of the figure is a plot of the* `MOTSI` *statistics where dS describes the fit with the the stress model (increasing dS indicates larger misfit) and dM is a measure of the similarity in the focal mechanism (dM=1 indicating they are the same). Focal mechanisms on the right (blue) were calculated with the stress constraint and those on the left (red) without. On the right of the graph are the P and T axes of the focal mechanisms calculated with (bottom) and without (top) considering stress.*

	S_1		S_3		
Cluster	trend	plunge	trend	plunge	#
4a	302	35	042	15	48
8a	300	25	206	8	36
10a	115	5	020	46	66

Table 4.3

Stress results from three clusters used in comparing focal mechanisms (FMOT93 data) determined with and without the stress constraint. Stress parameters calculated using `MOTSI` *inversion program. These clusters are different from those in Figure 2.5 as only events without pre-existing focal mechanisms are used.*

constrain the focal mechanism. Looking at the P and T axes of the three sets, we see that there is more scatter in the focal mechanisms constrained only by first motions (Figure 4.7). In Figure 4.8 it is evident that the focal mechanisms show improvement with the introduction of the stress constraint as the first motions are consistent with the stress model ($dS<0.65$, which is equivalant to the 68% confidence region). Most of the focal mechanisms calculated with

the stress constraint are similar to those calculated without (dM>0.9), but what changes have been made appear to have improved the fit of the focal mechanisms with the first motions (dS<0).

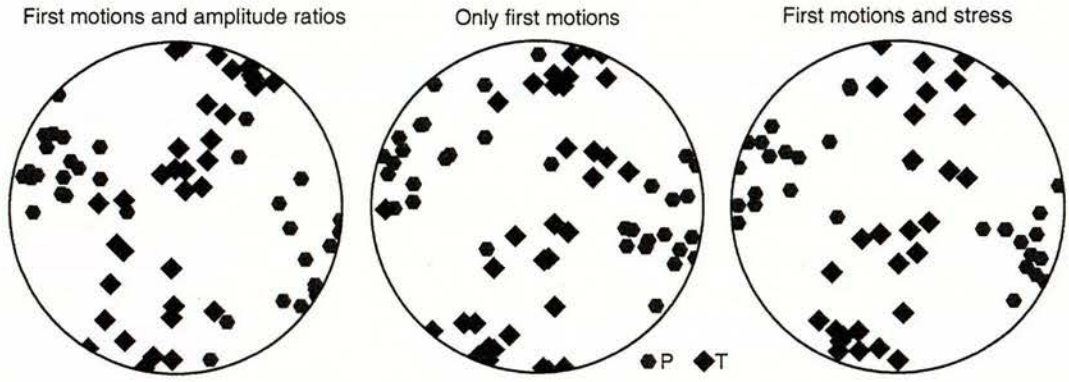

Figure 4.7 *P and T axes of focal mechanisms computed using different techniques. On the left are focal mechanisms obtained by McGinty et al (1997). They were computed using both first motions and amplitude ratios. In the middle are focal mechanisms computed using* `MOTSI-fp`*, which takes into account only first motions. On the right are the focal mechanisms determined using* `MOTSI-1sm` *that selects focal mechanisms that fit both the stress model and first motions.*

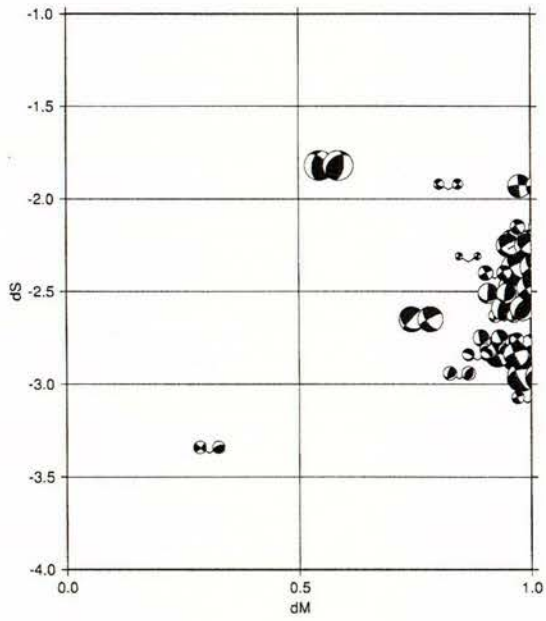

Figure 4.8 *The effect of the stress constraint on focal mechanisms near Lake Tennyson (TEN90 data). The graph is of* `MOTSI` *statistics where dS descibes the fit with the the stress model (increasing dS indicates larger misfit) and dM is a measure of the similarity in the two focal mechanisms (dM=1 indicates they are the same). The focal mechanisms on the right were computed with the stress constraint and those on the left without.*

By comparing the results of constructing focal mechanisms using different methods we have shown that a homogeneous stress requirement can be used to help constrain focal mechanisms to a similar degree as amplitude ratio data.

4.3 Stress results

In this section we present the results obtained using the SLFAST, FMSI and MOTSI inversion algorithms with first motion and focal mechanism data in Marlborough. The S_{Hmax} direction has been calculated for each result using the transformation described by Lund (2000). Our focus here is on relating the stress orientations and the stress ratio (R) to the major faults and drawing inferences about their frictional strength.

4.3.1 Crustal stress in the Lake Tennyson area

First motion data and focal mechanisms were obtained from the McGinty *et al.* (1997) Lake Tennyson study (TEN90). Since we had both first motions and focal mechanisms, the Abers and Gephart (2001) MOTSI algorithm could be used to calculate the stress tensor.

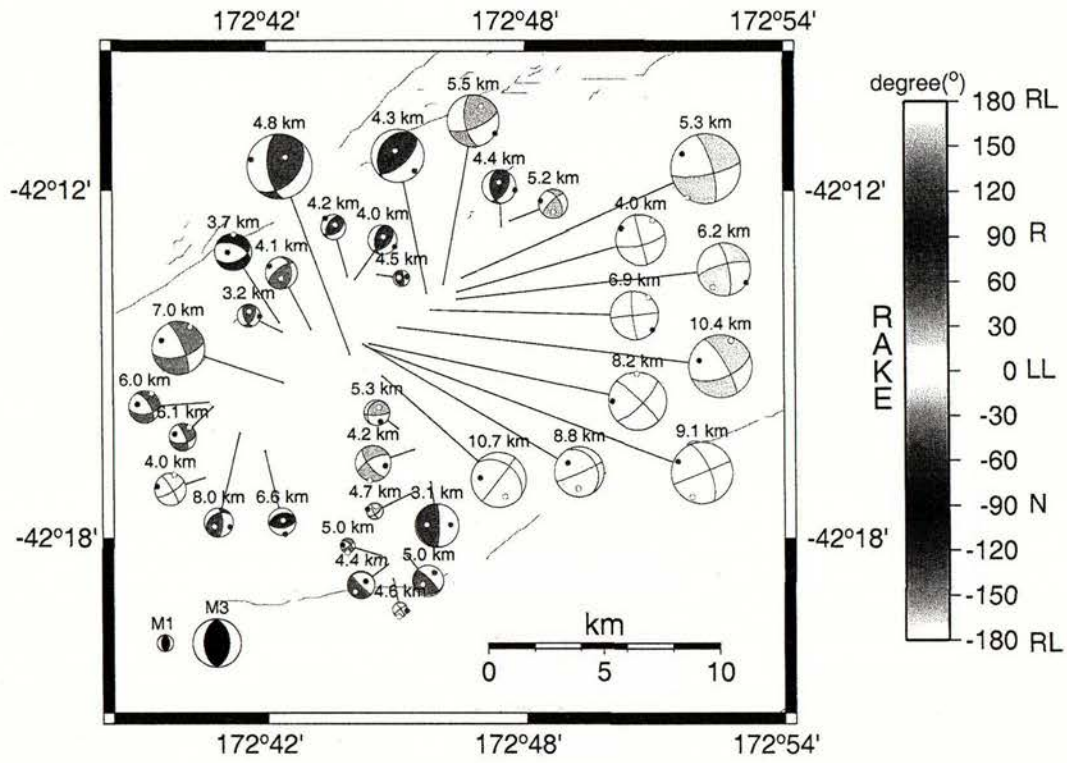

Figure 4.9 *Focal mechanisms obtained by McGinty et al (1997) and used in an SLFAST stress inversion (TEN90 data). The compressional quadrant is shaded according to rake, with the corresponding faulting regime indicated on the scale, e.g. LL for left-lateral strike slip. Dots in each quadrant represent the P (solid) and T (clear) axes.*

The focal mechanisms (shown in Figure 4.9) were calculated using both amplitude ratios and first motions so they are better constrained than those computed solely from first motions. McGinty *et al.* (1997) identified seven groups of events but they did not estimate sufficient mechanisms to invert for stress. Instead, all the data were used in a single inversion using all three techniques, then the data were split into two groups, corresponding to earthquakes that lie on and off the main rupture, defined by McGinty *et al.* (1997). The results of the stress inversions are presented in Figure 4.3 and Table 4.4, and show that when a group has fewer than 20 focal mechanisms the stress directions are not clearly resolved. In particular the S_2 and S_3 directions define a girdle, which we interpret as them being of similar magnitude. Partitioning of the data set with so few focal mechanisms did not yield stable solutions, as the inversion algorithms gave different results. The S_{Hmax} direction is consistent using all the inversions except for the result obtained with `FMSI` for the on-fault group, in which there are only 13 focal mechanisms with low diversity (Figure 4.9). The results from using all the focal mechanisms in the Lake Tennyson data set indicate a stress regime favouring strike-slip faulting.

		SLFAST			MOTSI			FMSI			
Group	Stress	trend	plunge	S_{Hmax}	trend	plunge	S_{Hmax}	trend	plunge	S_{Hmax}	#
All	S_1	108	4	288	104	7	286	90	30	285	34
	S_3	017	17		197	26		196	26		
On rupture	S_1	119	16	286	100	14	281	74	26	254	13
	S_3	216	24		194	16		343	2		
Off rupture	S_1	106	1	300	303	28	287	95	23	284	21
	S_3	016	23		178	48		196	26		

Table 4.4

A table displaying results from three stress inversions using different groups of input data (TEN90). `SLFAST` and `FMSI` inverts focal mechanisms for stress, while `MOTSI` inverts straight from first motions.

4.3.2 Crustal stress directions in Marlborough and Wellington computed from first motion data

The Marlborough regional first motion data from GNS were used (MARL93). Events were only used if they occurred at depths less than 50 km and if they had more than five first motions. Focal mechanisms were constructed for each event using the program `MOTSI`-

fp. The data were divided into clusters using a K-MEANS clustering algorithm, which divides the events into a specified number of groups depending on the distances between the earthquakes' hypocenters. For this study, we used an average number of 30 events per cluster, which in this case corresponds to 14 groups; then we only perform inversions on clusters with more than 20 events. The program calculated that 11 out of the 14 clusters met the criterion, six were shallow (within the crust, <25 km) and five deep (25–50 km). The deep clusters are not discussed further here as they are likely to incorporate plate interface or slab events. Each of the shallow clusters was run through the SLFAST (Michael, 1987), FMSI (Gephart, 1990) and MOTSI (Abers and Gephart, 2001) inversion programs. The results are displayed in Table 4.5 and Figure 4.5.

		SLFAST			MOTSI			FMSI			
Cluster	Stress	trend	plunge	S_{Hmax}	trend	plunge	S_{Hmax}	trend	plunge	S_{Hmax}	#
4	S_1	128	8	309	128	9	308	129	10	306	48
	S_3	223	32		218	1		034	25		
5	S_1	290	11	291	303	17	302	279	45	279	43
	S_3	021	3		211	7		189	0		
6	S_1	296	49	299	296	36	270	288	50	293	20
	S_3	086	37		170	40		051	25		
7	S_1	297	3	303	303	6	303	304	28	298	38
	S_3	027	3		213	7		207	14		
10	S_1	307	16	308	302	35	309	303	64	311	44
	S_3	039	9		042	15		055	10		
13	S_1	290	7	292	292	2	293	112	33	281	36
	S_3	024	27		205	5		017	2		

Table 4.5

Stress results obtained from various inversion algorithms using the GNS first motion data (MARL93). The cluster number refers to events shown in figure 4.5 and # indicates the number of events in each cluster.

The optimal solutions from the inversions are reasonably consistent, with the exception of cluster 10 for which FMSI calculates S_1 to be steeply plunging, while in other methods it is close to horizontal. The S_{Hmax} direction has an average of $299\pm17°$ and is consistent between clusters. Cluster 6 shows S_2 and S_3 defining a plane (for which S_1 is the pole); the earthquakes in this region are slightly deeper (an average depth of 20 km) and likely to be due to motion on the plate interface. Further south, the stress results indicate a strike-slip regime in which the intermediate stress (S_2) is vertical and the other two are horizontal. In cluster 7, the confidence interval shows more of a variation in the maximum compressive stress (S_1).

This cluster includes many aftershocks from the Lake Tennyson earthquake (Section 4.3.1) and the focal mechanisms display a wide range of faulting including some normal faulting events which may have influenced this result.

4.3.3 Crustal stress directions in Marlborough and Wellington computed from focal mechanism data

Michael's (1987) method of inverting focal mechanisms for stress was used on all the focal mechanism data (ALLFM and Appendix C), which included both published and catalogue data but excluded focal mechanisms computed from first motions in this study (Figure 4.1). The data were divided using the K-MEANS clustering algorithm, which yielded four clusters with centroids less than 25 km deep (Figure 4.10). A total of 177 focal mechanisms was used, with each cluster containing between 23 and 76 focal mechanisms. The results for each cluster are in Table 4.6 and Figure 4.10. All the clusters from earthquakes located in the South Island have a near-vertical intermediate stress indicating a strike-slip stress regime. The cluster in north-west Nelson has a girdle that is formed by the confidence regions of S_2 and S_3 and has the same orientation as the strike of the faults in the region; this suggests that S_{Hmax} is orthogonal to the plane of the fault. The Wellington region is different, as S_3 is subvertical indicating a reverse faulting stress regime that is likely to be due to the earthquakes occurring on the plate interface. Even though the strikes of the faults and the plate boundary change considerably over the region, each cluster yields a similar S_{Hmax} direction.

Cluster	Region	S_1		S_3		S_{Hmax}	#
		trend	plunge	trend	plunge		
1	Lake Tennyson	111	2	21	4	291	76
2	North Canterbury	297	6	27	0	297	23
3	NW Nelson	114	28	205	2	294	39
4	Wellington	129	11	9	69	307	39

Table 4.6

Stress results obtained for different clusters in Marlborough using all published focal mechanism data (ALLFM). The stress model was computed using `SLFAST`.

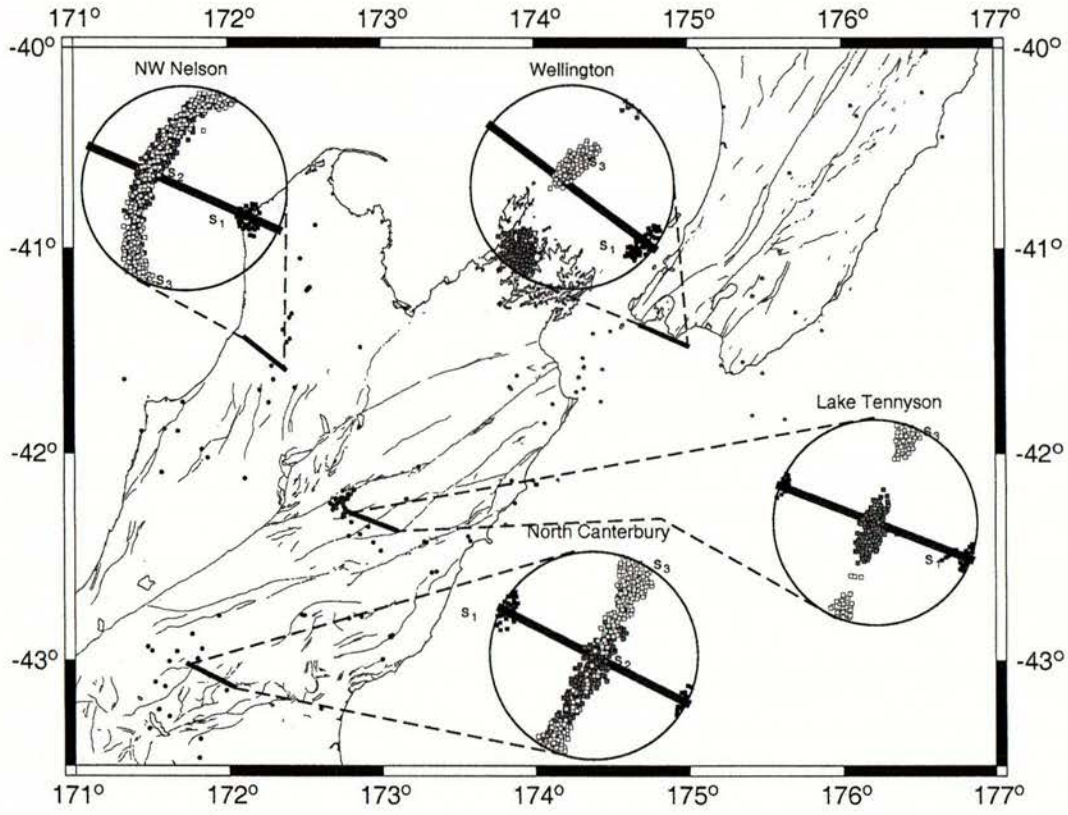

Figure 4.10 *All available focal mechanisms (ALLFM) were divided into clusters and then each cluster one was used to determine stress using the* SLFAST *algorithm. Events (dots) are colour-coded according to the cluster they are in.*

4.4 Summary

The results discussed in the previous section show a strikingly consistent S_{Hmax} direction throughout the Marlborough and Wellington regions, with an average azimuth of 295±16°and a standard error of 3°. Most of the results show that the principal stresses indicate a strike-slip regime, except for in the Wellington region, where the results indicate reverse faulting ($S_v = S_3$) that is compatible with the structural geological observations.

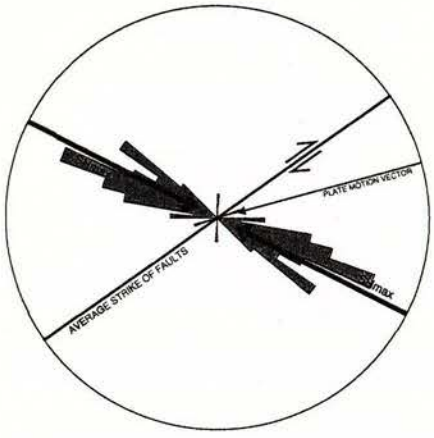

Figure 4.11 *A rose diagram of S_{Hmax} directions from all the inversions presented in the previous section. S_{Hmax} is at a high angle (60°) to the average strike of the faults (55°).*

Figure 4.11 indicates that S_{Hmax} lies at an average angle of 60° to the average strike of the major faults. This is very similar to the relative geometry observed in Southern California near the San Andreas fault, where an angle of 68±7°was determined from focal mechanisms, borehole breakouts and hydraulic fracturing experiments within 10 km of the fault (Townend and Zoback, 2004).

Three inversion techniques were tested in this study and even though most gave consistent solutions there are trade-offs involved in using each technique. Inverting directly from first motions incorporates errors that are excluded from other algorithms, such as mispicked first motions and the overall geometry of the focal mechanisms. Even though `MOTSI` outputs large confidence regions, these are probably more indicative of the real uncertainties in the stress model given the original observations than the uncertainties estimated with `SLFAST` or `FMSI`. The extra amount of computation time (40 min for `MOTSI` as opposed 10 min for `FMSI` or 10 s for `SLFAST`, on a Macintosh G4 processor) is not prohibitive it for a small data set (<300 events). We observe that the uncertainties of individual stress inversions are

reasonably large, the standard error of the calculated S_{Hmax} azimuth is only 3°, in the greater Marlborough region.

Another benefit of using the MOTSI package of programs is that one can investigate the effect of the stress constraint on focal mechanisms and investigate whether first motions are consistent with a homogenous stress field. The majority of the focal mechanisms responded well to the stress constraint by showing little or no degradation of misfit ($dS < 2.32$), when computed using a stress constraint. However, data that respond poorly to the constraint can be identified quickly by comparing the misfit with the change in focal mechanism. Therefore, by applying the stress constraint it may be possible to calculate focal mechanisms in cases which poor station coverage or mispicked first motions prevent mechanisms being computed independently.

CHAPTER 5

DISCUSSION

5.1 Crustal stress in Marlborough

To investigate tectonic stress in central New Zealand we have calculated the stress tensor from focal mechanisms and first motions (Figure 5.1). Almost all of the inversions yield strike-slip faulting regimes, except for those in the Wellington region and north-west Nelson, for which the stress inversions indicate reverse-faulting regimes. The mean S_{Hmax} direction is 295±16°and makes an angle of ~60° with the average strike of the major faults.

The optimum angle of failure (β_{opt}, the angle between S_{Hmax} and the strike of a vertical, strike-slip fault) for pre-existing faults is given in terms of the coefficient of friction by the equation below (Sibson, 1985):

$$\beta_{opt} = \frac{1}{2} tan^{-1}\left(\frac{1}{\mu}\right) \tag{5.1}$$

For a typical ("Byerlee") coefficient of friction of 0.6–1.0 (Byerlee, 1978), β_{opt} =22.5–30°. As the angle between S_{Hmax} and the average fault strike observed (β) in Marlborough is more than twice β_{opt}, the faults are certainly not optimally oriented (Sibson, 1985). This implies that the faults in the Marlborough slip in response to a relatively low ratio of shear-stress to effective normal stress, presumably because of either a low effective coefficient of friction or high pore fluid pressure.

Using a Mohr circle, we can illustrate some of the geometric relationships between faulting and stress (Figure 5.2). We use equations for a critically stressed crust described by Zoback and Townend (2001) to estimate the magnitude of the principal stresses at a mid-crustal depth of 7.5 km in a strike-slip fault regime. The Coulomb failure envelope, indicated

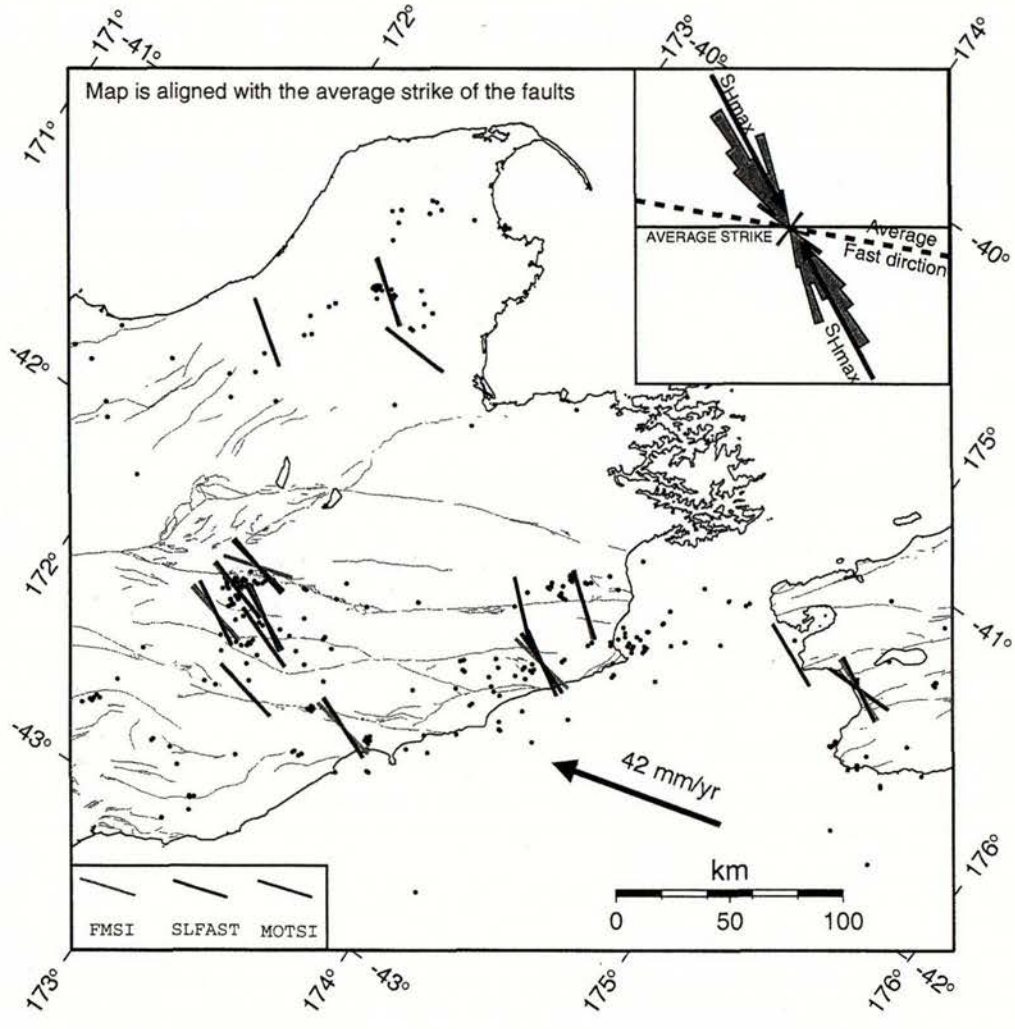

Figure 5.1 *Plot of all calculated S_{Hmax} directions obtained from stress inversions. Results (bars) are coloured according to the inversion method used;* `MOTSI` *is red,* `FMSI` *is green and* `SLFAST` *is blue. The events used in the inversions are indicated by dots. The map is aligned with the average strike of the faults, which is 55°. The inset shows a rose diagram of all the S_{Hmax} directions obtained in this study and the average orientation of the strike of faults, fast direction and S_{Hmax}.*

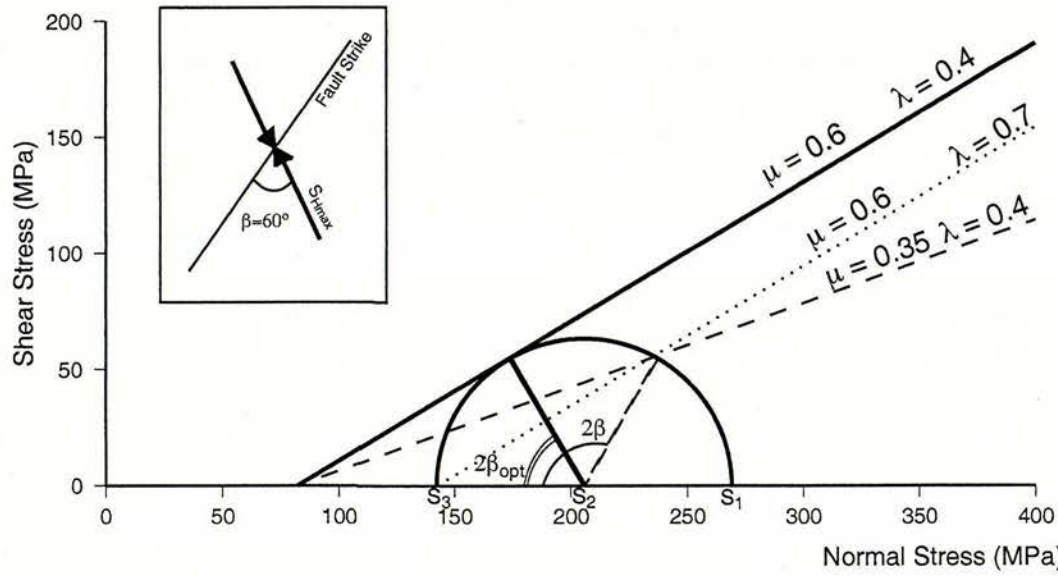

Figure 5.2 *Mohr diagram illustrating the relationship of the total stresses to faulting at 7.5 km depth. Solid lines indicates Coulomb failure criterion at near hydrostatic-pressures (with a pore fluid factor of* $\lambda = 0.4$*) and a coefficient of friction of 0.6. The dashed line indicates a coefficient of friction of 0.35 and the dotted line indicates the higher pore fluid pressure* ($\lambda = 0.7$)*, necessary to explain an angle between the fault and* S_{Hmax} *of 60°. Where the black lines intercept the circle indicates conditions for which the rock will fail. The inset is a schematic illustration of the relationship between* S_{Hmax} *and the strike of a vertical strike-slip fault.*

by the black line in Figure 5.2, delineates the shear and normal stresses necessary for frictional failure of a pre-existing fault with a coefficient of friction of 0.6 and near-hydrostatic ambient pore fluid pressures (pore fluid factor of $\lambda = 0.4$). The optimal angle for frictional failure corresponds to the situation in which the failure envelope is tangential to the Mohr circle; which in this case is $\sim 30°$. In contrast, our results suggest a mean angle of 60°, presuming the Marlborough faults to be vertical. By plotting this on the Mohr diagram, we can calculate the coefficient of friction necessary for the faults to fail under the same hydrostatic pore pressure (dashed line); in this case, the friction coefficient would have to be approximately 0.35 to explain the angle of 60° between S_{Hmax} and the fault strike. Alternatively, we can also explain the observed geometry by maintaining the friction coefficient at 0.6 but increasing the pore fluid pressure so that it equals but does not exceed S_3; this requires a pore fluid factor of $\lambda = 0.7$, which is comparable to that estimated by Prejean (2002) in the Long Valley Caldera in California. The pore fluid pressure cannot rise above S_3, as hydrofracturing would occur (Sibson, 1990) and in fact the maximum angle that S_{Hmax} can make with

the faults is 60° ($2\beta_{opt}$), unless the coefficient of friction is decreased.

Townend and Zoback (2004) concluded that the San Andreas fault is frictionally weak, as it has an S_{Hmax} direction that is at an angle of 60–85° to the local strike of the faults. In Southern California, they calculated a coefficient of friction of between 0.2–0.3, while near the San Francisco Peninsula the faults appear very weak and they estimate the coefficient of friction of at <0.1. Townend and Zoback (2004) assumed the crust adjacent to the SAF to be critically stressed with hydrostatic pore fluid pressures, as this has been observed in the Cajon Pass borehole and other continental regions (Townend and Zoback, 2000; Zoback and Townend, 2001). Our overall results from Marlborough are similar to those from Southern California, where the mean angle is 68±7°based on data within 10 km of the fault.

In northern Marlborough, we observe from the inversions that β is somewhat greater than elsewhere (60–80°), and therefore an increase in pore fluid pressure alone cannot fully explain the results. This is similar to the angles observed in the San Francisco Bay area (Townend and Zoback, 2004). Due to this upper bound on the pore pressure ($S_3 > P_f$), we must investigate the frictional properties of the faults. This analysis has been previously used by Lachenbruch and Sass (1992), Fulton *et al.* (2004) and Williams *et al.* (2004), to explain the absence of a heat flow anomaly across the San Andreas, which is usually expected for large transform faults with Byerlee's friction.

Two end-member explanations for the steep angle between S_{Hmax} and the strike of the faults, are high pore-fluid pressure or a low coefficient of friction. Sibson (1990) discussed the effect of increased pore fluid pressures on faulting and suggested that, for fault reactivation to occur on misoriented faults ($\beta_{opt} < \beta$), the pore fluid pressure conditions need to be greater than hydrostatic. He suggested these conditions could be accommodated by a "fault-valve mechanism" that allows fluid to flow up the fault zone immediately after the fault has ruptured; this occurs on pre-exisiting faults that cut across a barrier that separates hydrostatic fluid pressures close to the surface from a zone of overpressured pore fluid beneath and is most likely to occur in regions of steep-reverse faulting or vertical strike-slip faulting. Rice (1992) argued that by increasing pore fluid pressure conditions in the immediate core of the fault zone, such that P_f is higher than in the surrounding crust, the fault could slip for even higher angles of $\beta > 2\beta_{opt}$. Therefore, angles between S_{Hmax} and the strike of the faults that

are less than 60° can be explained by increasing the pore fluid pressure, but higher angles require extreme fluid pressures (Rice, 1992). Since the mean of our results is 60°, the apparent fault strength can be fully explained by either increasing the pore fluid pressure or lowering the coefficient of friction. Until we can investigate the properties of faults at depth or have high density data to investigate the stress close to the fault, it is hard to tell whether the faults are weak due to low coefficient of friction or whether the pore pressure conditions in the fault are higher than the surrounding rock. Nevertheless, studying seismic velocity and magnetotelluric anomalies near the Marlborough faults may help to address this question.

The estimated coefficient of friction on the Marlborough faults (0.35) is comparable to that observed in California (0.2–0.3) and implies that the Marlborough faults are frictionally weak. These results are similar to Liu and Bird's (2002) study of the frictional strength of faults in New Zealand, which suggested that the faults had low frictional strength on average.

5.2 Crustal anisotropy

Measurements of anisotropy in the upper crust on continents commonly show some variation, due to the crust's complex history of deformation. This is evident in our results of shear-wave splitting on local S waves in Marlborough (Figure 5.3). The overall trend of our fast direction results has a mean and standard deviation of 65±50°, and a standard error of 7°; this is parallel to the average strike of the faults (55°). There appears to be another pronounced mode almost 90° away, but it has a lot of variation and there are not enough measurements to be confident that it is a significant trend. The results do not show the fast direction aligned with S_{Hmax} or perpendicular to it, which implies that anisotropy is not due to stress-aligned cracks (Crampin, 1987; Crampin, 1994). These results are similar to those obtained by Audoine *et al.* (2000), but because our events are all shallower than 50 km, they suggest a source of anisotropy above the 50–70 km deep metamorphosed schist proposed by those authors.

The results from this study are similar to those from other studies on local S phases in central New Zealand (Gledhill, 1991; Gledhill and Stuart, 1996; Audoine *et al.*, 2000). The Tararua array shows NE–SW fast directions, which Gledhill and Stuart (1996) attributed to the geological structure. One of the stations in the North Island array shows a flip of

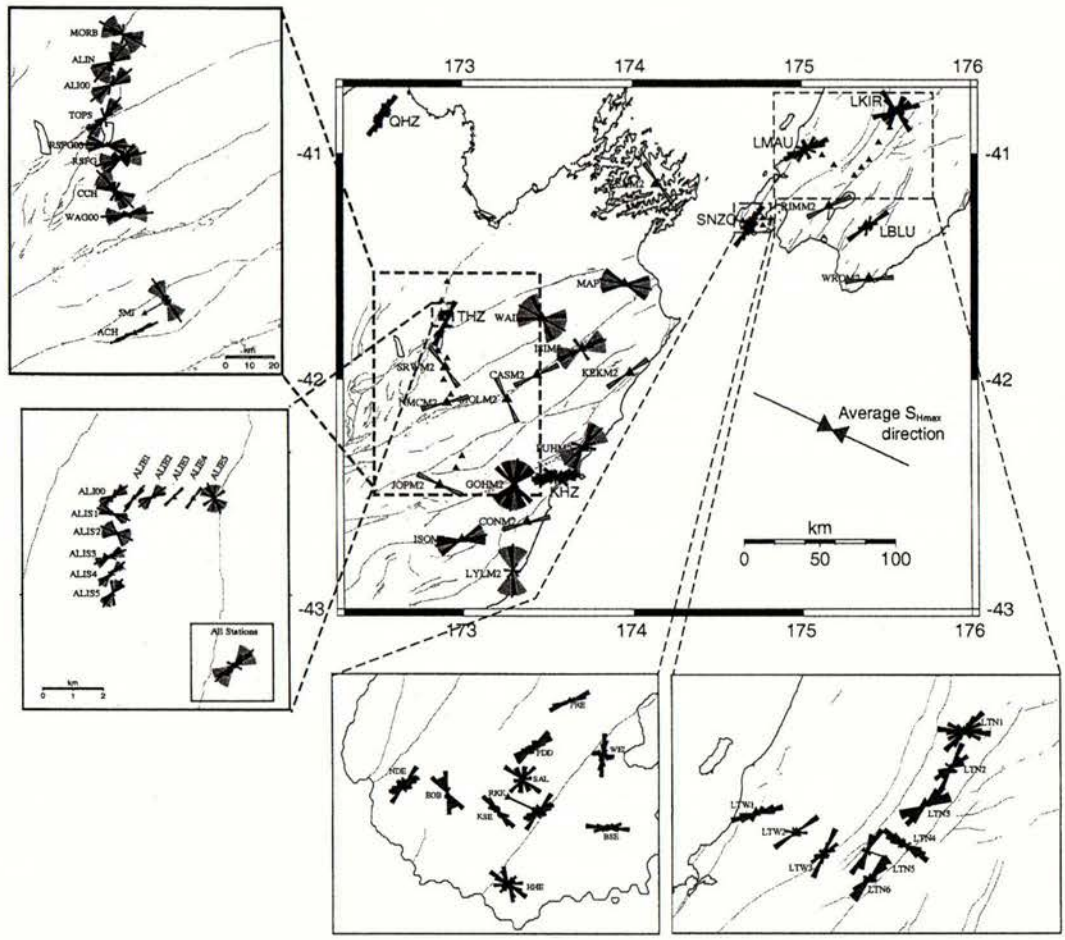

Figure 5.3 *Shear-wave splitting results from studies on local-S phases in central New Zealand. Fast directions are displayed as rose diagrams at each station (blue) and single measurements are coloured green.*

90° compared to nearby stations, which is also observed in our results. It is more difficult to compare the results from the Wellington Peninsula array with those from Marlborough as they exhibit a lot of station-to-station variation: however, the Marlborough results also show variation and four of the ten Wellington stations have northeast-trending fast directions and the delay times are similar to our results. At the station WAG, we analysed events at depths of 50–100 km so that we could compare the results with those of Audoine *et al.* (2000). At these depths the results were very similar, with larger delay times and more north-trending fast directions. This suggests that deeper events are influenced by another source of anisotropy, such as mineral alignment in the lower crust or upper mantle as evident in studies using teleseismic events (Klosko *et al.*, 1999).

Bimodal fast directions including fault-parallel have been observed in shear-wave splitting studies in California (Zhang and Schwartz, 1994; Zinke and Zoback, 1994; Cochran and Vidale, 2003; Paulssen, 2004), Brazil (do Nascimento *et al.*, 2002) and Iceland (Crampin *et al.*, 2002), but the predominant cause of crustal anisotropy is still controversial. To investigate what controls the crustal anisotropy both the geological structure and the stress field need to be defined, and even then it is only possible to distinguish between anisotropy due to structure and that due to stress if their orientations are significantly different. This is the case for both California and Marlborough, where S_{Hmax} makes an angle of 60° or more to the strike of the major faults. Results from studies in California show both fault-parallel and S_{Hmax}-parallel fast directions, which are 60°–85° apart. Zhang and Schwartz (1994) observed generally fault-parallel fast directions and attributed the anisotropy to mineral or fracture alignment due to shearing along the fault. Another direction present in their results was in the direction of S_{Hmax}, which is commonly interpreted as caused by fluid-filled stress-aligned cracks.

Zinke and Zoback (1994) analysed two clusters of earthquakes, each displaying a similar variation in fast direction to that seen in other studies. However the variation is dependant on the locations of the earthquakes, as a cluster close to the fault shows fault-parallel fast directions while the other cluster further from the fault has directions aligned with S_{Hmax}. These spatial variations are easy to identify as many measurements are observed at one station and near-station effects may be reasonably ruled out as the cause of the variation since all the measurements would be affected. In the Marlborough deployments, we are looking at a few measurements from many stations and therefore it is more difficult to detect spatial variations in anisotropy; that is we have to take into consideration the fact that the source of the differences in fast direction could be close to the station or anywhere between the source and the station. However, we do observe a fault-parallel trend as did Zinke and Zoback (1994), and this trend is especially pronounced for ray paths that go through faults just before reaching the station.

One of the more controversial interpretations of the variation in the fast direction seen in crustal anisotropy is that of Crampin *et al.* (2002), who ascribed 90° variations in fast direction observed in Iceland to high pore-fluid pressures. Crampin *et al.* (2002) only dis-

cusses this with application to regions of normal faulting and implies it is difficult to apply to other faulting regimes, since the pore-fluid pressure may have to exceed the least compressive stress direction, which would result in hydrofracturing. Although shear-wave splitting results in California display $\sim 90°$ flips in fast direction, measurements from boreholes imply that the upper crust generally has near-hydrostatic pore fluid pressure (Townend and Zoback, 2000), suggesting that high pore fluid pressure cannot entirely explain the results in California.

Seismic anisotropy measurement from the crust immediately adjacent to the San Andreas fault have been recently obtained using a dipole sonic shear velocity tool as part of the SAFOD (San Andreas Fault Observatory at Depth) pilot hole. The results show that the fast direction is subparallel to the S_{Hmax} direction and does not show the fault-parallel fast directions observed from shear-wave splitting (Boness and Zoback, 2004). The result from shear-wave splitting analysis is obtained from sampling a large portion of the crust and may sample regions that are more strongly influenced by fracturing, while the method that Boness and Zoback (2004) used may only be sampling rock in the immediate vicinity of the borehole. What will be of interest are the results from the full SAFOD project, in which measurements will be taken from within the fault zone. This may yield a better understanding of how faults directly affect anisotropy, as well as how pore-fluid pressure and stress vary across a fault zone.

5.3 Conclusions

The results relating to the initial objectives stated in Chapter 1 are the following:

1. Stress inversions on both focal mechanism and first motion data showed a mean azimuth of maximum horizontal compressive stress of $295 \pm 16°$, which makes an angle $\sim 60°$ with the average strike of the major faults. The angle between the maximum horizontal compressive stress direction and the average strike of the faults is too high to be straightforwardly reconciled with Andersonian fault slip relationships under conditions of Byerlee friction coefficients and hydrostatic pore fluid pressures. This implies that the Marlborough faults are frictionally weak and can be explained in terms of

either a moderately low coefficient of friction ($\sim$0.35) or suprahydrostatic pore fluid pressures ($\lambda \sim 0.7$).

2. The observation that faulting occurs at high angles to the maximum horizontal compressive stress direction substantiates the hypothesis that the SAF fault is not unique in being a frictionally weak fault: however it may be somewhat weaker than the Marlborough faults, at least locally, as angles of close to 85° are evident on San Fransisco Peninsula.

3. The difference between the orientation of maximum compressive stress direction and the principal geological structures allow us to distinguish between stress-related and structure related anisotropy. The results from shear-wave splitting analysis show fault-parallel fast directions and small delay times ($\sim$ 0.01 s). These observations lead to the conclusion that seismic anisotropy in the crust in Marlborough is related predominately to the geological structure and not to the ambient stress field.

By considering Fresnel zones and spatial variations in fast direction we have analysed the depth extent of the crustal anisotropy and suggest that what we have observed is associated with the upper crust (shallower than 15 km).

The results obtained at one station suggest that fast directions perpendicular to the ray paths may be due to transverse isotropy with a perpendicular axis of symmetry caused by horizontally foliated schist in the upper crust. To investigate other fast directions more thoroughly, more measurements could be made on data from the GNS short-period instruments and from the other CU/VUW short-period arrays, as not all of the available data were used in this study. The closely spaced arrays could be used to investigate a possible change in fast direction with distance from the faults and the transverse isotropy, which is suggested in this study.

CHAPTER 6

REFERENCES

Abers, G. and Gephart, J. (2001), Direct inversion of earthquake first motions for both the stress tensor and focal mechanisms and application to southern California, *Journal of Geophysical Research* **106**(B11): 26523–26540.

Anderson, E. (1951), *The dynamics of faulting and dyke formation with applications to Britian.*, Oliver and Boyd, Edinburgh.

Anderson, H., Webb, T. and Jackson, J. (1993), Focal mechanisms of large earthquakes in the South Island of New Zealand: implications for the accommodation of the Pacific-Australia plate motion, *Geophysics Journal International* **115**: 1032–1054.

Audoine, E. (2002), *Upper Mantle and Crustal Seismic Anisotropy across the Pacific-Australian plate boundary, New Zealand*, PhD thesis, Victoria University of Wellington.

Audoine, E., Savage, M. and Gledhill, K. (2000), Seismic anisotropy from local earthquakes in the transition region from a subduction to a strike-slip plate boundary, New Zealand, *Journal of Geophysical Research* **105**(B4): 8013–8033.

Babuska, V. and Cara, M. (1991), *Seismic Anisotropy in the Earth*, Kluwer Academic Publishers.

Beavan, J. and Haines, J. (2001), Contemporary horizontal velocity and strain rate fields of the Pacific-Australian plate boundary zone through New Zealand, *Journal of Geophysical Research* **106**(B1): 741–770.

Bibby, H. (1975), Crustal strain across the Marlborough faults, New Zealand, *New Zealand Journal of Geology and Geophysics* **19**(4): 407–425.

Bibby, H. (1981), Geodetically determined strain across the southern end of the Tonga-Kermadec-Hikurangi subduction zone, *Geophysical Journal of the Royal Astrological Society* **66**: 513–533.

Boness, N. and Zoback, M. D. (2004), Stress-induced seismic velocity anisotropy and physical properties in the SAFOD pilot hole in Parkfield, CA., *Geophysical Research Letters* **31**(15): L15S17.

Bott, M. (1959), The mechanics of oblique slip faulting, *Geology Magazine* pp. 109–117.

Bourne, S., Árnadóttir, T., Beavan, J., Darby, D., England, P., Parsons, B., Walcott, R. and Wood, P. (1998), Crustal deformation of the Marlborough fault zone in the South Island of New Zealand: Geodetic constraints over the interval 1982-1994, *Journal of Geophysical Research* **103**(B12): 30147–30165.

Buland and Chapman (1983), The computation of seismic travel times, *Bulletin of the Seismological Society of America* **73**: 1271–1302.

Byerlee, J. (1978), Friction of Rocks, *Pure and Applied Geophysics* **116**: 615–626.

Cochran, E. and Vidale, J. (2003), Near-fault anisotropy following the Hector Mine earthquake, *Journal of Geophysical Research* **108**(B9): 11–1 – 11–11.

Crampin, S. (1987), Geological and industrial implications of extensive-dilatancy anisotropy, *Nature* **328**: 491–496.

Crampin, S. (1994), The fracture criticality of crustal rocks, *Geophysical Journal International* **118**: 428–438.

Crampin, S., Volti, T., Chastin, S., Gudmundsson, A. and Stefánsson, R. (2002), Indication of high pore-fluid pressures in a seismically active fault zone., *Geophysical Journal International* **151**: F1–F5.

Darby, D. and Beavan, J. (2001), Evidence from GPS measurements for contemporary interplate coupling on the Southern Hikurangi subduction thrust and for partitioning of strain in the upper plate, *Journal of Geophysical Research* **106**(B12): 30881–30891.

DeMets, C., Gordon, D., Argus, D. and Stein, S. (1990), Current plate motions, *Geophysics Journal International* **101**: 425–478.

do Nascimento, A., Pearce, R. and Takeya, M. (2002), Local shear-wave observations in João Câmara, NE Brazil, *Journal of Geophysical Research* **107**(B10): 2232–2242.

Doser, D., Webb, T. and Maunder, D. (1999), Source parameters of large historical (1918-1962) earthquakes, South Island, New Zealand, *Geophysics Journal International* **139**(3): 769–794.

Dowrick, D. and Rhoades, D. (1998), Magnitudes of New Zealand earthquakes, 1901-1993, *Bulletin of the New Zealand National Society of Earthquake Engineering* **31**: 260–280.

Eberhart-Phillips, D. and Reyners, M. (1997), Continental subduction and three-dimensional crustal structure: The northern South Island, New Zealand, *Journal of Geophysical Research* **102**(B6): 11843–11861.

Evans, R. (1984), Effects of the free surface on shear wavetrains, *Geophysical Journal of the Royal Astronomical Society* **76**: 165–172.

Fulton, P., Saffer, R., Harris, R. and Bekins, B. (2004), Re-evaluation of heat flow data near Parkfield, CA., *Geophysical Research Letters* **31**(15): L15S15.

Furlong, K. and Kamp, P. (2004), Making room for the Pacific: Southward migration of subduction beneath New Zealand and tectonic consequences of delaminating the Australian lithosphere., *Eos Trans.*, number 85 in *28*, AGU, pp. T34A–05. West. Pac. Geophs. Meet. Suppl., Abstract.

Gephart, J. (1990), Stress and the direction of slip on fault planes, *Tectonics* **9**(4): 845–858.

Gephart, J. and Forsyth, D. (1984), An improved method for determining the regional stress tensor using earthquake focal mechanism data: Application to the San Fernando earthquake sequence, *Journal of Geophysical Research* **89**(B11): 9305–9320.

Gerst, A. (2003), *Temporal Changes in Seismic Anisotropy as a New Eruption Forecasting Tool?*, Master's thesis, Victoria University of Wellington.

Gledhill, K. (1991), Evidence for shallow and pervasive seismic anisotropy in the Wellington Region, New Zealand, *Journal of Geophysical Research* **96**(B13): 21503–21516.

Gledhill, K. and Stuart, G. (1996), Seismic anisotropy in the fore-arc region of the Hikurangi subduction zone, New Zealand, *Physics of the Earth and Planetary Interiors* **95**: 211–225.

Godfrey, N., Christensen, N. and Okaya, D. (2000), Anisotropy of schists: Contribution of crustal anisotropy to active source seismic experiments and shear wave splitting observations, *Journal of Geophysical Research* **105**(B12): 27991–28007.

Hickman, S. and Zoback, M. D. (2004), Stress orientations and magnitudes in the SAFOD pilot hole: Implications for the strength of the San Andreas fault at Parkfield., *Geophysical Research Letters* **31**(15): L15S12.

Holt, W. and Haines, A. (1995), The kinematics of the northern South Island, New Zealand, determined from geologic strain rates, *Journal of Geophysical Research* **100**(B9): 17991–18010.

Jones, L. (1988), Focal mechanisms and the state of stress on the San Andreas fault in southern California, *Journal of Geophysical Research* **93**: 8869–8891.

Klosko, E., Wu, F., Anderson, H., Eberhart-Phillips, D., McEvilly, E., Audoine, E., Savage, M. K. and Gledhill, K. (1999), Upper mantle anisotropy in the New Zealand region, *Geophysical Research Letters* **26**: 1496–1500.

Köhler, N. (2003), SKS wave splitting beneath the Marlborough Fault Zone, South Island, New Zealand.

Lachenbruch, A. and Sass, J. (1992), Heat flow from Cajon Pass, fault strength, and tectonic implications, *Journal of Geophysical Research* **97**(B4): 4995–5015.

Leitner, B., Eberhart-Phillips, D., Anderson, H. and Nabelek, J. (2001), A focused look at the Alpine Fault, New Zealand: Seismicity, focal mechanisms, and stress observations, *Journal of Geophysical Research* **106**(B2): 2193–2220.

Little, T. and Jones, A. (1998), Seven million years of strike-slip and related off-fault deformation, northeastern Marlborough fault system, South Island, New Zealand, *Tectonics* **17**(2): 285–302.

Liu, Z. and Bird, P. (2002), Finite element modeling of neotectonics in New Zealand, *Journal of Geophysical Research* **107**(B12,2328): 1–1 – 1–18.

Lund, B. (2000), *Crustal stress studies using microearthquakes and boreholes*, PhD thesis, Uppsala University.

Mardia, K. V. (1972), *Statistics of Directional Data*, Academic Press.

Marson-Pidgeon, K. and Savage, M. K. (1997), Frequency-dependant anisotropy in Wellington, New Zealand, *Geophysical Research Letters* **24**: 3297–3300.

Marson-Pidgeon, K., Savage, M. K., Gledhill, K. and Stuart, G. (1999), Seismic anisotropy beneath the lower half of the North Island, New Zealand, *Journal of Geophysical Research* **104**: 20277–20286.

Matcham, I. (1997), Seismic anisotropy in the Wellington region from local events recorded at the IRIS station SNZO.

Matcham, I., Savage, M. and Gledhill, K. (2000), Distribution of seismic anisotropy in the subduction zone beneath the Wellington region, New Zealand, *Geophysics Journal International* **140**(1): 1–10.

McGinty, P., Reyners, M. and Robinson, R. (2000), Stress directions in the shallow part of the Hikurangi subduction zone, New Zealand, from inversion of earthquake first motions, *Geophysics Journal International* **142**(2): 339–350.

McGinty, P., Robinson, R., Taber, J. and Reyners, M. (1997), The 1990 Lake Tennyson earthquake sequence, Marlborough, New Zealand, *New Zealand Journal of Geology and Geophysics* **40**: 521–535.

McKenzie, D. (1969), The relation between fault plane solutions for earthquakes and the direction of the principal stresses, *Bulletin of the Seismological Society of America* **59**(2): 591–601.

Michael, A. (1984), Determination of stress from slip data: faults and folds, *Journal of Geophysical Research* **89**(B13): 11517–11526.

Michael, A. (1987), Use of focal mechanisms to determine stress: A control study, *Journal of Geophysical Research* **92**(B1): 357–368.

Nicol, A. and Wise, D. (1992), Paleostress adjacent to the Alpine fault of New Zealand: Fault, Vein, and Styolite data from the Doctors Dome area, *Journal of Geophysical Research* **97**(B12): 12685–17692.

Nuttli, O. W. (1961), The effect of the Earth's surface on the S wave particle motion, *Bulletin of the Seismological Society of America* **51**: 237–246.

Okaya, D., Christensen, N., Stanley, D. and Stern, T. (1995), Crustal anisotropy in the vicinity of the Alpine Fault, South Island, New Zealand, *New Zealand of Geology and Geophysics* **38**: 579–583.

Paulssen, H. (2004), Crustal Anisotropy in southern California from local earthquake data, *Geophysical Research Letters* **31**(L01601,doi:10.1029/2003GL018654): 1–4.

Pettinga, J. and Wise, D. (1994), Paleostress adjacent to the Alpine fault: Broader implications from fault analysis near Nelson, South Island, New Zealand, *Journal of Geophysical Research* **99**(B2): 2727–2736.

Prejean, S. (2002), *The interaction of tectonic and magmatic processes in the Long Valley Caldera, California*, PhD thesis, Stanford University.

Provost, A. and Houston, H. (2001), Orientation of the stress field surrounding the creeping section of the San Andreas fault: Evidence for a narrow mechanically weak zone, *Journal of Geophysical Research* **106**(B6): 11373–11386.

Reilly, W. (1990), Horizontal crustal deformation on the Hikurangi Margin, *New Zealand Journal of Geology and Geophysics* **33**: 393–400.

Reyners, M. (1998), Plate coupling and the hazard of large subduction thrust earthquakes at the Hikurangi subduction zone, New Zealand, *New Zealand Journal of Geology and Geophysics* **41**: 343–354.

Reyners, M. and de J. Robertson, E. (2004), Intermediate depth earthquakes beneath Nelson, New Zealand, and the southwestern termination of the subducted Pacific Plate, *Geophysical Research Letters* **31**: L04607.

Reyners, M., Robinson, R. and McGinty, P. (1997), Plate coupling in the northern South Island and the southernmost North Island, New Zealand, as illuminated by earthquake focal mechanisms, *Journal of Geophysical Research* **102**(B7): 15197–15210.

Rice, J. (1992), Fault stress states, pore pressure distributions, and the weakness of the San Andreas fault, *in* B. Evans and T.-F. Wong (eds), *Fault mechanics and transport properties of rocks*, Vol. 51, Academic Press.

Robinson, R. (1986), Seismicity, structure and tectonics of the Wellington region, New Zealand, *Geophysical Journal of the Royal Astrological Society* **87**: 379–409.

Robinson, R. and McGinty, P. (2000), The enigma of the Arthur's Pass, New Zealand, earthquake 2. The aftershock distribution and its relation to regional and induced stress fields, *Journal of Geophysical Research* **105**(B7): 16139–16150.

Sheriff, R. and Geldart (1995), *Exploration Seismology, 2nd edition*, Cambridge University Press.

Sibson, R. (1985), A note on fault reactivation, *Journal of Structural Geology* **7**(6): 751–754.

Sibson, R. (1990), Faulting and fluid flow, *in* B. Nesbitt (ed.), *Short course on fluids in tectonically active regimes of continental crust*, Vol. 18, Mineralogical Association of Canada.

Silver, P. and Chan, W. (1991), Shear-wave splitting and subcontinental mantle deformation, *Journal of Geophysical Research* **96**: 16429–16454.

Smith, G. and Ekström, G. (1999), A global study of P_n anisotropy beneath continents, *Journal of Geophysical Research* **104**(B1): 963–980.

Stein, S. and Wysession, M. (2003), *An introduction to seismology, earthquakes and earth structure*, Blackwell Publishing.

Sutherland, R. (1999), Cenezoic bending of New Zealand basement terranes and Alpine Fault displacement: a brief review, *New Zealand Journal of Geology and Geophysics* **42**: 295–301.

Tapley, W., Tull, J., Miner, L. and Goldstein, P. (1990), SAC command reference manual version 10.5.

Teanby, N., Kendall, J.-M. and van der Baan, M. (2004), Automation of shear-wave splitting measurements using cluster analysis, *Bulliten of the Seismological Society of America* **94**(2): 453–463.

Townend, J. (2003), *Mechanical constraints on the strength of the lithosphere and plate bounding faults.*, PhD thesis, Stanford University.

Townend, J. and Zoback, M. D. (2000), How faulting keeps the crust strong, *Geology* **28**: 399–402.

Townend, J. and Zoback, M. D. (2001), Implications of earthquake focal mechanisms for the frictional strength of the San Andreas fault system, *in* R. Holdsworth (ed.), *The*

Nature and Significance of Fault Zone Weakening, Vol. 186, Geolological Society of London Special Publication.

Townend, J. and Zoback, M. D. (2004), Regional tectonic stress near the San Andreas fault in central and southern California., *Geophysical Research Letters* **31**(15): L15S11.

Walcott, R. (1984), The kinematics of the plate boundary zone through New Zealand: a comparison of short- and long-term deformations, *Geophysical Journal of the Royal Astrological Society* **79**: 613–633.

Wallace, R. (1951), Geometry of shearing stress and relation to faulting, *Journal of Geology* **59**: 118–130.

Webb, T. and Anderson, H. (1998), Focal mechanisms of large earthquakes in the North Island of New Zealand: slip partitioning at an oblique active margin, *Geophysical Journal International* **134**: 40–86.

Williams, C., Grubb, F. and Galanis Jr., S. (2004), Heat flow in the SAFOD pilot hole and implications for the strength of the San Andreas Fault, *Geophysical Research Letters* **31**(15): L15S14.

Yeats, R. and Berryman, K. (1987), South Island, New Zealand, and Transverse Ranges, California: a seismotectonic comparison, *Tectonics* **6**(3): 363–376.

Zhang, Z. and Schwartz, S. (1994), Seismic anisotropy in the shallow crust of the Loma Prieta segment of the San Andreas fault system, *Journal of Geophysical Research* **99**(B5): 9651–9661.

Zinke, J. and Zoback, M. D. (1994), Stucture-related and stress-induced shear-wave velocity anisotropy: Observations from microearthquakes near the Calaveras Fault in Central California, *Bulletin of the Seismological Society of America* **90**(5): 1305–1312.

Zoback, M. D. and Townend, J. (2001), Implications of hydrostatic pore pressures and high crustal strength for the deformation of intraplate lithosphere, *Tectonophysics* **336**: 19–30.

Zoback, M. D. and Zoback, M. L. (2002), Stress in the Earth's Lithosphere, *Encyclopedia of Physical Science and Technology*, Vol. 16, Academic Press.

Zoback, M. L. (1992), First- and second-order patterns of stress in the lithosphere: The world stress map project, *Journal of Geophysical Research* **97**(B8): 11703–11728.

APPENDIX A

PUBLISHED FOCAL MECHANISM DATA

This appendix lists all published focal mechanism data used in this study. Some events have had multiple methods or multiple sources determining the focal mechanism.

Event	Event name as called in published source.
Long	Earthquake Longitude.
Lat	Earthquake Latitude.
Depth	Earthquake Depth in kilometers.
Strike	Strike of nodal plane.
Dip	Dip of nodal plane.
Rake	Rake of nodal plane.
Mw	Body wave magnitude of earthquake.
Source	Reference of published data.
Date	Date of earthquake given by YYMMDD or YYMMDDHOUR.

Table A.1: Summary of published focal mechanisms

Event	Long	lat	Depth(km)	strike	dip	rake	Mw	Source	Date
B	174.1	-42.74	16	110	55	297	6.1	Anderson et al (1993)	650411
C	174.4	-41.63	19	232	68	133	5.8	Anderson et al (1993)	660423
D	171.96	-41.76	10	232	51	103	7.1	Anderson et al (1993)	680523
F	172.1	-42.13	9	242	83	207	5.7	Anderson et al (1993)	710813
I	170.56	-43.6	13	62	83	206	6.1	Anderson et al (1993)	840624
M	172.74	-42.32	8	55	89	163	5.9	Anderson et al (1993)	900210
N	171.58	-41.89	10	42	30	99	5.8	Anderson et al (1993)	910128a
O	171.67	-41.9	12	8	48	77	6	Anderson et al (1993)	910128b
MO	173	-43	20	72	90	170	6.4	Doser et al (1999)	221225
			23	60	90	170	6.6	Doser et al (1999)	
AP	171.93	-42.79	11	65	90	-178	7	Doser et al (1999)	290309
			12	57	89	-169	7	Doser et al (1999)	
B1	172.2	-41.7	9	358	46	69	7.3	Doser et al (1999)	290616
			9	356	52	67	7.3	Doser et al (1999)	
B2	172.43	-41.69	11	21	45	80	6.3	Doser et al (1999)	290619
			5	22	45	79	6.4	Doser et al (1999)	
B3	172.86	-41.49	14	321	42	79	6.5	Doser et al (1999)	290622
			14	342	48	157	6.6	Doser et al (1999)	
B4	172.85	-41.88	7	350	32	83	6.4	Doser et al (1999)	290622
			6	32	54	142	6.6	Doser et al (1999)	
B5	172.29	-41.65	19	21	29	120	6.3	Doser et al (1999)	290715
			17	20	30	120	6.4	Doser et al (1999)	
WA	172.99	-42.48	4	64	90	177	6.4	Doser et al (1999)	480522
			3	223	89	180	6.6	Doser et al (1999)	
WE	171.32	-41.65	7	55	40	88	5.6	Doser et al (1999)	621510
			11	54	38	88	5.8	Doser et al (1999)	
1	172.396	-41.347	2.1	255	30	112.5	3.3	Reyners et al (1997)	9401011457
2	172.572	-40.890	2.3	120	30	-15	2.7	Reyners et al (1997)	9402260614
3	173.238	-42.075	3.2	210	52	60	3.3	Reyners et al (1997)	9402160840
4	172.660	-42.252	3.7	247.5	75	-135	3	Reyners et al (1997)	9402280616
5	172.376	-41.466	4.4	217.5	60	45	4.1	Reyners et al (1997)	9310231226

continued on next page...

Event	Long	lat	Depth(km)	strike	dip	rake	Mw	Source	Date
6	172.400	-41.450	5.0	97.5	67.5	135	4.1	Reyners et al (1997)	9310241655
7	172.490	-42.790	5.0	157.5	60	37.5	4	Reyners et al (1997)	9312022204
8	172.490	-42.790	5.0	60	67	180	3.5	Reyners et al (1997)	9312050718
9	172.696	-42.236	5.4	255	75	150	2.8	Reyners et al (1997)	9311240821
10	172.279	-41.583	5.4	45	68	105	2.9	Reyners et al (1997)	9402150547
11	172.907	-42.366	5.6	97.5	75	-165	2.7	Reyners et al (1997)	9311201120
12	174.313	-41.542	6.1	270	53	-157.5	2.7	Reyners et al (1997)	9311140006
13	172.814	-42.188	6.8	165	83	-22.5	2.9	Reyners et al (1997)	9401240712
14	172.706	-42.240	7.0	307.5	83	-7.5	3.2	Reyners et al (1997)	9401211702
15	173.864	-42.25	7.3	270	68	-172.5	2.8	Reyners et al (1997)	9311011349
16	172.705	-42.232	7.3	330	83	22.5	2.8	Reyners et al (1997)	9311040014
17	173.066	-42.886	7.3	75	60	150	2.9	Reyners et al (1997)	9312121958
18	173.863	-40.949	7.3	315	75	-45	2.9	Reyners et al (1997)	9403031152
19	173.983	-42.139	7.6	30	68	105	4	Reyners et al (1997)	9312161053
20	172.596	-43.236	7.9	75	90	-135	2.7	Reyners et al (1997)	9403092156
21	173.056	-42.897	8.0	165	38	45	4.2	Reyners et al (1997)	9312142351
22	172.413	-41.327	8.3	127.5	23	-30	3	Reyners et al (1997)	9401011806
23	173.323	-42.584	8.4	240	45	157.5	2.8	Reyners et al (1997)	9401181649
24	172.511	-41.213	8.4	45	68	82.5	2.8	Reyners et al (1997)	9402082118
25	173.053	-42.896	8.5	37.5	68	127.5	4	Reyners et al (1997)	9312141903
26	173.160	-42.231	8.6	52.5	83	142.5	2.7	Reyners et al (1997)	9311292342
27	172.257	-41.761	8.6	217.5	60	45	3.5	Reyners et al (1997)	9311150248
28	173.049	-42.893	8.7	75	90	135	3.3	Reyners et al (1997)	9312310150
29	173.052	-42.894	8.9	165	45	7.5	3.4	Reyners et al (1997)	9312181613
30	172.704	-42.234	8.9	277.5	23	-60	3.3	Reyners et al (1997)	9402102135
31	173.999	-42.160	8.9	360	68	82.5	3.9	Reyners et al (1997)	9312011024
32	172.813	-42.189	9.1	157.5	60	-22.5	2.9	Reyners et al (1997)	9401011818
33	173.354	-42.580	9.2	202.5	53	37.5	2.8	Reyners et al (1997)	9402262014
34	174.271	-41.708	9.2	60	45	120	3.8	Reyners et al (1997)	9401120613
35	172.773	-42.209	9.3	247.5	83	-165	3.5	Reyners et al (1997)	9402012109
36	172.863	-42.796	9.3	352.5	60	22.5	3.3	Reyners et al (1997)	9311080400
37	172.524	-41.206	9.5	60	75	127.5	3.7	Reyners et al (1997)	9402082102
38	172.943	-42.440	9.6	352.5	68	-52.5	3	Reyners et al (1997)	9312032052
39	174.008	-42.161	9.7	172.5	75	-22.5	2.9	Reyners et al (1997)	9312032220

continued on next page...

Event	Long	lat	Depth(km)	strike	dip	rake	Mw	Source	Date
40	172.521	-41.208	9.9	165	45	15	3.3	Reyners et al (1997)	9401050537
41	172.520	-41.206	10.2	157.5	38	15	4	Reyners et al (1997)	9312051244
42	172.520	-41.205	10.4	75	83	127.5	3	Reyners et al (1997)	9401081527
43	172.520	-41.204	10.4	165	45	22.5	3.3	Reyners et al (1997)	9401301203
44	172.470	-41.057	10.6	82.5	68	120	2.7	Reyners et al (1997)	9311010642
45	172.533	-41.200	10.6	60	68	135	3.7	Reyners et al (1997)	9401102314
46	174.285	-41.636	10.7	255	60	-172.5	4.5	Reyners et al (1997)	9311212001
47	172.523	-41.206	10.9	172.5	45	7.5	3.2	Reyners et al (1997)	9401120608
48	172.519	-41.206	11.0	255	75	135	2.8	Reyners et al (1997)	9312181209
49	172.524	-41.203	11.1	60	68	135	2.9	Reyners et al (1997)	9402190852
50	174.287	-41.634	11.3	270	68	165	3.4	Reyners et al (1997)	9311212222
51	173.276	-42.437	11.3	195	75	-15	2.9	Reyners et al (1997)	9311040402
52	175.475	-41.616	11.8	150	8	30	3.2	Reyners et al (1997)	9401160244
53	173.290	-42.440	11.9	90	23	-165	5	Reyners et al (1997)	9311032332
54	173.284	-42.438	11.9	255	83	-165	2.1	Reyners et al (1997)	9311032335
55	172.528	-41.201	12.1	60	75	142.5	2.8	Reyners et al (1997)	9402240911
56	174.148	-42.134	12.2	277.5	30	142.5	3	Reyners et al (1997)	9311201812
57	172.354	-41.405	12.3	172.5	60	52.5	2.9	Reyners et al (1997)	9402161437
58	174.441	-41.596	12.9	255	53	142.5	3.1	Reyners et al (1997)	9401090511
59	173.561	-42.411	13.2	232.5	45	112.5	4.1	Reyners et al (1997)	9402181336
60	173.844	-42.141	13.2	52.5	45	180	2.8	Reyners et al (1997)	9401230156
61	172.854	-42.401	13.5	255	68	-142.5	2.9	Reyners et al (1997)	9312271746
62	174.061	-41.859	13.9	262.5	68	-157.5	3.2	Reyners et al (1997)	9401240319
63	172.781	-42.804	14.1	217.5	68	-172.5	3	Reyners et al (1997)	9312050851
64	173.573	-42.433	14.5	7.5	75	53	4.5	Reyners et al (1997)	9402110907
65	175.692	-41.316	14.7	52.5	90	90	3.7	Reyners et al (1997)	9402190407
66	172.472	-42.787	15.5	165	38	15	2.8	Reyners et al (1997)	9312030649
67	175.865	-41.405	15.9	97.5	60	-142.5	3.1	Reyners et al (1997)	9403140936
68	173.881	-41.626	16.0	330	60	-22.5	3.1	Reyners et al (1997)	9312102226
69	174.318	-41.690	16.0	345	83	45	2.8	Reyners et al (1997)	9312190423
70	174.116	-41.765	16.1	232.5	68	172.5	3.4	Reyners et al (1997)	9311290016
71	173.833	-41.681	16.1	330	45	-37.5	3.2	Reyners et al (1997)	9312230719
72	174.320	-41.690	16.2	240	53	157.5	3	Reyners et al (1997)	9312190227
73	175.208	-41.577	17.2	157.5	8	45	2.8	Reyners et al (1997)	9312241944

continued on next page...

Event	Long	lat	Depth(km)	strike	dip	rake	Mw	Source	Date
74	173.841	-41.692	17.5	90	68	-150	2.8	Reyners et al (1997)	9312230721
75	175.212	-41.576	17.5	135	8	30	2.9	Reyners et al (1997)	9312190632
76	174.380	-41.420	18.7	262.5	68	-30	2.8	Reyners et al (1997)	9311210627
77	175.415	-41.238	20.8	60	23	-90	2.9	Reyners et al (1997)	9312210036
78	175.408	-41.820	21.1	15	8	-97.5	3.4	Reyners et al (1997)	9402130158
79	174.574	-41.378	21.8	217.5	45	127.5	2.9	Reyners et al (1997)	9311200652
80	174.495	-41.410	21.9	7.5	68	60	2.7	Reyners et al (1997)	9401040044
81	174.321	-41.584	22.6	277.5	15	150	3	Reyners et al (1997)	9401080011
82	173.805	-42.350	23.1	210	75	-127.5	2.7	Reyners et al (1997)	9311020817
83	174.320	-41.589	23.2	202.5	23	112.5	3.1	Reyners et al (1997)	9402031412
84	174.564	-41.391	23.5	352.5	60	52.5	3.1	Reyners et al (1997)	9311220200
85	175.593	-41.018	24.4	232.5	8	105	2.8	Reyners et al (1997)	9403130350
86	174.430	-41.752	24.9	67.5	45	-52.5	3.3	Reyners et al (1997)	9310291642
87	174.852	-41.282	25.1	270	38	157.5	2.8	Reyners et al (1997)	9401260506
88	175.272	-41.250	25.2	240	15	97.5	2.7	Reyners et al (1997)	9310291827
89	174.286	-42.019	25.2	67.5	68	-75	2.9	Reyners et al (1997)	9312311949
90	175.270	-41.277	25.6	90	23	-82.5	2.8	Reyners et al (1997)	9312080209
91	175.270	-41.278	25.6	105	30	-67.5	2.7	Reyners et al (1997)	9312080210
92	175.264	-41.284	25.9	247.5	83	-105	3.5	Reyners et al (1997)	9312080204
93	173.477	-42.617	26.6	67.5	45	-90	3.4	Reyners et al (1997)	9401070340
94	173.353	-42.566	26.9	285	53	-45	3.4	Reyners et al (1997)	9402222203
95	173.279	-42.599	27.2	135	83	67.5	2.9	Reyners et al (1997)	9311101537
96	175.493	-41.102	27.9	352.5	30	-157.5	4	Reyners et al (1997)	9312101540
97	174.768	-41.667	28.3	67.5	30	-60	4	Reyners et al (1997)	9401152112
98	174.443	-41.878	28.3	202.5	75	142.5	2.9	Reyners et al (1997)	9312072158
99	174.889	-41.401	28.4	315	30	127.5	2.9	Reyners et al (1997)	9311281831
100	174.411	-41.864	28.6	7.5	53	180	2.7	Reyners et al (1997)	9310300255
101	174.717	-41.514	28.9	7.5	23	-105	3.3	Reyners et al (1997)	9402081004
102	175.360	-40.872	29.3	202.5	45	142.5	2.8	Reyners et al (1997)	9311071005
103	173.645	-42.080	30.8	97.5	68	-15	2.9	Reyners et al (1997)	9401202251
104	174.505	-41.800	30.9	75	60	-52.5	2.7	Reyners et al (1997)	9310210708
105	175.356	-40.790	31.3	315	45	142.5	2.9	Reyners et al (1997)	9310282033
106	174.525	-41.681	31.6	150	23	157.5	2.8	Reyners et al (1997)	9312130556
107	173.342	-42.165	31.9	105	75	-15	3.1	Reyners et al (1997)	9311070127

continued on next page...

Event	Long	lat	Depth(km)	strike	dip	rake	Mw	Source	Date
108	173.517	-42.167	32.1	202.5	30	-165	2.8	Reyners et al (1997)	9403070241
109	173.706	-41.906	32.6	90	53	-37.5	2.7	Reyners et al (1997)	9310310037
110	174.079	-41.668	32.6	22.5	83	180	3	Reyners et al (1997)	9403090434
111	173.678	-41.911	33.2	97.5	45	-22.5	3	Reyners et al (1997)	9402070443
112	175.063	-40.922	33.2	127.5	83	-37.5	2.8	Reyners et al (1997)	9310281352
113	173.680	-41.909	33.3	97.5	45	-22.5	3.4	Reyners et al (1997)	9402121204
114	173.006	-42.818	33.7	330	38	120	2.9	Reyners et al (1997)	9403100919
115	172.894	-42.764	35.4	150	68	37.5	2.7	Reyners et al (1997)	9311081717
116	175.177	-40.796	36.0	217.5	60	-127.5	2.8	Reyners et al (1997)	9312190902
117	174.243	-41.389	36.5	82.5	23	-37.5	2.8	Reyners et al (1997)	9312302050
118	174.481	-41.172	37.2	67.5	8	45	3.2	Reyners et al (1997)	9312150020
119	174.447	-41.191	37.5	105	45	-60	2.8	Reyners et al (1997)	9312050047
120	174.031	-41.447	40.5	15	30	-112.5	3.4	Reyners et al (1997)	9312021055
121	173.581	-41.813	40.7	292.5	38	-105	4.4	Reyners et al (1997)	9310241816
122	173.424	-41.924	41.5	30	75	150	2.7	Reyners et al (1997)	9312201614
123	174.154	-41.473	41.8	22.5	60	105	3	Reyners et al (1997)	9403012327
124	174.376	-41.056	42.5	232.5	53	-157.5	3.1	Reyners et al (1997)	9401231454
125	173.562	-41.736	45.1	322.5	23	-157.5	2.8	Reyners et al (1997)	9311220742
126	173.332	-41.909	45.3	142.5	45	22.5	2.8	Reyners et al (1997)	9312270643
127	174.138	-41.326	45.3	45	90	105	3.2	Reyners et al (1997)	9312300724
128	174.814	-40.798	45.7	255	53	-67.5	2.8	Reyners et al (1997)	9403051530
129	173.813	-41.614	46.0	157.5	60	67.5	2.8	Reyners et al (1997)	9312271211
130	174.212	-40.770	47.3	75	68	-60	2.9	Reyners et al (1997)	9311181856
131	174.255	-40.742	48.9	120	75	-120	2.9	Reyners et al (1997)	9311041206
132	174.833	-41.121	52.9	60	30	-82.5	3	Reyners et al (1997)	9403040637
133	174.837	-41.119	53.2	277.5	83	-15	4.5	Reyners et al (1997)	9402281022
134	174.398	-41.208	55.0	322.5	83	37.5	3.7	Reyners et al (1997)	9403051233
135	174.486	-41.294	57.1	97.5	30	-60	3.3	Reyners et al (1997)	9312190345
136	174.127	-41.688	57.4	157.5	45	52.5	3.1	Reyners et al (1997)	9402221840
137	174.496	-41.136	58.2	285	60	-67.5	3.3	Reyners et al (1997)	9402072221
138	174.366	-41.465	61.2	210	60	165	3.4	Reyners et al (1997)	9401212249
139	174.524	-41.100	62.1	105	23	-52.5	3	Reyners et al (1997)	9311271732
140	173.495	-41.674	67.8	240	68	-135	3.1	Reyners et al (1997)	9310221034
141	172.830	-42.023	72.4	127.5	83	30	3.6	Reyners et al (1997)	9402081011

continued on next page...

Event	Long	lat	Depth(km)	strike	dip	rake	Mw	Source	Date
142	172.844	-41.627	76.1	210	45	-157.5	3.2	Reyners et al (1997)	9311060846
143	173.235	-41.794	81.9	37.5	75	127.5	3	Reyners et al (1997)	9312160300
144	173.563	-41.187	84.1	120	75	7.5	3.3	Reyners et al (1997)	9310261106
145	173.219	-41.828	87.5	352.5	45	135	3.7	Reyners et al (1997)	9311190843
1000	174.29	-41.76	26	70	24	-57	6.1	Harvard CMT catalog	770118
1001	171.54	-42.46	59	345	57	9	5	Harvard CMT catalog	790324
1002	175.27	-40.18	45	153	11	14	5.4	Harvard CMT catalog	800623
1003	176.66	-40.45	15	146	11	28	5.4	Harvard CMT catalog	800703
1004	175.66	-40.63	15	263	9	145	5.4	Harvard CMT catalog	811227
1005	175.48	-41.15	15	62	28	-74	5.3	Harvard CMT catalog	820205
1006	173.68	-40.41	94	125	23	-3	5.2	Harvard CMT catalog	840103
1007	172.74	-42.19	15	65	54	-167	5.7	Harvard CMT catalog	900210
1008	176.09	-40.76	32	81	28	-41	6.2	Harvard CMT catalog	900219
	176.102	-40.347	20	91	16	-51	6.3	NEIC	
1009	176.53	-40.23	16	220	28	149	6.4	Harvard CMT catalog	900513
	176.064	-40.296	23	220	48	143	6.4	NEIC	
1010	176.28	-40.56	32	72	35	-75	5.1	Harvard CMT catalog	901219
1011	175.62	-41.84	15	190	21	58	5.5	Harvard CMT catalog	901004
1012	175.35	-41.56	20	250	38	145	5.4	Harvard CMT catalog	901006
1013	171.7	-41.76	15	66	42	136	5.7	Harvard CMT catalog	910128C
1014	171.86	-42.03	15	229	34	121	5.8	Harvard CMT catalog	910128D
1015	171.43	-41.9	15	213	37	90	5.4	Harvard CMT catalog	910215
	171.56	-42.1	15	213	37	90	5.4	Dowrick & Rhoades (1998)	
1016	174.94	-40.69	70	232	27	50	5.6	Harvard CMT catalog	910908
1017	176.29	-40.65	30	76	17	-52	5.5	Harvard CMT catalog	920302
1018	171.61	-43.01	15	70	19	134	5.5	Harvard CMT catalog	920330
1019	173.71	-41.65	75	29	72	178	5.9	Harvard CMT catalog	920527
	173.727	-41.616	77	31	74	175	6	NEIC	
1020	171.47	-42.94	15	68	63	150	6.7	Harvard CMT catalog	940618
	171.658	-42.963	24	346	29	56	6.7	NEIC	
1021	174.17	-40.89	90	282	63	150	5.8	Harvard CMT catalog	950322
1022	171.76	-42.88	15	166	60	12	6.1	Harvard CMT catalog	951124
	171.793	-42.9984	13	166	84	4	6.2	NEIC	
1023	172.9	-42.41	31	317	67	-20	5.2	Harvard CMT catalog	960829

continued on next page...

Event	Long	lat	Depth(km)	strike	dip	rake	Mw	Source	Date
1024	173.34	-41.19	79	124	42	12	5.2	Harvard CMT catalog	971129
1025	173.4	-41.28	60	357	12	-123	5.2	Harvard CMT catalog	990103
1026	175.47	-40.93	46	54	14	-76	5.2	Harvard CMT catalog	000329
1027	176.13	-40.44	38	252	51	-42	5.2	Harvard CMT catalog	030125
1028	171.48	-43.33	10	92	34	164	5.2	Harvard CMT catalog	770511
	171.98	-43.15	10	92	34	164	5.2	Dowrick & Rhoades (1998)	
1029	172.78	-42.41	15	67	56	-174	6	Harvard CMT catalog	900210
	172.798	-42.343	14	63	78	-180	6	NEIC	
1030	171.54	-43.24	15	172	74	2	5.9	Harvard CMT catalog	940619
	171.611	-43.273	14	174	87	25	6	NEIC	
	171.58	-43.13	15	172	74	2	5.9	Dowrick & Rhoades (1998)	
1031	171.81	-43.38	15	168	49	16	5.4	Harvard CMT catalog	940621
	171.52	-43.11	15	168	49	16	5.4	Dowrick & Rhoades (1998)	
1032	171.8	-43.47	15	53	67	174	5.5	Harvard CMT catalog	950529
	171.5	-42.96	15	53	67	174	5.5	Dowrick & Rhoades (1998)	
1033	176.33	-40.08	27	234	1	111	5.3	Harvard CMT catalog	010924
CA	171.82	-42.95	3	176	45	44	6.2	Gledhill et al (1996)	
I2	171.82	-41.99	11	179	49	72	5.8	Webb & Anderson (1998)	
H	175.93	-40.34	38	250	56	257	5.6	Webb & Anderson (1998)	

Table A.1: **List of all focal mechanisms**

APPENDIX B

SHEAR-WAVE SPLITTING MEASUREMENTS

This appendix contains the results of the shear-wave splitting measurements obtained using the automated shear-wave splitting program (Teanby *et al.*, 2004) on the three deployments in Marlborough. A description of the parameters in the table is below.

Station	Name of the station.
Event	Number that identifies the each event. It reflects the time of the event which consists of: <year><julian day><hour>.
Qual	Quality of measurement described in 3.3 section.
ϕ	fast direction in degrees.
$\pm\phi$	95% confidence interval of the fast direction in degrees.
δt	Delay time in seconds.
$\pm\delta t$	95% confidence interval of the delay time in seconds.
Baz	Back azimuth of the hypocenter.
Pol	Polarization.
Slow	Slowness or ray parameter in seconds per degree.
Incid	Incidence angle in degrees.
Filter	Bandpass frequency filter values in Hz.
Ede	Earthquake depth in kilometers.
Elat	Earthquake latitude.
Elong	Earthquake longitude.
Edist	Earthquake distance in kilometers.

Table B.1: Summary of splitting measurements for broadband instruments.

Station	Event	Qual	ϕ	$\pm\phi$	δt	$\pm\delta t$	Baz	Pol	Slow	Incid	Filter	Ede	Elat	Elong	Edist
5MI	200204205	A	-63	9	0.043	0.013	224	41	0.283	48.6	1–3	5	-42.473	172.813	21.5
5MI	200204809	A	-31	8	0.056	0.167	39	39	0.285	49.1	None	9	-41.980	173.380	50.2
5MI	200206220	A	-31	6	0.063	0.002	33	29	0.285	49.1	1–3	5	-42.120	173.182	28.4
5MI	200207915	A	-14	10	0.031	0.003	317	32	0.156	24.4	1–3	33	-42.183	172.808	22.9
ACH	200204622	A	61	2	0.063	0.000	204	198	0.135	20.9	1–6	33	-42.543	172.869	18.7
CCH	200111623	A	-26	18	0.038	0.0125	136	35	0.286	49.4	1–3	5	-42.189	173.134	28.9
CCH	200114608	A	-77	3	0.063	0.000	153	56	0.252	42.0	2–5	33	-42.615	173.321	76.8
RSFG	200111623	A	-52	8	0.100	0.005	149	80	0.286	49.4	1–3	5	-42.189	173.134	36.3
RSFG	200121104	A	-76	12	0.044	0.003	298	45	0.278	47.5	2–6	12	-41.726	172.502	38.4
RSFG	200121222	A	76	6	0.075	0.006	292	186	0.058	8.8	2–6	33	-41.885	172.833	6.9
RSFG	200122018	A	-86	3	0.113	0.006	104	-67	0.268	45.2	1–3	12	-41.976	173.284	31.9
RSFG	200132812	A	61	10	0.044	0.003	199	194	0.287	49.5	2–6	5	-42.271	172.743	42.6
RSFG	200133714	A	60	2	0.056	0.000	179	200	0.236	38.8	2–6	33	-42.429	172.924	57.9
TOPS	200129717	A	-14	3	0.269	0.003	130	93	0.285	49.0	2–6	8	-42.047	173.237	41.9
TOPS	200130315	A	47	8	0.081	0.0031	168	173	0.279	47.6	2–6	10	-42.098	172.935	33.6
TOPS	200130602	A	55	8	0.088	0.003	171	186	0.281	48.2	1–3	11	-42.157	172.925	39.9
TOPS	200131418	A	46	7	0.056	0.003	192	191	0.239	39.4	2–6	33	-42.353	172.694	62.6
WAG	200119502	A	-48	2	0.094	0.008	155	52	0.283	48.5	1–3	12	-42.459	173.175	47.9
WAG	200120207	A	70	1	0.038	0.000	189	215	0.220	35.7	2–6	33	-42.456	172.850	43.7
WAG	200121303	A	-63	6	0.050	0.003	80	-1	0.283	48.6	2–6	5	-42.032	173.180	20.9
WAG	200121703	A	77	7	0.038	0.000	176	203	0.147	23.0	1–5	11	-42.118	172.935	5.7
WAG	200122405	A	72	3	0.069	0.002	268	138	0.284	48.8	2–5	5	-42.073	172.640	24.1
WAG	200130602	A	64	5	0.031	0.002	183	205	0.173	27.2	2–6	11	-42.158	172.924	10.1
5MI	200204822	A	-52	3	0.019	0.002	175	23	0.147	22.9	None	39	-42.563	173.025	25.4
5MI	200201320	B	-39	5	0.050	0.002	249	66	0.141	22.0	None	33	-42.399	172.768	20.0
5MI	200201423	B	-47	12	0.031	0.008	345	10	0.135	20.9	None	33	-42.171	172.937	18.8
5MI	200202315	B	29	10	0.063	0.020	240	162	0.250	41.4	None	12	-42.434	172.767	21.8
5MI	200205210	B	81	3	0.331	0.002	234	134	0.287	49.4	2–6	12	-42.468	172.746	96.8
5MI	200205700	B	5	12	0.038	0.005	321	42	0.130	20.2	1–6	47	-42.142	172.783	27.6
5MI	200205700	B	-39	9	0.025	0.002	321	20	0.130	20.2	None	47	-42.142	172.783	27.6
ACH	200202701	B	71	7	0.050	0.002	89	107	0.256	42.8	2–6	12	-42.384	173.271	25.7

continued on next page...

Station	Event	Qual	ϕ	$\pm\phi$	δt	$\pm\delta t$	Baz	Pol	Slow	Incid	Filter	Ede	Elat	Elong	Edist
ACH	200204205	B	65	4	0.175	0.005	232	137	0.270	45.7	1–6	5	-42.473	172.812	15.3
ALI00	200119502	B	40	6	0.381	0.003	164	102	0.286	49.3	2–6	12	-42.459	173.175	86.7
ALI00	200121200	B	44	7	0.381	0.003	169	105	0.286	49.3	2–6	12	-42.472	173.083	86.3
ALI00	200122013	B	77	10	0.069	0.034	130	141	0.288	49.6	2–6	5	-41.986	173.319	47.8
ALI00	200122018	B	78	6	0.094	0.003	131	142	0.282	48.3	2–6	12	-41.976	173.283	44.8
ALIN	200121104	B	-1	11	0.031	0.006	252	63	0.271	46.0	2–6	12	-41.726	172.501	33.0
ALIN	200121303	B	72	10	0.331	0.009	149	194	0.288	49.7	2–6	5	-42.032	173.179	49.0
ALIN	200122013	B	71	6	0.125	0.011	136	144	0.288	49.7	2–6	5	-41.986	173.318	52.1
ALIN	200122306	B	13	8	0.094	0.003	215	152	0.289	49.9	2–6	20	-42.020	173.535	49.8
CCH	200110823	B	-51	7	0.069	0.036	219	53	0.287	49.5	2–5	5	-42.289	172.889	41.1
CCH	200111214	B	-9	8	0.150	0.003	177	113	0.261	43.8	1–3	12	-42.225	172.907	27.8
CCH	200114510	B	-66	6	0.175	0.005	90	51	0.286	49.2	2–6	5	-41.999	173.291	33.2
CCH	200114703	B	-34	10	0.031	0.003	297	12	0.286	49.3	2–6	5	-41.865	172.528	33.6
CCH	200114721	B	-33	15	0.031	0.005	296	21	0.286	49.2	2–5	5	-41.187	172.534	32.8
CCH	200115701	B	-80	8	0.031	0.003	314	70	0.287	49.6	2–5	5	-41.720	172.505	44.7
MORB	200204809	B	84	15	0.275	0.017	140	226	0.286	49.3	1–3	9	-41.985	173.380	60.4
MORB	200207915	B	-72	8	0.144	0.003	187	-19	0.243	39.9	2–6	33	-42.183	172.808	68.7
MORB	200210100	B	-28	8	0.219	0.006	184	24	0.259	43.4	2–5	18	-42.306	172.852	81.9
MORB	200212615	B	-73	12	0.100	0.011	190	-41	0.287	49.4	2–4	12	-42.406	172.704	94.4
RSF00	200111214	B	-70	3	0.156	0.002	175	-48	0.281	48.2	2–6	12	-42.255	172.907	41.8
RSF00	200112520	B	90	7	0.063	0.013	182	254	0.287	49.4	2–5	5	-42.226	172.846	38.8
RSFG	200121200	B	54	9	0.056	0.005	167	183	0.285	49.0	2–6	12	-42.472	173.083	64.2
RSFG	200121303	B	-44	15	0.075	0.009	122	78	0.285	49.0	1–3	5	-42.032	173.179	26.3
RSFG	200122122	B	42	6	0.038	0.002	198	174	0.275	46.7	2–6	12	-42.210	172.777	35.3
RSFG	200133307	B	43	13	0.044	0.003	198	178	0.288	49.6	2–6	5	-42.305	172.738	46.3
TOPS	200129021	B	31	10	0.081	0.006	181	155	0.259	43.4	2–4	20	-42.406	172.834	67.1
TOPS	200129808	B	63	8	0.188	0.009	150	187	0.288	49.8	1–5	5	-42.234	173.186	55.4
WAG	200117715	B	-52	12	0.063	0.009	188	62	0.288	49.7	1–3	5	-42.501	172.851	48.6
WAG	200121019	B	67	16	0.038	0.152	209	197	0.262	44.0	2–5	12	-42.288	172.764	28.1
WAG	200122013	B	86	3	0.175	0.000	75	215	0.286	49.3	2–5	5	-41.986	173.318	33.3
WAG	200122018	B	74	6	0.150	0.002	71	120	0.266	44.9	2–6	12	-41.976	173.283	30.9
WAG	200204205	B	60	6	0.175	0.003	192	182	0.288	49.7	2–4	5	-42.473	172.812	46.2
WAG	200207915	B	-71	8	0.281	0.005	218	58	0.122	18.8	1–3	33	-42.183	172.807	16.5
5MI	200206202	B	-24	8	0.063	0.002	212	31	0.271	45.9	2–6	12	-42.060	173.190	32.8

continued on next page...

Station	Event	Qual	ϕ	$\pm\phi$	δt	$\pm\delta t$	Baz	Pol	Slow	Incid	Filter	Ede	Elat	Elong	Edist
ALI00	200122122	B	16	6	0.156	0.002	188	49	0.283	48.8	4-8	12	-42.210	172.777	56.2
CCH	200111205	B	29	6	0.200	0.001	208	145	0.286	49.3	1–6	5	-42.276	172.695	34.4
MORB	200202701	B	2	7	0.231	0.003	162	48	0.287	49.4	3-7	12	-42.384	173.271	95.3
RSF00	200111623	B	79	6	0.200	0.006	147	186	0.287	49.5	2–5	5	-42.189	173.134	41.5
TOPS	200128804	B	21	6	0.188	0.005	173	90	0.259	43.4	2–5	21	-42.565	172.979	85.3
5MI	200204622	Null A	-46	3	0.056	0.011	204	37	0.167	26.3	None	33	-42.543	172.869	25.2
ACH	200205700	Null A	-49	2	0.044	0.008	332	35	0.141	21.9	2–6	47	-42.142	172.784	30.9
ALI00	200115811	Null A	-37	5	0.838	0.100	197	67	0.287	49.5	2–6	12	-42.633	172.503	107.1
ALI00	200117715	Null A	-39	6	0.663	0.009	181	76	0.289	49.9	2–6	5	-42.501	172.852	87.8
ALI00	200121104	Null A	43	22	0.019	0.044	263	68	0.269	45.5	2–6	12	-41.726	172.502	31.5
ALI00	200121703	Null A	-53	4	0.275	0.009	174	47	0.283	48.7	2–6	11	-42.118	172.935	45.5
ALI00	200122405	Null A	-36	1	0.656	0.008	206	58	0.287	49.6	1–3	5	-42.073	172.639	44.8
ALIN	200115701	Null A	-67	13	0.031	0.008	268	90	0.286	49.2	2–6	5	-41.720	172.505	31.0
ALIN	200121222	Null A	86	9	0.081	0.016	188	161	0.170	26.8	3-5	33	-41.885	172.833	26.1
ALIN	200121703	Null A	-51	5	0.069	0.011	175	52	0.284	48.9	2–6	10	-42.118	172.935	51.9
CCH	200113706	Null A	74	2	0.463	0.005	188	174	0.288	49.8	2–4	5	-42.511	172.794	57.0
CCH	200115805	Null A	-71	4	0.931	0.208	204	33	0.285	49.1	2–6	12	-42.597	172.535	72.2
CCH	200115811	Null A	-75	3	0.813	0.034	204	0	0.286	49.2	2–6	12	-42.633	172.503	77.0
MORB	200202315	Null A	79	7	0.319	0.008	187	130	0.287	49.4	1–3	12	-42.434	172.767	96.7
MORB	200208218	Null A	15	4	0.269	0.006	142	84	0.288	49.7	2–5	5	-41.948	173.304	53.3
RSF00	200110823	Null A	82	8	0.113	0.005	207	237	0.288	49.7	2–8	5	-42.289	172.865	51.6
RSF00	200113211	Null A	-78	3	0.069	0.002	172	86	0.289	49.9	2–8	5	-42.478	172.976	67.5
RSFG	200114608	Null A	-26	4	0.275	0.008	157	76	0.224	36.4	2–6	33	-42.615	173.321	85.5
RSFG	200114703	Null A	-74	16	0.931	0.022	278	101	0.286	49.2	2–6	5	-41.865	172.528	32.0
RSFG	200114721	Null A	-70	9	0.950	0.013	277	104	0.286	49.2	2–6	5	-41.187	172.534	31.4
RSFG	200132507	Null A	55	11	0.044	0.006	205	170	0.281	48.2	3-8	12	-42.250	172.695	41.8
RSFG	200133713	Null A	-45	6	0.956	0.059	163	35	0.224	36.4	1–3	33	-42.619	173.203	82.6
WAG	200115701	Null A	-44	2	0.775	0.003	317	60	0.288	49.7	2–6	5	-41.720	172.505	52.2
WAG	200121104	Null A	81	2	0.013	0.002	315	258	0.283	48.6	2–10	12	-41.726	172.502	50.4
WAG	200121222	Null A	-41	5	0.175	0.002	338	88	0.150	23.4	2–6	33	-41.885	172.833	21.7
WAG	200203200	Null A	90	5	0.269	0.002	144	214	0.143	22.2	2–5	14	-42.259	173.310	53.6
WAG	200204809	Null A	67	5	0.919	0.005	76	140	0.283	48.7	3-8	9	-41.985	173.380	38.3
WAG	200204822	Null A	15	6	0.463	0.011	172	82	0.213	34.3	1–3	39	-42.563	173.025	55.6
WAG	200206202	Null A	18	5	0.150	0.005	87	133	0.225	36.7	2–6	12	-42.060	173.139	17.2

continued on next page...

Station	Event	Qual	ϕ	$\pm\phi$	δt	$\pm\delta t$	Baz	Pol	Slow	Incid	Filter	Ede	Elat	Elong	Edist
WAG	200208218	Null A	-69	24	0.163	0.202	67	-27	0.286	49.3	2–6	5	-41.949	173.304	33.6
5MI	200202917	Null B	-34	8	0.856	0.856	145	151	0.117	18.1	None	50	-42.524	173.175	25.7
ALI00	200117811	Null B	-2	9	0.869	0.008	179	16	0.288	49.8	2–6	5	-42.263	172.895	61.4
ALI00	200119400	Null B	42	30	0.244	0.166	156	209	0.224	36.4	2–6	33	-42.371	173.271	80.3
ALIN	200122405	Null B	-14	3.5	0.306	0.011	203	90	0.288	49.7	2–5	5	-42.073	172.639	50.7
CCH	200112520	Null B	-69	1	0.488	0.006	188	18	0.284	48.9	1–3	5	-42.226	172.846	25.1
CCH	200114316	Null B	-3	4	0.463	0.005	169	63	0.284	48.8	1–5	12	-42.499	173.015	56.2
CCH	200114500	Null B	-12	15	0.031	0.005	183	27	0.284	48.9	1–5	12	-42.471	172.857	52.1
MORB	200205210	Null B	-73	5	0.275	0.005	188	-44	0.287	49.5	2–6	12	-42.468	172.746	10.1
MORB	200206220	Null B	-47	6	0.969	0.027	160	-35	0.288	49.9	3-8	5	-42.120	173.182	65.2
MORB	200210916	Null B	-69	24	0.731	0.131	175	96	0.222	36.1	2–5	33	-42.522	173.019	106.2
RSF00	200111205	Null B	82	5	0.138	0.003	197	239	0.287	49.6	2–6	5	-42.276	172.696	46.4
RSF00	200112505	Null B	11	2	0.138	0.008	172	109	0.222	36.1	2–6	32	-42.631	173.009	84.8
RSFG	200122013	Null B	-90	2	0.275	0.008	104	-71	0.286	49.3	1–3	5	-41.986	173.318	34.9
RSFG	200134809	Null B	11	3	0.119	0.017	152	92	0.285	49.1	1–3	12	-42.449	173.295	68.0
WAG	200115805	Null B	-67	14	0.094	0.028	209	36	0.285	49.0	1–3	12	-42.597	172.535	67.3
WAG	200115811	Null B	86	20	0.031	0.017	209	206	0.285	49.1	1–3	12	-42.633	172.503	72.1
WAG	200119407	Null B	-45	26	0.100	0.098	140	25	0.220	35.7	2–5	33	-42.371	173.271	43.9
WAG	200121200	Null B	-45	3	0.100	0.005	164	60	0.283	48.5	2–6	12	-42.472	173.083	46.7
WAG	200122306	Null B	17	28	0.875	0.248	279	188	0.289	49.9	2–5	20	-42.020	173.536	33.1

Table B.1: **List of splitting measurements for the Marlborough deployment of broadband seismometers**

Table B.2: Summary of splitting measurements for the short-period array ALI

Station	Event	Qual	ϕ	$\pm\phi$	δt	$\pm\delta t$	Baz	Pol	Slow	Incid	Filter	Ede	Elat	Elong	Edist
E1	200108421	A	43	5	0.063	0.006	171	69	0.222	36.1	1–3	33	-42.542	173.061	93.5
E2	200129717	A	79	8	0.125	0.008	142	135	0.285	49.1	0.5–3	8	-42.047	173.237	47.2
E5	200129717	A	-62	7	0.094	0.009	144	-3	0.285	49.1	0.5–3	8	-42.047	173.237	46.3
S3	200108323	A	41	1	0.063	0.000	170	189	0.222	36.1	1–5	28	-42.580	172.074	95.9
S4	200108323	A	55	3	0.056	0.002	170	213	0.222	36.1	1–5	28	-42.575	172.074	95.5
S4	200108421	A	55	5	0.063	0.008	171	211	0.222	36.1	0.5–3	33	-42.542	173.061	91.6
S4	200130602	A	38	4	0.094	0.005	175	192	0.284	48.7	0.5–5	11	-42.158	172.925	47.8
S5	200108122	A	53	6	0.138	0.005	134	181	0.287	49.6	1–3	5	-42.019	173.272	45.7
S5	200108323	A	43	2	0.063	0.003	170	203	0.222	36.1	0.5–3	28	-42.575	172.074	94.9
E1	200108122	B	30	6	0.088	0.006	137	148	0.287	49.6	1–5	5	-42.019	173.272	47.1
E2	200035817	B	27	5	0.150	0.003	159	179	0.222	36.1	0.2–2	33	-42.502	173.295	0.9
E4	200035817	B	32	11	0.065	0.011	160	188	0.222	36.1	0.5–3	33	-42.502	173.295	0.9
E5	200126202	B	-37	8	0.075	0.009	152	22	0.284	48.8	0.5–3	10	-42.083	173.173	46.8
E5	200132003	B	9	6	0.125	0.003	210	142	0.279	47.6	0.5–5	12	-41.989	172.684	36.1
S1	200035817	B	-49	5	0.075	0.006	158	25	0.222	36.1	0.5–4	33	-42.502	173.295	0.9
S3	200100101	B	87	5	0.313	0.002	193	132	0.289	49.9	1.5 –5	5	-42.287	172.271	0.6
S3	200104919	B	44	4	0.238	0.003	191	189	0.222	36.1	0.2–2	33	-42.611	172.647	100.3
S3	200108122	B	53	6	0.131	0.006	135	180	0.287	49.6	0.5–3	5	-42.019	173.272	46.4
S3	200111623	B	-67	6	0.138	0.005	157	53	0.288	49.8	0.5–3	5	-42.189	173.134	55.9
S3	200129717	B	75	12	0.094	0.016	140	136	0.285	49.1	0.5–3	8	-42.047	173.237	46.6
S4	200035817	B	-67	12	0.038	0.005	159	74	0.222	36.1	0.5–4	33	-42.502	173.295	0.9
S4	200104919	B	39	3	0.125	0.005	191	202	0.222	36.1	0.5–3	33	-42.611	172.647	99.9
S5	200111623	B	-4	8	0.206	0.008	157	36	0.288	49.8	1–3	5	-42.189	173.134	54.9
E3	200111623	B(cs)	46	6	0.325	0.008	159	153	0.288	49.8	1–4	5	-42.189	173.134	56.7
E5	200100101	B(cs)	50	4	0.325	0.003	194	83	0.289	49.9	1.5 –4	5	-42.287	172.271	0.6
S1	200132003	B(cs)	-88	6	0.194	0.002	207	-38	0.279	47.6	0.5–5	12	-41.989	172.684	34.5
S2	200129717	B(cs)	78	6	0.281	0.005	140	202	0.285	49.1	0.5–3	8	-42.047	173.237	47.0
S2	200132003	B(cs)	-27	6	0.156	0.003	208	92	0.279	47.6	0.5–5	12	-41.989	172.684	34.1
S3	200130602	B(cs)	56	4	0.131	0.002	175	85	0.284	48.7	0.5–5	11	-42.158	172.925	48.3
S4	200108122	B(cs)	59	6	0.356	0.008	134	119	0.287	49.6	1–3	5	-42.019	173.272	46.1
S4	200111623	B(cs)	13	6	0.206	0.005	157	66	0.288	49.8	1–4	5	-42.189	173.134	55.5

continued on next page...

Station	Event	Qual	ϕ	$\pm\phi$	δt	$\pm\delta t$	Baz	Pol	Slow	Incid	Filter	Ede	Elat	Elong	Edist
S4	200126202	B(cs)	27	5	0.256	0.003	148	82	0.284	48.8	1–3	10	-42.083	173.173	46.4
S4	200126209	B(cs)	59	12	0.075	0.008	173	201	0.222	36.1	0.5–3	33	-42.386	173.003	79.6
S4	200129717	B(cs)	32	9	0.250	0.006	139	75	0.285	49.1	0.5–3	8	-42.047	173.237	46.3
E1	200108323	Null A	58	2	0.131	0.009	171	67	0.222	36.1	0.5–3	28	-42.575	172.074	97.3
E2	200100101	Null A	52	5	0.338	0.005	193	76	0.289	49.9	0.5–5	5	-42.287	172.271	0.7
E2	200104919	Null A	-30	5	0.463	0.066	191	43	0.222	36.1	1–3	33	-42.611	172.647	102.1
E4	200100101	Null A	31	2	0.900	0.019	194	38	0.289	49.9	1.5 –5	5	-42.287	172.271	0.6
E4	200108421	Null A	19	4	0.438	0.091	172	36	0.222	36.1	0.5–3	33	-42.542	173.061	93.2
E4	200111623	Null A	13	9	0.200	0.008	160	48	0.288	49.8	0.5–3	5	-42.189	173.134	56.5
E4	200126202	Null A	11	7	0.644	0.006	151	45	0.284	48.8	1–3	10	-42.083	173.173	47.1
E4	200126209	Null A	24	3	0.075	0.019	174	198	0.222	36.1	0.5–3	33	-42.386	173.003	81.3
E4	200130602	Null A	89	4	0.338	0.045	177	188	0.284	48.7	0.5–5	113	-42.158	172.925	49.7
E5	200104919	Null A	35	5	0.713	0.061	192	58	0.222	36.1	1–3	33	-42.611	172.647	102.3
E5	200108323	Null A	-41	3	0.148	0.020	172	40	0.222	36.1	1–3	28	-42.575	172.074	97.0
E5	200111623	Null A	-14	20	0.200	0.016	160	140	0.288	49.8	0.5–3	5	-42.189	173.134	56.4
S1	200100101	Null A	39	4	0.338	0.006	192	197	0.289	49.8	0.5–4	5	-42.287	172.271	0.6
S1	200108323	Null A	52	2	0.281	0.006	170	63	0.222	36.1	0.5–3	28	-42.575	172.074	97.0
S2	200100101	Null A	76	14	0.750	0.113	193	242	0.289	49.9	0.5–5	5	-42.287	172.271	0.6
S2	200104919	Null A	-12	6	0.231	0.009	191	97	0.222	36.1	0.2–2	33	-42.611	172.647	100.9
S2	200108323	Null A	-39	22	0.050	0.022	170	46	0.222	36.1	0.5–3	28	-42.575	172.074	96.5
S2	200126209	Null A	9	5	0.169	0.013	173	111	0.222	36.1	0.5–3	33	-42.386	173.003	80.6
S3	200108421	Null A	57	5	0.069	0.008	171	219	0.222	36.1	1–3	33	-42.542	173.061	92.0
S4	200100101	Null A	79	4	0.175	0.006	193	239	0.289	49.9	1–3	5	-42.287	172.271	63.6
S5	200100101	Null A	46	4	0.119	0.006	193	213	0.289	49.9	1.5 –5	5	-42.287	172.271	63.1
S5	200104919	Null A	-47	10.01	0.688	0.008	191	46	0.222	36.1	0.5–3	33	-42.611	172.647	99.4
S5	200108421	Null A	38	3	0.062	0.008	170	206	0.222	36.1	0.5–3	33	-42.542	173.061	91.1
E1	200035817	Null B	-18	5	0.188	0.041	159	82	0.222	36.1	0.5–4	33	-42.502	173.295	0.9
E1	200100101	Null B	-9	10	0.031	0.009	193	60	0.289	49.9	0.5–4	5	-42.287	172.271	0.6
E2	200108323	Null B	30	11	0.056	0.016	171	43	0.222	36.1	0.5–3	28	-42.575	172.074	97.3
E2	200108421	Null B	31	2	0.144	0.003	171	196	0.222	36.1	1–3	33	-42.542	173.061	93.4
E2	200111623	Null B	-81	4	0.856	0.020	159	22	0.288	49.8	0.5–3	5	-42.189	173.134	56.9
E2	200126209	Null B	-44	3	0.406	0.006	173	32	0.222	36.1	0.5–3	33	-42.386	173.003	81.4
E3	200035817	Null B	-37	5	0.206	0.011	159	68	0.222	36.1	0.5–3	33	-42.502	173.295	0.9
E3	200108323	Null B	-41	3	0.631	0.017	171	40	0.222	36.1	0.2–2	28	-42.575	172.074	97.2

continued on next page...

Station	Event	Qual	ϕ	$\pm\phi$	δt	$\pm\delta t$	Baz	Pol	Slow	Incid	Filter	Ede	Elat	Elong	Edist
E3	200108421	Null B	40	4	0.325	0.011	171	199	0.222	36.1	1–3	33	-42.542	173.061	93.3
E4	200108323	Null B	-60	3	0.188	0.013	171	39	0.222	36.1	0.5–3	28	-42.575	172.074	97.1
E4	200129717	Null B	-79	2	0.194	0.006	143	2	0.285	49.1	0.5–3	8	-42.047	173.237	46.6
E4	200132003	Null B	-82	4	0.194	0.008	210	20	0.279	47.6	0.5–5	12	-41.989	172.684	35.8
E5	200035817	Null B	53	6	0.113	0.033	160	61	0.222	36.1	0.5–3	33	-42.502	173.295	0.9
E5	200108122	Null B	-57	4	0.306	0.011	138	-13	0.287	49.6	1–3	5	-42.019	173.272	45.7
E5	200108421	Null B	-32	17	0.088	0.028	172	45	0.222	36.1	0.5–3	33	-42.542	173.061	93.2
E5	200126209	Null B	-34	1	0.306	0.022	174	70	0.222	36.1	0.5–4	33	-42.386	173.003	81.2
E5	200130602	Null B	-54	2	0.894	0.011	178	42	0.284	48.7	0.5–5	11	-42.158	172.925	49.6
S1	200104919	Null B	-51	5	0.119	0.008	191	27	0.222	36.1	0.5–3	33	-42.611	172.647	101.4
S2	200035817	Null B	-40	23	0.031	0.044	158	35	0.222	36.1	0.5–3	33	-42.502	173.295	0.9
S2	200108421	Null B	-35	3	0.594	0.009	171	49	0.222	36.1	0.5–3	33	-42.542	173.061	92.6
S2	200130602	Null B	-40	2	0.975	0.008	175	61	0.284	48.7	0.5–5	11	-42.158	172.925	48.8
S3	200126209	Null B	-60	4	0.219	0.006	172	48	0.222	36.1	0.5–3	33	-42.386	173.003	80.0
S5	200035817	Null B	-62	3	0.069	0.006	158	42	0.222	36.1	0.5–4	33	-42.502	173.295	0.9

Table B.2: **List of splitting measurements for the short period seismometer array ALI.**

Table B.3: Summary of Splitting Measurements for the GNS deployment

Station	Event	Qual	ϕ	$\pm\phi$	δt	$\pm\delta t$	Baz	Pol	Slow	Incid	Filter	Ede	Elat	Elong	Edist
GOHM	199334823	A	-23	3	0.068	0.000	200	23	0.285	49.1	N/A	9	-42.929	173.065	55.7
GOHM	199335216	A	40	8	0.075	0.038	201	97	0.285	48.9	0.5–5	11	-42.931	173.051	56.3
ISIM	199329718	A	-36	7	0.065	0.004	311	15	0.071	10.9	0.5–5	42	-41.794	173.597	11.8
ISIM	199335707	A	61	8	0.165	0.004	28	120	0.246	40.6	0.5–5	15	-41.665	173.845	25.0
ISOM	199405322	A	-82	17	0.045	0.009	70	-31	0.211	33.9	0.5–5	28	-42.597	173.361	32.3
LYLM	199331204	A	38	5	0.090	0.006	276	75	0.284	48.9	0.5–3	8	-42.804	172.811	40.1
LYLM	199334823	A	-86	8	0.085	0.006	244	-51	0.260	43.6	N/A	9	-42.929	173.065	21.2
MAPM	199332522	A	77	4	0.090	0.004	99	187	0.282	48.3	0.5–5	8	-41.618	174.298	29.0
MAPM	199335707	A	-54	3	0.143	0.002	223	65	0.193	30.6	0.5–5	15	-41.665	173.845	13.3
WAIM	199329718	A	-22	2	0.040	0.003	124	137	0.078	11.9	1.0-5	42	-41.794	173.597	13.0
WAIM	199404708	A	80	6	0.038	0.000	207	120	0.285	49.0	0.5–5	8	-42.066	173.241	41.9
WROM	199334415	A	89	13	0.130	0.010	8	218	0.234	38.4	1.0-3	31	-41.090	175.478	52.0
CASM	199404708	B	69	2	0.098	0.004	240	171	0.267	45.1	0.5–6	8	-42.066	173.241	19.1
CONM	199330723	B	77	5	0.230	0.005	337	119	0.236	38.7	0.5–5	13	-42.444	173.275	21.3
GOHM	199330723	B	-49	2	0.470	0.004	308	104	0.087	13.3	0.5–3	13	-42.444	173.275	2.6
GOHM	199334819	B	-11	4	0.080	0.003	201	50	0.285	49.0	N/A	10	-42.931	173.050	56.3
GOHM	199336501	B	55	13	0.068	0.004	203	111	0.283	48.6	0.5–5	14	-42.929	173.027	56.8
GOHM	199400703	B	13	9	0.030	0.008	145	123	0.194	31.0	0.5–5	28	-42.657	173.492	27.1
GOHM	199404708	B	21	3	0.120	0.000	354	88	0.285	49.1	0.5–6	8	-42.066	173.241	43.8
ISIM	199331101	B	57	8	0.083	0.008	221	204	0.227	36.9	0.5–3	32	-42.173	173.342	45.5
ISIM	199334422	B	78	7	0.083	0.047	29	200	0.258	43.0	0.5–3	15	-41.609	173.894	32.4
ISIM	199404708	B	62	3	0.098	0.006	239	170	0.285	49.1	0.5–5	8	-42.066	173.241	44.5
ISOM	199402117	B	80	4	0.195	0.004	334	234	0.288	49.8	0.5–4	5	-42.228	172.686	58.0
ISOM	199405906	B	52	5	0.248	0.006	330	92	0.288	49.8	0.5–5	5	-42.243	172.634	58.5
JOPM	199330723	B	-66	5	0.090	0.005	87	-29	0.269	45.4	N/A	13	-42.444	173.275	33.9
KEKM	199331101	B	50	5	0.330	0.006	247	80	0.238	39.2	0.5–5	32	-42.173	173.342	57.5
KENM	199332602	B	-40	10	0.060	0.004	127	79	0.256	42.7	2.0-6	21	-41.370	174.561	44.0
LYLM	199330723	B	-10	6	0.105	0.006	358	41	0.281	48.1	0.5–4	13	-42.444	173.275	44.7
LYLM	199334819	B	-4	11	0.085	0.013	245	122	0.258	43.2	0.1–5	10	-42.931	173.050	22.4
LYLM	199335216	B	-7	2	0.203	0.004	245	63	0.254	42.4	0.5–5	11	-42.931	173.051	22.2
MOLM	199330723	B	-21	2	0.150	0.006	178	83	0.276	47.1	0.5–5	13	-42.444	173.275	39.6

continued on next page...

Station	Event	Qual	ϕ	$\pm\phi$	δt	$\pm\delta t$	Baz	Pol	Slow	Incid	Filter	Ede	Elat	Elong	Edist
NMCM	199405906	B	72	8	0.075	0.006	235	208	0.285	49.0	0.5–5	5	-42.243	172.634	27.5
PUHM	199330723	B	72	7	0.110	0.011	246	137	0.276	47.1	0.5–4	13	-42.444	173.275	39.4
PUHM	199331101	B	39	6	0.203	0.006	295	98	0.201	32.3	1.0-3	32	-42.173	173.342	33.8
PUHM	199400703	B	-71	6	0.143	0.004	205	-44	0.231	37.7	0.5–5	28	-42.657	173.492	43.5
PUHM	199404209	B	27	11	0.045	0.005	193	169	0.226	36.7	1.0-5	14	-42.485	173.655	21.0
PUHM	199404913	B	22	16	0.075	0.014	197	169	0.221	35.9	0.5–5	18	-42.474	173.645	20.0
RIMM	199334415	B	66	5	0.195	0.007	59	184	0.194	31.0	0.5–3	31	-41.090	175.478	31.2
SRWM	199330723	B	-36	4	0.130	0.011	151	35	0.284	48.9	0.5–3	13	-42.444	173.275	63.4
CASM	199330723	NULL A	32	4	0.525	0.009	195	54	0.283	48.6	N/A	13	-42.444	173.275	53.3
CASM	199404913	NULL A	-77	10	0.170	0.008	163	45	0.279	47.7	0.5–5	18	-42.474	173.645	57.4
CONM	199334819	NULL A	79	3	0.113	0.032	218	173	0.283	48.6	0.5–6	10	-42.931	173.050	43.5
CONM	199334823	NULL A	-83	5	0.128	0.283	217	16	0.284	48.7	N/A	9	-42.923	173.065	42.6
CONM	199335216	NULL A	-85	10	0.128	0.071	218	12	0.283	48.6	0.5–5	11	-42.931	173.051	43.4
CONM	199336501	NULL A	-86	6	0.128	0.036	220	10	0.279	47.7	0.5–3	14	-42.929	173.027	44.5
ISOM	199334819	NULL A	74	20	0.040	0.051	170	217	0.268	45.3	N/A	10	-42.931	173.050	26.2
ISOM	199334823	NULL A	50	9	0.070	0.013	167	204	0.272	46.2	N/A	9	-42.929	173.065	26.3
JOPM	199331204	NULL A	-36	3	0.143	0.004	187	-25	0.284	48.8	0.5–5	8	-42.804	172.811	38.2
LYLM	199404209	NULL A	16	7	0.065	0.013	362	36	0.281	48.2	0.5–3	14	-42.485	173.655	49.8
LYLM	199404913	NULL A	-16	16	0.035	0.013	34	31	0.272	46.1	0.5–3	18	-42.474	173.645	50.2
MAPM	199333300	NULL A	-37	6	0.090	0.015	142	70	0.243	40.1	0.5–5	16	-41.756	174.138	25.1
RIMM	199401521	NULL A	75	4	0.585	0.019	212	185	0.240	39.5	0.5–3	31	-41.667	174.792	57.0
TOTM	199333912	NULL A	79	3	0.695	0.019	223	245	0.286	49.4	0.1–1	8	-41.212	172.518	56.6
TOTM	199401023	NULL A	-81	5	0.285	0.008	223	-51	0.288	49.7	0.5–3	5	-41.197	172.546	53.8
CASM	199331101	NULL B	30	4	0.210	0.008	201	49	0.161	25.3	0.5–5	32	-42.173	173.342	22.9
CLAM	199404708	NULL B	36	3	0.950	0.011	271	132	0.286	49.2	2.0-6	8	-42.066	173.241	49.7
CONM	199331101	NULL B	-52	8	0.165	0.019	357	23	0.232	37.9	1.0-3	32	-42.173	173.342	49.9
CONM	199404708	NULL B	57	3	0.158	0.011	350	57	0.287	49.5	0.5–6	8	-42.066	173.241	62.6
CONM	199405322	NULL B	-38	12	0.090	0.043	336	37	0.030	4.6	0.5–5	28	-42.597	173.361	2.9
FABM	199335707	NULL B	-3	4	0.218	0.024	129	78	0.253	42.1	0.5–5	15	-41.665	173.845	28.7
GOHM	199331101	NULL B	31	4	0.870	0.008	6	101	0.196	31.3	0.5–5	32	-42.173	173.342	31.9
GOHM	199405322	NULL B	-9	5	0.158	0.006	162	64	0.137	21.2	N/A	28	-42.597	173.361	16.2
KENM	199332520	NULL B	-11	3	0.150	0.021	166	87	0.286	49.3	0.5–3	8	-41.625	174.296	56.0
LYLM	199336501	NULL B	-7	4	0.203	0.006	247	60	0.241	39.6	0.5–5	14	-42.929	173.027	23.9
LYLM	199405322	NULL B	-73	2	0.525	0.011	11	12	0.199	31.7	0.5–3	28	-42.597	173.361	28.2

continued on next page...

Station	Event	Qual	ϕ	$\pm\phi$	δt	$\pm\delta t$	Baz	Pol	Slow	Incid	Filter	Ede	Elat	Elong	Edist
MOLM	199329718	NULL B	-53	1	0.270	0.009	41	41	0.186	29.5	0.5–5	42	-41.794	173.597	42.9
NMCM	199402117	NULL B	30	4	0.263	0.008	233	95	0.284	48.8	0.5–4	5	-42.228	172.686	23.0
NMCM	199404121	NULL B	16	5	0.353	0.006	233	82	0.284	48.8	0.5–3	5	-42.232	172.675	24.0
PUHM	199405322	NULL B	24	5	0.105	0.004	221	101	0.231	37.8	0.5–5	28	-42.597	173.361	43.8
WROM	199334202	NULL B	-17	6	0.105	0.002	337	28	0.214	34.6	0.5–5	28	-41.278	175.242	33.2

Table B.3: **List of splitting measurements for the GNS deployment.**

APPENDIX C

EVENTS USED FOR STRESS INVERSIONS

This appendix lists the events used in stress inversions and which clusters they were used in.

Date	Date of earthquake given by YYMMDDHH.
Long	Earthquake Longitude.
Lat	Earthquake Latitude.
Strike	Strike of nodal plane.
Dip	Dip of nodal plane.
Rake	Rake of nodal plane.
Depth	Earthquake Depth in kilometers.
Mw	Body wave magnitude of earthquake.
R1	Replication of McGinty's (2000) results from Northern Marlborough.
R2	Replication of McGinty's (2000) results from Southern Marlborough.
R3	Replication of McGinty's (2000) results from Nelson.
T1	Inversion on all the Lake Tennyson data.
T2	Inversion of data on the main fault rupture.
T3	Inversion of data off the main fault rupture.
M4	Cluster 4 of Marlborough data used for stress inversion comparison.
M5	Cluster 5 of Marlborough data used for stress inversion comparison.
M6	Cluster 6 of Marlborough data used for stress inversion comparison.
M7	Cluster 7 of Marlborough data used for stress inversion comparison.
M10	Cluster 10 of Marlborough data used for stress inversion comparison.
M13	Cluster 13 of Marlborough data used for stress inversion comparison.
F4a	Cluster 4a used for focal mechanism comparison.
F8a	Cluster 8a used for focal mechanism comparison.
F10a	Cluster 10a used for focal mechanism comparison.
A1	Cluster 1 used in inversion of all collected focal mechanims.
A2	Cluster 2 used in inversion of all collected focal mechanisms.
A3	Cluster 3 used in inversion of all collected focal mechanisms.
A4	Cluster 4 used in inversion of all collected focal mechanisms.

Table C.1: Summary of the events used in inversions

Date	Long	lat	strike	dip	rake	Depth	Mw	R1	R2	R3	T1	T2	T3	M4	M5	M6	M7	M10	M13	F4	F8	F10	A1	A2	A3	A4
9002140705	172.756	-42.287	53	60	158	4.7	1				✓		✓										✓			
9002131729	172.763	-42.284	158	7.5	68	3.1	2.7				✓		✓										✓			
9002141804	172.744	-42.253	38	90	-128	10.7	3.4				✓	✓											✓			
9002142025	172.763	-42.234	83	90	173	6.9	3				✓	✓											✓			
9002141441	172.756	-42.275	240	67.5	-158	4.2	2.2				✓		✓										✓			
9002140629	172.791	-42.210	30	52.5	113	4.4	2.1				✓		✓										✓			
9002141058	172.667	-42.261	83	52.5	-143	6	2				✓		✓										✓			
9002141119	172.734	-42.225	45	52.5	113	4	1.8				✓		✓										✓			
9002142322	172.679	-42.262	338	75	-38	6.1	1.7				✓		✓										✓			
9002150150	172.753	-42.305	98.0	15.0	53.0	4.20	1.9				✓		✓										✓			
90 2162310	172.717	-42.240	360.0	37.5	45.0	4.10	2.0				✓		✓										✓			
90 21412 4	172.689	-42.270	360.0	67.5	60.0	8.00	1.8				✓		✓										✓			
90 2141335	172.794	-42.209	330.0	52.5	23.0	5.20	1.8				✓		✓										✓			
90 215 145	172.746	-42.307	270.0	7.5	-135.0	4.40	1.6				✓		✓										✓			
90 2121339	172.768	-42.227	68.0	67.5	150.0	5.50	3.2				✓	✓											✓			
90 214 736	172.750	-42.268	203.0	30.0	30.0	5.30	1.6				✓		✓										✓			
90 214 8 0	172.748	-42.312	233.0	82.5	173.0	4.60	0.9				✓		✓										✓			
90 214 833	172.699	-42.275	83.0	52.5	98.0	6.60	1.7				✓		✓										✓			
90 21411 7	172.731	-42.224	60.0	45.0	113.0	4.20	1.5				✓		✓										✓			
90 2141311	172.744	-42.305	53.0	75.0	-150.0	5.00	0.9				✓		✓										✓			
90 215 058	172.706	-42.240	30.0	52.5	128.0	3.20	1.4				✓		✓										✓			
90 215 1 2	172.743	-42.224	150.0	22.5	68.0	4.50	1.0				✓		✓										✓			
90 215 416	172.675	-42.283	60.0	75.0	-173.0	4.00	2.0				✓		✓										✓			
90 215 250	172.704	-42.238	293.0	52.5	-60.0	3.70	2.3				✓		✓										✓			
90 2121336	172.775	-42.225	345.0	75.0	-15.0	5.30	4.3				✓	✓											✓			
90 21215 8	172.773	-42.231	255.0	75.0	165.0	6.20	3.3				✓	✓											✓			
90 2122057	172.732	-42.247	173.0	60.0	60.0	4.80	4.0				✓	✓											✓			
90 212 831	172.738	-42.245	68.0	90.0	-158.0	9.10	3.8				✓	✓											✓			
90 213 431	172.762	-42.229	210.0	30.0	75.0	4.30	3.3				✓	✓											✓			
90 21312 2	172.706	-42.255	338.0	75.0	-30.0	7.00	3.3				✓	✓											✓			
90 214 755	172.751	-42.239	68.0	60.0	-165.0	10.40	3.9				✓	✓											✓			
90 2141810	172.739	-42.244	45.0	75.0	-173.0	8.20	3.6				✓	✓											✓			
90 212 616	172.774	-42.229	75.0	75.0	180.0	4.00	3.1				✓	✓											✓			
90 212 839	172.737	-42.244	330.0	30.0	-8.0	8.80	3.1				✓	✓											✓			
94 2101145	172.780	-41.167	189.4	61.2	-8.0	7.30	1.9							✓												
94 1221340	172.610	-41.213	243.7	74.0	176.0	10.60	2.0							✓												
94 2 91835	172.550	-41.196	12.8	66.0	40.0	12.00	1.9							✓												
9312292235	172.530	-41.204	227.9	50.8	136.0	12.40	2.2							✓												
94 210 052	172.750	-41.246	171.3	58.6	24.0	8.60	2.0							✓												
94 12816 6	172.450	-40.993	274.7	83.3	-152.0	12.60	2.1							✓												

continued on next page...

Date	Long	lat	strike	dip	rake	Depth	Mw	R1	R2	R3	T1	T2	T3	M4	M5	M6	M7	M10	M13	F4	F8	F10	A1	A2	A3	A4
94 1 91131	172.540	-41.199	351.5	53.3	48.0	11.70	2.1							✓												
931211 358	172.610	-41.192	198.0	76.4	-16.0	10.00	2.4							✓												
9312 91627	172.610	-41.203	23.2	66.0	64.0	9.50	1.8							✓												
931210 8 1	172.780	-41.223	36.5	59.6	88.0	9.50	1.8							✓												
9312101029	172.540	-41.205	184.7	68.0	16.0	11.80	2.0							✓												
931220 548	172.530	-41.201	18.0	58.3	40.0	12.50	2.0							✓												
93113010 0	172.740	-41.246	193.0	69.9	-16.0	8.40	2.1							✓												
9311231529	172.690	-41.129	115.2	45.1	-168.0	8.20	2.1							✓												
9311191425	172.400	-40.966	225.0	89.9	-120.0	13.30	2.5							✓												
94 225 614	172.580	-41.179	121.3	83.3	-168.0	10.20	1.9							✓												
94 225 549	173.180	-41.402	193.3	83.3	-104.0	7.20	1.8							✓												
94 1 92211	172.430	-40.952	215.5	59.6	-168.0	12.80	2.6							✓												
94 1122019	172.730	-41.165	224.7	58.6	104.0	8.30	2.5							✓												
931217 9 1	172.540	-41.196	342.0	47.6	120.0	12.40	1.9							✓												
94 112 620	172.550	-41.197	247.9	82.0	-168.0	11.90	1.9							✓												
9312242322	172.600	-41.194	106.3	51.6	-144.0	9.50	2.6							✓												
94 1102314	172.530	-41.200	247.9	82.0	136.0	10.60	3.4			✓				✓												✓
94 2 821 8	172.530	-41.206	252.5	59.6	152.0	10.50	2.6							✓												
94 2 821 2	172.520	-41.206	352.8	45.1	24.0	9.50	3.7							✓												
94 1271347	172.530	-41.207	103.6	43.6	176.0	9.80	2.7							✓												
94 1211236	172.530	-41.198	44.5	53.3	88.0	10.80	2.0							✓												
94 2 11614	172.530	-41.199	157.2	81.9	8.0	11.30	2.4							✓												
94 1 5 537	172.520	-41.208	206.6	61.2	96.0	9.90	3.1							✓												
94 2 9 815	172.520	-41.211	188.5	53.3	40.0	10.10	2.7							✓												
9312231621	172.550	-41.226	238.8	81.9	176.0	10.70	2.6							✓												
94 1301553	172.530	-41.198	337.3	83.3	8.0	10.80	1.9							✓												
94 2 9 147	172.510	-41.209	84.8	66.0	144.0	10.10	2.5							✓												
94 2 821 2	172.530	-41.201	252.2	75.1	152.0	10.40	2.7			✓				✓												✓
93121812 9	172.520	-41.206	187.2	45.1	40.0	11.00	2.8			✓				✓												✓
9312181155	172.530	-41.203	265.0	69.9	144.0	11.50	2.7							✓												
94 13012 3	172.520	-41.204	243.7	74.0	136.0	10.40	2.9			✓				✓												✓
94 112 6 8	172.520	-41.206	188.5	53.3	48.0	10.90	2.8			✓				✓												✓
94 1 81527	172.520	-41.205	63.5	53.3	120.0	10.40	2.8			✓				✓												✓
94 224 911	172.530	-41.201	67.3	68.0	128.0	12.10	2.8			✓				✓												✓
94 112 646	172.530	-41.201	162.0	89.9	-8.0	11.70	2.1							✓												
94 1111730	172.540	-41.200	351.5	53.3	32.0	10.80	2.4							✓												
94 1 8 329	172.540	-41.200	18.0	58.3	48.0	11.00	2.3							✓												
94 219 852	172.520	-41.203	243.7	74.0	136.0	11.10	2.9			✓				✓												✓
94 116 839	172.530	-41.204	342.0	76.4	16.0	10.50	2.5							✓												
94 116 842	172.510	-41.207	347.0	69.9	16.0	9.90	2.3							✓												
94 114 732	172.530	-41.200	243.0	89.9	-176.0	11.30	2.0							✓												
94 112 630	172.540	-41.202	162.0	89.9	-8.0	10.60	2.0							✓												
94 310 149	173.840	-42.030	319.6	43.6	24.0	13.60	2.4								✓						✓					
94 3 4 2 9	173.870	-42.053	188.5	53.3	40.0	13.40	2.0								✓						✓					

continued on next page...

Date	Long	lat	strike	dip	rake	Depth	Mw	R1	R2	R3	T1	T2	T3	M4	M5	M6	M7	M10	M13	F4	F8	F10	A1	A2	A3	A4
94 3112037	174.250	-41.701	256.2	83.3	168.0	9.60	2.3								✓						✓					
94 3 41625	173.940	-41.938	18.0	26.6	128.0	12.40	1.9								✓						✓					
94 2131753	173.850	-41.995	342.0	76.4	-24.0	9.60	2.0								✓						✓					
94 2 71823	173.970	-41.942	162.0	58.3	0.1	14.20	2.4								✓						✓					
94 122 042	174.190	-41.732	328.2	83.3	24.0	12.20	2.3								✓					✓						
94 110 226	174.270	-41.701	139.8	83.3	-24.0	10.70	2.0								✓					✓						
94 2 71823	173.970	-41.942	90.1	58.3	-144.0	14.10	2.0								✓					✓						
94 2151815	174.250	-41.694	279.5	76.6	168.0	11.70	2.0								✓											
94 2101149	173.410	-41.960	324.2	75.1	16.0	12.80	1.6								✓						✓					
94 2131913	174.220	-41.682	228.8	66.0	-152.0	12.80	2.3								✓					✓						
94 2 71623	173.970	-41.941	322.3	51.6	-32.0	14.00	2.0								✓						✓					
94 2 716 2	173.970	-41.938	198.0	47.6	8.0	13.20	1.5								✓						✓					
94 2 71415	173.890	-42.063	301.2	81.9	32.0	14.10	1.5								✓						✓					
94 2 71547	173.970	-41.935	247.9	82.0	-160.0	12.60	1.9								✓						✓					
94 2 71737	173.980	-41.936	351.5	53.3	-40.0	14.10	1.9								✓						✓					
94 2 717 6	173.970	-41.940	90.1	58.3	-128.0	13.70	2.0								✓						✓					
94 119 852	173.930	-41.978	224.7	58.6	80.0	14.40	1.7								✓						✓					
9312 3 059	174.040	-42.064	63.5	76.6	152.0	11.50	2.4								✓						✓					
9312 7 843	174.280	-41.661	274.7	83.3	136.0	11.10	2.2								✓					✓						
9311301454	173.980	-41.931	315.7	74.0	-48.0	14.20	2.0								✓						✓					
9311 71331	173.710	-42.035	135.0	89.9	8.0	12.00	1.8								✓						✓					
931124 157	173.920	-42.061	180.2	75.1	40.0	6.50	2.3								✓						✓					
93112022 7	173.700	-42.036	63.5	53.3	-128.0	12.30	2.2								✓						✓					
9311212147	174.260	-41.657	71.8	75.1	-168.0	11.00	2.5								✓					✓						
9311142031	174.270	-41.803	350.6	61.2	0.1	13.40	1.9								✓						✓					
931114 4 0	173.750	-42.125	215.5	59.6	120.0	10.20	1.8								✓						✓					
9310261659	173.770	-41.744	189.4	61.2	88.0	13.40	1.8								✓					✓						
9310231551	173.730	-42.062	162.0	89.9	40.0	11.50	2.1								✓						✓					
9310231613	173.740	-42.061	167.2	66.0	0.1	12.60	2.4								✓						✓					
94 124 319	174.060	-41.859	80.3	74.0	-168.0	13.90	3.0	✓							✓										✓	
94 123 156	173.840	-42.141	44.5	76.6	160.0	13.20	2.8	✓							✓								✓			
94 1 9 324	174.270	-41.694	130.7	83.3	-8.0	8.60	2.2								✓						✓					
94 1172147	174.280	-41.708	130.7	83.3	0.1	9.00	2.2								✓						✓					
9312192319	173.940	-41.952	243.7	74.0	-168.0	12.90	1.9								✓						✓					
931216 429	173.840	-42.026	297.7	34.9	-8.0	13.20	1.8								✓						✓					
9312271840	174.200	-41.699	332.5	76.6	-24.0	6.00	2.7								✓						✓					
94 112 613	174.270	-41.708	243.0	89.9	176.0	9.20	3.7	✓							✓										✓	
9312271743	174.200	-41.699	347.0	69.9	8.0	5.90	2.6								✓											
94 2102220	173.980	-41.932	76.1	82.0	144.0	12.40	2.1								✓						✓					
94 3 21446	173.940	-41.882	224.3	74.0	144.0	11.10	1.9								✓						✓					
94 123 314	173.820	-41.971	333.4	61.2	0.1	10.40	2.0								✓						✓					
94 224 813	175.060	-41.099	156.8	66.0	64.0	19.30	2.4									✓										
9312 9 6 8	174.820	-41.383	332.5	76.6	-16.0	20.00	2.0									✓										
94 1 4 044	174.500	-41.410	189.0	89.9	96.0	21.90	2.7	✓								✓									✓	

continued on next page...

Date	Long	lat	strike	dip	rake	Depth	Mw	R1	R2	R3	T1	T2	T3	M4	M5	M6	M7	M10	M13	F4	F8	F10	A1	A2	A3	A4
931120 652	174.570	-41.378	157.2	81.9	48.0	21.80	2.9	✓								✓									✓	
931122 2 0	174.560	-41.391	58.7	83.3	168.0	23.50	3.1	✓								✓									✓	
9312181035	175.230	-41.276	49.0	69.9	-136.0	22.50	1.8									✓										
93122420 8	175.200	-41.587	229.2	81.9	104.0	17.70	2.1									✓										
931221 324	175.410	-41.231	342.0	39.6	-32.0	19.70	2.1									✓										
931221 036	175.420	-41.238	59.0	69.9	-88.0	20.80	2.9									✓										
94 2 6 255	175.110	-41.444	220.1	82.0	64.0	21.90	2.4									✓										
94 2 3 832	175.470	-41.452	23.2	66.0	-104.0	17.30	1.8									✓										
931219 632	175.210	-41.576	12.8	66.0	-40.0	17.50	2.9	✓								✓										
9312181457	175.410	-41.237	103.9	66.7	-120.0	19.10	2.4									✓										
93111715 1	175.110	-41.409	138.7	37.2	176.0	23.90	2.1									✓										
931111 811	175.220	-41.222	40.7	68.0	-120.0	21.40	2.1									✓										
9311 7 016	175.590	-41.501	242.3	34.9	-80.0	19.50	2.4									✓										
9312242344	175.210	-41.590	126.0	47.6	-152.0	18.50	2.6									✓										
94 1162131	175.700	-41.189	225.7	34.9	-80.0	19.40	2.2									✓										
9312241944	175.210	-41.577	220.1	82.0	32.0	17.20	2.8	✓								✓									✓	
9312241918	175.210	-41.572	234.0	89.9	88.0	16.80	2.2									✓										
94 3 61532	172.980	-42.280	80.3	74.0	176.0	10.10	2.1										✓					✓				
94 3 32238	173.040	-42.207	351.5	53.3	8.0	9.90	2.0										✓					✓				
94 3101017	173.090	-42.308	76.1	82.0	-136.0	8.30	2.1										✓					✓				
931212 414	173.030	-42.277	143.8	75.1	16.0	10.00	2.0										✓					✓				
9312 9 124	172.740	-42.273	90.1	73.7	168.0	9.80	2.1										✓					✓				
931130 0 2	173.160	-42.231	45.4	61.2	-168.0	8.40	1.9										✓					✓				
9312 6 435	172.730	-42.291	58.7	83.3	160.0	8.70	2.2										✓					✓				
9311292342	173.160	-42.231	315.3	58.6	-24.0	8.60	2.7		✓								✓						✓			
9311 3 727	172.740	-42.254	103.9	66.7	-144.0	5.20	1.9										✓					✓				
9311 21645	172.710	-42.230	189.0	89.9	32.0	6.90	1.7										✓					✓				
9310312251	172.740	-42.206	328.7	68.0	-8.0	9.40	2.4										✓					✓				
9310212140	172.730	-42.213	136.8	45.1	-72.0	8.80	2.4										✓					✓				
9311 4 014	172.700	-42.232	143.8	75.1	-8.0	7.30	2.8		✓								✓						✓			
9310301227	172.740	-42.235	96.1	50.8	-120.0	5.90	2.2										✓									
9310271436	172.700	-42.238	300.8	66.0	-56.0	6.00	2.2										✓					✓				
94 3111259	172.890	-42.300	347.0	69.9	-24.0	12.70	2.0										✓					✓				
94 3 51249	172.880	-42.543	135.0	89.9	-8.0	6.60	1.8										✓					✓				
94 3 11545	172.970	-42.132	148.4	43.6	-72.0	11.90	1.7										✓					✓				
94 1111540	172.880	-42.391	166.8	81.9	8.0	13.40	2.1										✓					✓				
94 118 926	173.120	-42.690	62.6	61.2	128.0	7.70	2.4										✓					✓				
94 1 11818	172.810	-42.189	256.7	68.0	-144.0	9.10	2.9		✓								✓						✓			
94 220 248	172.960	-42.392	332.5	76.6	-24.0	12.30	2.2										✓					✓				
94 13115 0	173.210	-42.239	73.7	51.6	-128.0	9.80	1.8										✓					✓				
931214 835	172.910	-42.368	90.1	89.9	144.0	11.20	2.4										✓					✓				
94 12515 0	172.980	-42.127	282.7	37.2	-144.0	11.30	2.4										✓					✓				
94 1 9 959	172.730	-42.222	148.4	43.6	-72.0	11.70	2.1										✓					✓				
9311241446	172.820	-42.438	243.3	58.6	-144.0	7.80	2.0										✓					✓				

continued on next page...

Date	Long	lat	strike	dip	rake	Depth	Mw	R1	R2	R3	T1	T2	T3	M4	M5	M6	M7	M10	M13	F4	F8	F10	A1	A2	A3	A4
93112411 8	172.830	-42.550	306.0	73.7	-16.0	8.40	1.9										✓					✓				
9311 8 1 9	173.110	-42.044	180.2	75.1	-16.0	8.40	1.9										✓					✓				
9311221333	172.900	-42.376	18.0	58.3	32.0	8.70	2.6										✓					✓				
9311231835	172.820	-42.306	76.1	82.0	-152.0	6.60	2.1										✓					✓				
931124 821	172.700	-42.236	162.0	89.9	8.0	5.40	2.8		✓								✓						✓			
931111 459	172.840	-42.161	296.7	58.6	-104.0	7.90	2.0										✓					✓				
9311111143	172.900	-42.370	333.4	61.2	-24.0	7.20	2.4										✓					✓				
9311 2 650	173.110	-42.096	152.7	58.6	-16.0	8.40	1.9										✓					✓				
9311 11235	173.110	-42.098	269.8	47.6	-168.0	8.00	2.0										✓					✓				
94 113 4 2	172.810	-42.191	269.9	76.4	-160.0	9.50	1.9										✓					✓				
94 3 91153	174.190	-41.661	84.8	66.0	136.0	15.60	1.7											✓		✓						
94 3 91618	173.960	-41.923	64.8	45.1	-152.0	15.30	1.9											✓		✓						
94 3 6 037	173.960	-41.608	332.5	76.6	-24.0	12.90	2.0											✓		✓						
94 1 3 953	173.880	-41.664	162.0	42.8	-56.0	15.00	2.0											✓		✓						
94 1 313 8	173.890	-41.630	171.7	74.0	0.1	16.30	1.9											✓		✓						
931223 858	173.840	-41.690	99.0	89.9	176.0	17.00	2.1											✓		✓						
931223 656	173.840	-41.690	189.0	89.9	0.1	17.20	2.3											✓		✓						
931223 652	173.840	-41.690	116.5	53.3	-168.0	16.50	2.3											✓		✓						
931222 229	173.910	-41.687	26.3	34.9	72.0	15.20	2.1											✓		✓						
931223 721	173.840	-41.692	189.0	89.9	0.1	17.50	2.8	✓										✓							✓	
931219 423	174.320	-41.690	171.7	74.0	40.0	16.00	2.9	✓										✓							✓	
931219 227	174.320	-41.690	153.0	89.9	48.0	16.20	3.0	✓										✓							✓	
9312101521	174.270	-41.809	322.3	51.6	32.0	15.00	2.0											✓		✓						
9312 7 656	174.210	-41.675	54.0	47.6	-168.0	14.20	2.1											✓		✓						
9311291240	174.240	-41.772	238.8	81.9	152.0	15.50	2.1											✓		✓						
9311241718	173.890	-41.606	90.1	73.7	168.0	15.70	2.0											✓		✓						
931117 923	173.890	-41.625	351.5	76.6	-64.0	16.10	2.2											✓		✓						
93111918 3	173.920	-41.690	67.8	83.3	176.0	15.30	2.3											✓		✓						
9311111859	173.890	-41.626	85.2	81.9	176.0	15.50	2.0											✓		✓						
9311152332	173.890	-41.682	179.9	89.9	-8.0	15.40	2.1											✓		✓						
9311 2 1 3	173.900	-41.689	243.0	89.9	176.0	14.10	2.2											✓		✓						
9311 81135	173.900	-41.634	292.1	82.0	-144.0	17.40	1.9											✓		✓						
931112 251	174.100	-41.451	243.7	74.0	72.0	19.50	2.2											✓		✓						
9311 6 0 2	173.950	-41.609	90.5	12.9	96.0	13.90	2.0											✓		✓						
9311 61433	174.110	-41.768	328.7	68.0	40.0	15.20	1.9											✓		✓						
9311 3 527	174.080	-41.571	243.3	58.6	-128.0	13.00	2.1											✓		✓						
9311 4 522	173.760	-41.802	351.5	76.6	8.0	14.30	1.7											✓		✓						
9311 3 723	173.890	-41.688	269.9	63.4	-152.0	14.40	1.8											✓		✓						
9310172130	174.310	-41.672	138.7	37.2	-80.0	13.60	2.6											✓		✓						
94 12323 2	173.890	-41.624	347.0	69.9	-64.0	16.20	2.3											✓		✓						
94 1221450	174.180	-41.718	224.3	74.0	136.0	13.30	1.8											✓		✓						
94 2271558	173.880	-41.615	90.1	73.7	-160.0	16.70	1.9											✓		✓						
94 2231928	173.970	-41.603	63.5	53.3	-152.0	14.30	2.7											✓		✓						
931224 0 9	173.920	-41.691	243.0	89.9	-176.0	15.60	2.1											✓		✓						

continued on next page...

Date	Long	lat	strike	dip	rake	Depth	Mw	R1	R2	R3	T1	T2	T3	M4	M5	M6	M7	M10	M13	F4	F8	F10	A1	A2	A3	A4
931223 722	173.840	-41.684	126.0	89.9	136.0	18.10	2.4											✓								
931230 437	174.320	-41.670	96.1	50.8	-168.0	13.10	2.2											✓		✓						
931229 837	173.890	-41.616	54.0	7.9	112.0	16.10	2.1											✓		✓						
931229 130	173.830	-41.688	171.7	74.0	-24.0	16.30	2.1											✓		✓						
9312232051	173.830	-41.686	189.0	89.9	-8.0	14.60	2.1											✓		✓						
9312241619	174.020	-41.545	67.8	83.3	-128.0	14.90	2.5											✓		✓						
94 218 616	174.570	-41.529	131.0	69.9	-40.0	17.40	2.2											✓		✓						
94 1 222 5	173.970	-41.969	152.3	74.0	72.0	18.50	1.9											✓		✓						
94 1242329	174.220	-41.996	162.0	42.8	-64.0	20.40	2.1											✓		✓						
9311301250	173.510	-41.171	234.0	26.6	96.0	14.00	2.2											✓		✓						
94 2111249	173.560	-42.416	45.4	61.2	120.0	12.40	1.8												✓			✓				
931027 713	173.600	-42.205	328.7	68.0	-72.0	14.90	2.2												✓		✓					
94 223 340	173.750	-42.299	292.5	20.3	40.0	11.40	2.0												✓		✓					
94 2241556	173.750	-42.302	228.8	66.0	88.0	11.30	2.9												✓		✓					
931229 917	173.720	-42.371	23.2	66.0	8.0	10.20	1.7												✓		✓					
94 2262014	173.350	-42.580	108.5	59.6	144.0	9.20	2.8		✓										✓				✓			
94 2111627	173.560	-42.415	71.5	59.6	144.0	12.40	1.7												✓			✓				
94 212 120	173.550	-42.417	193.0	69.9	48.0	12.20	2.2												✓			✓				
94 2 91912	173.550	-42.413	188.5	76.6	56.0	12.60	2.2												✓			✓				
9311 32345	173.290	-42.435	117.0	89.9	56.0	11.50	2.1												✓			✓				
9311 32344	173.290	-42.434	239.2	66.0	-160.0	11.10	2.3												✓			✓				
9311 32337	173.280	-42.434	44.5	53.3	-144.0	11.90	2.4												✓							
9311 32336	173.280	-42.435	207.0	89.9	-120.0	11.10	2.1												✓							
9311 32335	173.280	-42.437	333.4	61.2	40.0	11.80	3.0		✓										✓				✓			
9311 4 4 2	173.280	-42.437	23.2	66.0	-16.0	11.30	2.9		✓										✓				✓			
9311 4 133	173.290	-42.437	148.4	43.6	-8.0	11.30	2.1												✓			✓				
9311 611 2	173.280	-42.433	296.7	58.6	-48.0	10.90	1.7												✓			✓				
9311 32343	173.280	-42.436	252.0	89.9	-144.0	11.70	2.3												✓			✓				
9310252347	173.640	-42.504	198.0	55.5	120.0	11.70	2.1												✓			✓				
9311 4 138	173.290	-42.437	256.2	83.3	-152.0	11.00	2.3												✓			✓				
9311 32359	173.270	-42.438	117.4	61.2	-24.0	11.40	2.2												✓			✓				
9310261157	173.630	-42.504	64.8	45.1	168.0	11.90	2.2												✓			✓				
931026 120	173.640	-42.504	198.0	55.5	120.0	11.90	2.2												✓			✓				
94 1181649	173.320	-42.584	90.1	58.3	-168.0	8.40	2.7												✓							
94 114 8 5	173.280	-42.434	260.5	76.6	-152.0	11.50	2.0												✓			✓				
94 1 81827	173.580	-42.436	66.7	37.2	-144.0	17.10	2.1												✓		✓					
94 221 945	173.150	-42.333	126.0	47.6	-24.0	11.50	2.6												✓			✓				
94 1 41431	173.260	-42.340	299.9	50.8	0.1	9.60	2.0												✓			✓				
9311 5 211	173.290	-42.435	148.4	43.6	-8.0	11.40	2.0												✓			✓				
94 2181336	173.560	-42.410	49.0	69.9	120.0	12.10	2.1												✓							
94 2181412	173.560	-42.411	4.1	82.0	48.0	12.70	2.4												✓			✓				
94 2211122	173.570	-42.414	153.0	89.9	24.0	12.90	2.0												✓			✓				
94 227 313	173.520	-42.557	260.5	53.3	104.0	8.60	1.9												✓			✓				
94 2181336	173.560	-42.411	274.7	83.3	176.0	13.20	4.1	✓											✓				✓			

continued on next page...

Date	Long	lat	strike	dip	rake	Depth	Mw	R1	R2	R3	T1	T2	T3	M4	M5	M6	M7	M10	M13	F4	F8	F10	A1	A2	A3	A4
94 212 252	173.560	-42.415	220.1	66.7	96.0	12.40	2.2												✓			✓				
931114 0 6	174.313	-41.542	270.0	52.5	-157.5	6.11	2.7	✓																	✓	
9311 11349	173.865	-42.250	270.0	67.5	-172.5	7.28	2.8	✓															✓			
94 3 31152	173.863	-40.949	315.0	75.0	-45.0	7.32	2.9	✓																	✓	
9312161053	173.983	-42.139	30.0	67.5	105.0	7.62	4.0	✓															✓			
9312 11024	174.000	-42.160	360.0	67.5	82.5	8.94	3.9	✓															✓			
9312 32220	174.008	-42.161	172.5	75.0	-22.5	9.73	2.9	✓															✓			
9311212 01	174.285	-41.636	255.0	60.0	-172.5	10.67	4.5	✓																	✓	
9311212222	174.287	-41.634	270.0	67.5	165.0	11.29	3.4	✓																	✓	
940116 244	175.475	-41.616	150.0	7.5	30.0	11.75	3.2	✓																	✓	
9311201812	174.148	-42.134	277.5	30.0	142.5	12.19	3.0	✓																	✓	
94 1 9 511	174.441	-41.596	255.0	52.5	142.5	12.89	3.1	✓																	✓	
94 219 4 7	175.692	-41.316	52.5	90.0	90.0	14.73	3.7	✓																	✓	
94 314 936	175.865	-41.405	97.5	60.0	-142.5	15.92	3.1	✓																	✓	
9312102226	173.881	-41.626	330.0	60.0	-22.5	16.02	3.1	✓																	✓	
931129 016	174.116	-41.765	232.5	67.5	172.5	16.10	3.4	✓																	✓	
931223 719	173.833	-41.681	330.0	45.0	-37.5	16.12	3.2	✓																	✓	
931121 627	174.380	-41.420	262.5	67.5	-30.0	18.74	2.8	✓																	✓	
931221 036	175.415	-41.238	60.0	22.5	-90.0	20.83	2.9	✓																	✓	
94 213 158	175.408	-41.820	15.0	7.5	-97.5	21.11	3.4	✓																	✓	
94 1 8 011	174.321	-41.584	277.5	15.0	150.0	22.62	3.0	✓																	✓	
9311 2 817	173.805	-42.350	210.0	75.0	-127.5	23.13	2.7	✓																	✓	
94 2 31412	174.320	-41.590	202.5	22.5	112.5	23.23	3.1	✓																	✓	
94 313 350	175.593	-41.018	232.5	7.5	105.0	24.41	2.8	✓																	✓	
9312311949	174.286	-42.019	67.5	67.5	-75.0	25.23	2.9	✓																		
9310291642	174.430	-41.752	67.5	45.0	-52.5	24.86	3.3	✓																	✓	
9310291827	175.272	-41.250	240.0	15.0	97.5	25.23	2.7	✓																		
9312 8 2 9	175.270	-41.277	90.0	22.5	-82.5	25.62	2.8	✓																		
9312 8 210	175.270	-41.278	105.0	30.0	-67.5	25.66	2.7	✓																		
9312 8 2 4	175.264	-41.284	247.5	82.5	-105.0	25.92	3.5	✓																		
9312101540	175.493	-41.102	352.5	30.0	-157.5	27.93	4.0	✓																		
94 1152112	174.769	-41.667	67.5	30.0	-60.0	28.28	4.0	✓																		
9312 72158	174.443	-41.878	202.5	75.0	142.5	28.29	2.9	✓																		
9311281831	174.890	-41.401	315.0	30.0	127.5	28.36	2.9	✓																		
931030 255	174.411	-41.864	7.5	52.5	180.0	28.58	2.7	✓																		
94 2 810 4	174.717	-41.514	7.5	22.5	-105.0	28.89	3.3	✓																		
9311 710 5	175.360	-40.872	202.5	45.0	142.5	29.33	2.8	✓																		
94 1202251	173.645	-42.080	97.5	67.5	-15.0	30.77	2.9	✓																		
931021 7 8	174.505	-41.800	75.0	60.0	-52.5	30.90	2.7	✓																		
9310282033	175.356	-40.790	315.0	45.0	142.5	31.26	2.9	✓																		
931213 556	174.525	-41.681	150.0	22.5	157.5	31.63	2.8	✓																		
931031 037	173.706	-41.906	90.0	52.5	-37.5	32.57	2.7	✓																		
94 3 9 434	174.077	-41.668	22.5	82.5	180.0	32.64	3.0	✓																		
94 2 7 443	173.678	-41.911	97.5	45.0	-22.5	33.20	3.0	✓																		

continued on next page...

Date	Long	lat	strike	dip	rake	Depth	Mw	R1	R2	R3	T1	T2	T3	M4	M5	M6	M7	M10	M13	F4	F8	F10	A1	A2	A3	A4
9310281352	175.063	-40.922	127.5	82.5	-37.5	33.21	2.8	✓																		
94 21212 4	173.680	-41.909	97.5	45.0	-22.5	33.26	3.4	✓																		
9312190902	175.177	-40.796	217.5	60.0	-127.5	36.03	2.8	✓																		
9312302050	174.243	-41.389	82.5	22.5	-37.5	36.48	2.8	✓																		
931215 020	174.481	-41.172	67.5	7.5	45.0	37.24	3.2	✓																		
9312 5 047	174.447	-41.191	105.0	45.0	-60.0	37.54	2.8	✓																		
9312 21055	174.031	-41.447	15.0	30.0	-112.5	40.53	3.4	✓																		
9310241816	173.581	-41.813	292.5	37.5	-105.0	40.73	4.4	✓																		
9312201614	173.424	-41.924	30.0	75.0	150.0	41.52	2.7	✓																		
94 3012327	174.154	-41.473	22.5	60.0	105.0	41.79	3.0	✓																		
94 1231454	174.376	-41.056	232.5	52.5	-157.5	42.48	3.1	✓																		
931122 742	173.563	-41.736	322.5	22.5	-157.5	45.10	2.8	✓																		
931227 643	173.332	-41.909	142.5	45.0	22.5	45.28	2.8	✓																		
931230 724	174.138	-41.326	45.0	90.0	105.0	45.33	3.2	✓																		
94 3 51530	174.814	-40.798	255.0	52.5	-67.5	45.70	2.8	✓																		
9312271211	173.813	-41.614	157.5	60.0	67.5	45.99	2.8	✓																		
9311181856	174.212	-40.770	75.0	67.5	-60.0	47.28	2.9	✓																		
9311 41206	174.255	-40.742	120.0	75.0	-120.0	48.94	2.9	✓																		
94 3 4 637	174.833	-41.121	60.0	30.0	-82.5	52.88	3.0	✓																		
94 2281022	174.837	-41.119	277.5	82.5	-15.0	53.22	4.5	✓																		
94 3 51233	174.398	-41.208	322.5	82.5	37.5	55.03	3.7	✓																		
931219 345	174.486	-41.294	97.5	30.0	-60.0	57.06	3.3	✓																		
94 2221840	174.127	-41.688	157.5	45.0	52.5	57.36	3.1	✓																		
94 2 72221	174.496	-41.136	285.0	60.0	-67.5	58.17	3.3	✓																		
94 1212249	174.366	-41.465	210.0	60.0	165.0	61.15	3.4	✓																		
9311271732	174.524	-41.100	105.0	22.5	-52.5	62.13	3.0	✓																		
9310221034	173.495	-41.674	240.0	67.5	-135.0	67.78	3.1	✓																		
931216 3 0	173.235	-41.794	37.5	75.0	127.5	81.92	3.0	✓																		
93102611 6	173.563	-41.187	120.0	75.0	7.5	84.07	3.3	✓																		
931119 843	173.219	-41.828	352.5	45.0	135.0	87.48	3.7	✓																		
94 216 840	173.238	-42.075	210.0	52.5	60.0	3.18	3.3		✓														✓			
94 228 616	172.660	-42.252	247.5	75.0	-135.0	3.74	3.0		✓														✓			
9312 222 4	172.490	-42.790	157.5	60.0	37.5	5.00	4.0		✓														✓			
9312 5 718	172.490	-42.790	60.0	67.5	180.0	5.00	3.5		✓														✓			
9311201120	172.907	-42.366	97.5	75.0	-165.0	5.63	2.7		✓														✓			
94 124 712	172.814	-42.188	165.0	82.5	-22.5	6.75	2.9		✓														✓			
94 12117 2	172.706	-42.240	307.5	82.5	-7.5	6.96	3.2		✓														✓			
9312121958	173.066	-42.886	75.0	60.0	150.0	7.29	2.9		✓														✓			
94 3 92156	172.596	-43.236	75.0	90.0	-135.0	7.87	2.7		✓															✓		
9312142351	173.056	-42.897	165.0	37.5	45.0	8.01	4.2		✓														✓			
94 1181649	173.323	-42.584	240.0	45.0	157.5	8.41	2.8		✓														✓			
93121419 3	173.053	-42.896	37.5	67.5	127.5	8.51	4.0		✓														✓			
9312310150	173.049	-42.893	75.0	90.0	135.0	8.67	3.3		✓														✓			
94 2102135	172.704	-42.234	277.5	22.5	-60.0	8.90	3.3		✓														✓			

continued on next page...

Date	Long	lat	strike	dip	rake	Depth	Mw	R1	R2	R3	T1	T2	T3	M4	M5	M6	M7	M10	M13	F4	F8	F10	A1	A2	A3	A4
94 2 121 9	172.773	-42.209	247.5	82.5	-165.0	9.26	3.5		✓														✓			
9311 8 4 0	172.863	-42.796	352.5	60.0	22.5	9.32	3.3		✓														✓			
9312 32052	172.943	-42.440	352.5	67.5	-52.5	9.59	3.0		✓														✓			
9311 32332	173.290	-42.440	90.0	22.5	-165.0	11.90	5.0		✓														✓			
9312271746	172.854	-42.401	255.0	67.5	-142.5	13.45	2.9		✓														✓			
9312 5 851	172.781	-42.804	217.5	67.5	-172.5	14.05	3.0		✓															✓		
94 211 9 7	173.573	-42.433	7.5	75.0	52.5	14.54	4.5		✓														✓			
9312 3 649	172.472	-42.787	165.0	37.5	15.0	15.49	2.8		✓															✓		
94 1 7 340	173.477	-42.617	67.5	45.0	-90.0	26.59	3.4		✓																	
94 22222 3	173.353	-42.566	285.0	52.5	-45.0	26.93	3.4		✓																	
9311101537	173.279	-42.599	135.0	82.5	67.5	27.19	2.9		✓																	
9311 7 127	173.342	-42.165	105.0	75.0	-15.0	31.88	3.1		✓																	
94 3 7 241	173.517	-42.167	202.5	30.0	-165.0	32.05	2.8		✓																	
94 310 919	173.006	-42.818	330.0	37.5	120.0	33.69	2.9		✓																	
9311 81717	172.894	-42.764	150.0	67.5	37.5	35.44	2.7		✓																	
94 2 81011	172.830	-42.023	127.5	82.5	30.0	72.44	3.6		✓																	
94 1 11457	172.398	-41.347	255.0	30.0	112.5	2.10	3.3			✓																✓
94 226 614	172.572	-40.890	120.0	30.0	-15.0	2.32	2.7			✓																✓
9310231226	172.376	-41.466	217.5	60.0	45.0	4.35	4.1			✓																✓
9310241655	172.400	-41.450	97.5	67.5	135.0	5.00	4.1			✓																✓
94 215 547	172.279	-41.583	45.0	67.5	105.0	5.44	2.9			✓																✓
94 1 118 6	172.413	-41.327	127.5	22.5	-30.0	8.31	3.0			✓																✓
94 2 82118	172.511	-41.213	45.0	67.5	82.5	8.44	2.8			✓																✓
931115 248	172.258	-41.761	217.5	60.0	45.0	8.59	3.5			✓																✓
9312 51244	172.520	-41.206	157.5	37.5	15.0	10.23	4.0			✓																✓
9311 1 642	172.470	-41.057	82.5	67.5	120.0	10.55	2.7			✓																✓
94 2161437	172.354	-41.405	172.5	60.0	52.5	12.27	2.9			✓																✓
9311 6 846	172.844	-41.627	210.0	45.0	-157.5	76.11	3.2			✓																
900210	172.74	-42.32	55	89	163	8	5.9																✓			
290622	172.85	-41.88	350	32	83	7	6.4																✓			
480522	172.99	-42.48	64	90	177	4	6.4																✓			
221225	173	-43	72	90	170	20	6.4																	✓		
290309	171.93	-42.79	65	90	-178	11	7																	✓		
920330	171.61	-43.01	70	19	134	15	5.5																	✓		
940618	171.47	-42.94	68	63	150	15	6.7																	✓		
951124	171.76	-42.88	166	60	12	15	6.1																	✓		
770511	171.48	-43.33	92	34	164	10	5.2																	✓		
940619	171.54	-43.24	172	74	2	15	5.9																	✓		
940621	171.81	-43.38	168	49	16	15	5.4																	✓		
950529	171.8	-43.47	53	67	174	15	5.5																	✓		
660423	174.4	-41.63	232	68	133	19	5.8																		✓	
800703	176.66	-40.45	146	11	28	15	5.4																		✓	
811227	175.66	-40.63	263	9	145	15	5.4																		✓	
820205	175.48	-41.15	62	28	-74	15	5.3																		✓	

continued on next page...

Date	Long	lat	strike	dip	rake	Depth	Mw	R1	R2	R3	T1	T2	T3	M4	M5	M6	M7	M10	M13	F4	F8	F10	A1	A2	A3	A4
900219	176.102	-40.347	91	16	-51	20	6.3																		✓	
900513	176.53	-40.23	220	28	149	16	6.4																		✓	
901004	175.62	-41.84	190	21	58	15	5.5																		✓	
901006	175.35	-41.56	250	38	145	20	5.4																		✓	
680523	171.96	-41.76	232	51	103	10	7.1																			✓
910128a	171.58	-41.89	42	30	99	10	5.8																			✓
910128b	171.67	-41.9	8	48	77	12	6																			✓
290616	172.2	-41.7	358	46	69	9	7.3																			✓
290619	172.43	-41.69	21	45	80	11	6.3																			✓
290622	172.86	-41.49	321	42	79	14	6.5																			✓
290715	172.29	-41.65	21	29	120	19	6.3																			✓
621510	171.32	-41.65	55	40	88	7	5.6																			✓
910128C	171.7	-41.76	66	42	136	15	5.7																			✓
910128D	171.86	-42.03	229	34	121	15	5.8																			✓
910215	171.43	-41.9	213	37	90	15	5.4																			✓
9312 32330	172.470	-42.798	292.1	82.0	-32.0	17.00	2.5															✓				
9312 3 026	172.460	-42.796	31.6	43.6	-136.0	17.40	2.5															✓				
931118 5 8	173.290	-42.436	44.5	53.3	-144.0	11.10	2.2															✓				
9312311912	172.930	-42.823	256.2	83.3	-168.0	12.20	2.1															✓				
94 1 12156	172.440	-42.820	215.5	59.6	136.0	10.80	2.4															✓				
931217 637	173.080	-42.920	224.7	58.6	176.0	14.50	2.1															✓				
94 2 1 945	172.530	-42.573	171.0	89.9	-8.0	19.40	2.3															✓				

Table C.1: **Summary of events used in inversions**

APPENDIX D

DOCUMENTATION FOR THE MOTSI INVERSION CODES

This documentation is for the use of the MOTSI stress inversion codes (Abers and Gephart, 2001) on the Mac OSX system. See Abers and Gephart (2001) for explanation of the algorithm. Below is a table that outlines the programs and the input each program needs. The usage of each program is just the name in lower case, after which there are prompts asking for the input and output file names and any additional information. The format of the input file .mot is explained in detail below.

D.1 Main inversion codes

Program	Description	Input files and information	Output files
MOTSI	Inverts first motion data for the best fitting stress tensor	.mot Index of the primary principle stress (1 or 3). The plunge, azimuth and variance of the primary principle stress. Any directions to skip? If so how many? The plunge, azimuth and variance of the secondary stress. Grid size (5 or 10). R values to search (lowest, highest, increment). Probability of making a mistake.	.out
MOTSI-1sm	Given the stress tensor and first motion data finds the set of focal mechanisms that is fits both	.mot Index of the primary principle stress (1 or 3). The plunge, azimuth and variance of the primary principle stress. The phi value (output of motsi). The R value. Probability of making a mistake.	.1sm .1.fmsi
MOTSI-fp	From the first motion data	.mot	.mfp

	this determines focal mechanisms without considering stress.	Cutoff (factor of sigma) for limit calcs. Probability of making a mistake.	.fmsi

D.2 Other useful scripts related to MOTSI

Program	Description	Input	Output
motsort	Sorts through the .mot file using several parameters and discard any picks/events/stations that dont fit the parameters. Makes a new .mot file containing the wanted picks/stations/events	.mot	.mot
getbestsi	Usage: getbestsi file.out Returns a summary of information related to the best stress model from the Motsi output file.	.out	
rvalmarg	Usage: rvalmarg file.out Gives detailed probability density function information for each increment of R.	.out	
stressmarg	Usage: stressmarg file.out 1 (or 3) Gives detailed probability density function information for the all primary stresses searched. The output is quite long so it is best to pipe the output to a file.	.out	
compfps	Usage: compfps file.mfp file.1sm Compares two sets of focal mechanism data for the same event. Used by the plotting code make.compmaps.	.mfp .1sm or any two output files	
datarank	Usage: datarank -format < file.mfp > file.txt Returns a text file that produce histograms on data quality.	.mfp	.txt
mot2ptb	Usage: mot2ptb < file.mot Calculates the trend and plunge of the P,T,B axes from focal mechanisms in a .mot file.	.mot	

D.3 Plotting codes

Code	Description	Input	Output
make.compmaps	Usage: make.compmaps file.mfp file.1sm Creates a map with variations of PTTP plotted (compmap.ps). Also plots dS vs dM (dsdm.ps). The junk files are the data used to create the plots. This code uses other codes and programs, be sure to have compsfps and GMT.	.mfp .1sm	compmap.ps dsdm.ps junk.comp junk.text

make.ptbax	Usage: make.ptbax file.mfp file.1sm Makes two plots of the P and T axes to compare the two solutions. This code uses other codes and programs, be sure to have mot2ptb, datarank and GMT.	.mfp .1sm	compare_pt.ps
motplot	Usage: motplot file.s1.out file.s3.out > file.ps Plots the stress results on an equal-area lower-hemisphere projection, using GMT. Includes confidence regions and of stress directions and *R*.	.s1.out .s3.out	.ps

Note: If you are looking at multiple datasets it is a good idea to change the name of the output files from the plotting codes so that they might relate to the input file names. Otherwise, they might be overwritten by mistake.

D.4 Input format

The first 3 lines of the .mot file are mostly for comments.

Line 1	MOT....	First 3 characters denote the format the rest of the line is comments.
Line 2	.....	A 2nd line of comments.
Line 3	999 ...	The first thing is number of events (1x, i3). the rest of the line is for comments.

Then the rest of the file is made up of event headers followed by lines for the pick information for each station.

Event header (line 4)

Referred to in code as: iy, imo, idy, ih, mn, sec, alat, alon, adep, amag, nsta, nfmot, str, dip, rake, nfcor, fpscore, wfp, pttp

Format in code: 5i2, f6.2, f7.3, f8.3, f6.2, 1x, f3.1, 2i3, f7.1, f6.1, f7.1, i3, 2(1x,f7.2), 1x, f6.3

In other words: XX|XX|XX|XX|XX[]XX.XX|-XX.XXX|-XXX.XXX|XXX.XX[]X.X|XXX|XXX[][]XXX.X[][]XX.X[]-XXX.X|XXX[]XXXX.XX[]XXXX.XX[]XX.XXX

Where [] denotes a space and | denotes a new field follows but there is no space separating them. If you do not use all the X variables replace the X with a space at the beginning of the field. If there values are positive and a negative is indicated above just replace the negative with a space.

Pick Info (line 5)

Referred to in code as: stn,ipwt,pt,iswt,st,toa,az,dist,ifm,iwt

Format in code: a4,1x,2(i1,f6.2),f6.1,2f7.1,1x,i2,1x,i1

In other words: XXXX[]X|XXX.XX|X|XXX.XX[]XXX.X[][]XXX.X|XXXXX.X[]XX[]

Repeat Pick Info lines for all stations for that event. Then repeat the Event Header followed by the Pick info for all events to be included in the inversion.

Terms used in code:

iy, imo, idy, ih, mn, sec	event time: year, month, day, hour, minute, second
alat, alon, adep	event location: latitude, longitude, depth
amag	event magnitude
nsta	number of stations recording the event
nfmot	number of first motions reported
str, dip, rake	focal mechanism for the event: strike, dip, rake
nfcor	number of first motions correctly predicted
fpscore	MOTSI score for the event
wfp	MOTSI weight (variance of picks used to calculate fpscore
pttp	statistic that calculates difference from previous mechanism
stn	station
ipwt, pt	arrival time weight, P-wave arrival time
iswt, st	arrival time weight, S-wave arrival time
toa	take off angle
az	azimuth (degrees from north, from the earthquake to the station.
dist	distance from the event (km)
ifm	first motion pick: 1=up, −1 =down, 0=nodal
iwt	first motion weight

D.5 Running codes on Mac OSX

Firstly, you need to have g77. I came across a problem with libutils.a that runlib would fix. The following is what the SES Unix administrator did to fix the problem. The symbol > represents a command follows, when there is no symbol it represents the output from a command and when there is a symbol and no command it means there should be no output.

Start with - Motsi02 from tarball: Example README Test bin lib src

Basic problem: compiler error - "use ranlib". However, ranlib didn't work, probably because libutils.a was compiled on another system.

```
======= Solution ==========
Summary: remake libutils.a, then the binaries can be compiled!
Details: (all paths relative to Motsi02)
(Note: .o files (ie: letter "oh") should be safe to remove prior to
recompile)
> rm lib/libutils.a
>
Tweak makefile - function "pamp" is duplicated. Change line 1 thus:
Old: SOURCES=ptbax.f pamp.f plotsrad.f pt2np.f auxplnew.f
New: SOURCES=ptbax.f plotsrad.f pt2np.f auxplnew.f
kludge f77 to point to g77. One way: make symbolic link called "f77",
pointing to real g77. On my computer, I have...
```

```
PATH:
/usr/local/bin:/Volumes/SES1/Users/ralph/bin:/sw/sbin:/Users/ralph/bin:
/sw/bin:/sw/bin:/bin:/sbin:/usr/bin:/usr/sbin
so, can do this:
> ln -s /usr/local/bin/g77 ~/bin/f77
>
> cd src/Utils
> make
f77 -g -c -o ptbax.o ptbax.f
ar rv ../../lib/libutils.a ptbax.o
ar: creating archive ../../lib/libutils.a
a - ptbax.o
f77 -g -c -o plotsrad.o plotsrad.f
ar rv ../../lib/libutils.a plotsrad.o
a - plotsrad.o
f77 -g -c -o pt2np.o pt2np.f
ar rv ../../lib/libutils.a pt2np.o
a - pt2np.o
f77 -g -c -o auxplnew.o auxplnew.f
ar rv ../../lib/libutils.a auxplnew.o
a - auxplnew.o
rm ptbax.o plotsrad.o auxplnew.o pt2np.o
>
check file:
> cd ../..
> ls -l utils
total 240
-rwx------ 1 ralph admin 50788 16 Apr 15:00 libutils.a
-rwx------ 1 ralph admin 72208 25 Apr 2002 libutils.a.org
>
All good. Onwards...
> ranlib -s lib/libutils.a
> cd src
> make
g77 -O motsi.f -o motsi
g77 -O motsi-1sm.f -o motsi-1sm
g77 -O motsi-fp.f -o motsi-fp
g77 -g compfps.f -L../lib -lutils -o compfps
g77 -g datarank.f -L../lib -lutils -o datarank
g77 -g fit-by-sta.f -L../lib -lutils -o fit-by-sta
g77 -g motsort.f -o motsort
g77 -g rankfit1.f -o rankfit1
g77 -g rankfit2.f -o rankfit2
g77 -g getbestsi.f -o getbestsi
g77 -g mot2ptb.f -L../lib -lutils -o mot2ptb
g77 -g motplot.f pssubs.f -o motplot
```

```
g77 -g rvalmarg.f -o rvalmarg
g77 -g stressmarg.f -o stressmarg
>
```

Martha Savage

From: Cassidy, John [JCassidy@NRCan.gc.ca]
Sent: Wednesday, 20 October 2004 10:15
To: Martha Savage
Subject: RE: marking an MSc thesis?

Hi Martha,

Natalie's thesis is terrific! Nice research, and such a well-organised, and well-written thesis.
This should be easy to publish! (other than the usual challenge of removing 90% of the thesis to create a journal article!).

Returning the thesis was delayed slightly - I have an injured back and have spent quite a bit of time at doctor's offices, x-rays etc last week.. Anyway, the thesis is on it's way now via courier and will be there on Friday.

I have precious few comments (other than minor edits throughout) - far fewer than on most journal articles that I review. This reflects how well the thesis was written!
One area that I feel could use a little more clarification/discussion is the focal depths of earthquakes used in the crustal S-wave splitting study. For example, on page 33 ("Depth-Dependence of Observations") it is pointed out that the crustal thickness is 15-25 km, and that most earthquakes used are 50 km or less... So, are most earthquakes at 10 km depth? 20 km? Or are they in the continental upper mantle at 25-50 km? The candidate makes a very good case for the anisotropy being concentrated in the uppermost crust. However, by clarifying whether the earthquakes occurred in the crust, or deeper in the mantle, perhaps something could be concluded about anisotropy (or the lack of it?) In the lower crust, or more importantly, in the uppermost mantle...

That is about all. I look forward to seeing the published article!
Would it be possible to get a copy (digital or paper) of Natalie's thesis?

Talk with you soon Martha,

Cheers,
John

-----Original Message-----
From: Martha Savage
To: Cassidy, John
Cc: John Townend
Sent: 10/18/2004 12:24 AM
Subject: RE: marking an MSc thesis?

Hi John,

We're about to submit a paper based on Natalie's MSc thesis. I haven't yet seen your comments, which probably went to the Head of School who is sometimes getting behind with these things. I'm wondering if you might be able to send some of your comments directly to us--particularly the ones that would be useful to address before submission.

Thanks again for your help.

Martha

Internal Reviewer Report (Tim Little) on M Sc thesis of Natalie Balfour, entitled, "Stress and crustal anisotropy in Marlborough, NZ, Frictional-strength of faults and structure controlled anisotropy"

Abstract:

Concise and well written. But not much specific factual content.

Author states that 60deg angle btwn max comp stress and fault strike is greater than that expected for Andersonian faults. She is evaluating a long-lived, extant fault system however, not an "Andersonian" fault that has just formed at an ideal angle from previously intact, unfractured rock. Thus a 60deg angle in some ways is not really an "unexpected" angle, as the faults are probably long-lived, pre-existing structures that have been inherited into the present regime. I know that the author knows/appreciates this, however I find the way that that this is presented to be a little misleading.

Also as a struc geologist, I find the term "stress-related anisotropy" to be a little vague/misleading, as presumably it is the physical presence of arrays of cracks in the rock that would cause anisotropy not really the "stress" (even if these cracks are opened in response to stress). This point is underscored by the actual results of this study as foreshadowed in the abstract , where a set of old fractures (MFS faults) dominate the crustal anisotropy signal. In both end member "cases" considered, anisotropy is caused by fracturing; in both cases these fractures are a result of *stress*.

Introduction:

Concise. Nice summary of previous work. Nice, clear and informative color figures

At risk of sounding partisan/selfserving, I would say that the emphasis on Nicol and Wise Pettinga etc inversions is a bit surprising/overdone. These data were collected from faults chiefly in Mesozoic greywacke over a fairly limited spatial extent. The Sh data of Little and Jones (based on pebble fracturing, paper is included in ref list but not actually mentioned here) was collected from late Miocene-Pliocene rx and covers a fairly wide region in NE MFS. A Post Pliocene stress inversion result (Gephart method) from a data set of 100's of faults near the Awatere F are also presented in Little, 1996 (j Struc Geol, v 18 p.321)

Author states that "average strike" of MFS faults is 55. In fact the situation is more complicated than that, with the MFS including spatially distinct domains that have rather different strikes. (treatment seems unecessarily over simplified).

The language is vague in places
Terms "*coupled*" and "*locked*" are not well defined and have an unclear meaning in this context. Not clear if the author knows what these terms mean physically.

And again w/ respect to:
"Slip-rate deficit"...*of what?...with respect to what else?*

Also "partitioning" is used as if this has a known specific meaning, which I do not think it has. *Partitioning of what...to where??*

Strain rates are quoted for MFS as if this is a simple scalar quantity. What *kind* of strain rates, which *components*?

Description of Liu and Bird (2002) model, which seems quite relevant and important to this study, is presented in one sentence. The assumptions and techniques used are not really identified or discussed? For example were plate motions input as a boundary condition?

The analogy of MFS w/ S And may be emphasized too much. The former are part of an oblique collision zone and consists of dipping faults with a distinct reverse component, for example.. It is expectable that the stresses are likely to be different in the two areas, and perhaps at a higher angle to fault strike in NZ. *(OK I see this is acknowledged later in the paper).*

Theory

Treatment of elasticity etc seems fine.

Author states (p 20) that if one has a weak fault, then sigma 1 must be at a "high angle" to it. This statement seems inexact at best and incorrect at worse. For example it seems to ignore the effect of stress ratios/magnitudes and the type of fault (eg thrust vs strike slip). Also, if a fault is weak, then it *might* be able to move where the compression direction is at quite a vanishingly *low* angle to it or a high angle to it, or at an "ideal" angle to it, so I do not really understand this statement.

Outlining of stress tensor systematics seem OK though I did not know what "the vertical plane" was in p 24. *Which vertical plane, is there only one?*

For a case of nonvertical axes isn't it the PLUNGE of the principal stresses that additionally need to be specified? Author says "azimuth"
Is this correct?

Nice summary of stress inversion algorithms, their assumptions, etc.

Seismic Anisotropy

Tough going for me in terms of technical aspects of waveform modelling etc, so I did not read these in detail, although the writing does seem thorough with careful treatment of errors etc.

Complex nature of the shear wave splitting results, as explained in the Discussion, suggest that the interpretation of these types of data are nonunique. Some parts are quite difficult for a nonseismologist to grasp, in part because of vocabulary differences.

I wish author would have been succinct about what *robust* conclusions come out of this aspect of her work.

Focal Mechanisms, Stress Orientations
P 61
Northern MFS said to have distinct stress inversion result (eg S2 less persistently vertical). In fact,the faults strike quite differently there relative to the south, and have distinct reverse component unlike their southern cousins, so it is not surprising to see this stress inversion difference. The kinematic differences, however, were not even mentioned in the Intro, where the entire MFS was attributed a "mean strike" of 050.

Nice figures, data presentation and interesting results.

Comparison between methods is illuminating.

I am startled at the diversity of R values derived by the different methods for Lake Tennyson data!

Fig 4.6. Needs better labelling.
Caption talks about mechanisms being plotted on the "right" and "left" but the data actually sweem to be plotted ABOVE and BELOW each other. Difference between RED and BLUE focal mechanisms on the graph is not explained/pointed out.

How can dS ever be positive (as at least two events in Fig 4.6 seem to be), if the whole idea is to steer focal mechanisms into accord with a single stress tensor? This is not explained well enough for me to avoid confusion.

I have a hard time figuring out if/where any circularity exists in some of the results, ie of course a stress-constrained model will be give a result more consistent with the *stress* model but does this really make it "improved"? What does "improved" mean in this context.

Again I am a little disappointed that the derived Sh data are only cursorily compared (less than 1 sentence) to the Little and Jones (98) data set, and this actually done out of context (she implies on p. 75 that our data were collected from reverse faults in the Wellington region). Our results from NE MFS yielded a regional Sh result that is within error of this focal mechanism-derived one. This correspondence implies that stress in northern MFS may have been relatively stable on a time frame of several my., but without a comparison between the data sets being made, any potential insight into the time dimension is lost. The author was aware of these data but did not appear to recognize the significance fully.

60 deg "average angle" again seems misleading given the distinctly *domainal* nature of fault strike in N vs S parts of MFS. Rather than throwing everything into 1 bag, perhaps the regional data "clusters" should have been <u>used,</u> in conjunction with their locally appropriate fault strikes so that this statement could been a more exact one.

Discussion

Inappropriately 2D nature of Mohr analysis?. The MFS faults are not pure strike-slip faults like much of the S. Andreas! The inferred ~60 deg angle is measured <u>horizontally</u> between fault *strike* and *trend* of *Sh* max, not the 3D angle between the

NW-dipping(?) oblique-reverse MFS fault planes and (+-plunging?) sigma 1? This could make a difference in the calculated magnitude of the weakening effect as measured by either a coeff of friction or by a fluid pressure ratio. The author should at least discuss the 3D nature of the actual situation and how it might complicate her analysis?

The apparently higher beta angle in northern Marlborough may be related to the associated of change in fault strike to NE there?? See my earlier comments about this!

Good succinct list of conclusions of this study

Appendices:
Well laid out. Good.

Overall Comments:
This is a solid, well-organized and well written piece of work. The shear-wave splitting vs stress/focal mechanism aspects of the study did not, in the end, dovetail well together, but Natalie clearly demonstrates competence in applying both techniques and comes up w/ an important new data set of relevance not only in New Zealand but generally. I have no doubt that parts of this thesis will be published in international journals.

In places, she makes small omissions or includes overly sweeping comments that may reveal an incomplete understanding of some concepts, but this is to be expected for an MSc candidate! As suggested in some of my comments above, the interpretation of some of her results would have been beneficially reinforced or extended by more reference to geological aspects of the MFS.

Overall I am quite impressed. I am tempted to suggest a grade of A-, but as this is not really my field (and there are parts, esp. seismic anisotropy systematics) that I did not read or understand in detail, I would be willing to swing at least a mark up or down on this grade. She is to be congratulated on an excellent piece of work!

Martha Savage

From: Natalie.Balfour@ga.gov.au
Sent: Monday, 31 January 2005 10:55
To: Martha Savage; John Townend
Subject: FW: Geophysical Journal International - GJI-04-0447

Regards,

Natalie Balfour

---- Original Message ----
From: mew@ras.org.uk
To: balfounata@student.vuw.ac.nz, nataliebalfour@hotmail.com
Subject: FW: Geophysical Journal International - GJI-04-0447
Date: Fri, 28 Jan 2005 10:14:33 -0500 (EST)

Dear Ms. Balfour

We have now received reviews of your manuscript GJI-04-0447 entitled "Stress and Crustal Anisotropy in Marlborough, New Zealand: Evidence for Low Fault Strength and Structure-Controlled Anisotropy". These are appended. Taking these reviews into account, the Editor, Dr. Russ Evans, feels that some minor revision of your manuscript is required, after which he will be pleased to give further consideration to publication in Geophysical Journal International.

The editor makes the following additional comments: "Thank you for the opportunity to read and consider your paper. The reviewers are both very complimentary about the standard and (especially) the quality of preparation of your paper. Thank you for making the editor's job a little easier! Although Stephanie Prejean considers the paper could be published "as is", she offers a few suggestions for further improvement. The reviewer who wishes to remain anonymous feels similarly. There is some commonality between the points they raise. I invite you to take advantage of this opportunity to undertake some minor revision to address these points. I feel sure you will not find this onerous and look forward to receiving a revised manuscript shortly.".

You now have six months in which to submit your revision, but we hope that you will be able to make the necessary revisions well within that time. If you do not submit a revised version of your manuscript within six months it will be deemed withdrawn. We would be happy to see your revised version after that date, but it will be handled as a new submission. In any event, you should quote the reference number of this manuscript.

Please submit your revised manuscript at http://gji.manuscriptcentral.com logging in with your UserID and Password. Click on the "Revised Manuscripts" icon and submit your response to the reviewers' comments. You may then upload your revised manuscript by clicking on its title and following the on-screen instructions. Important: Do NOT submit your revised manuscript as a new paper UNLESS you have exceeded the six-month deadline.

Regards,

Marie Williams

Reviewer 1 Comments:

This paper is in great shape and is basically ready to publish as is. It's an important research problem that was well posed, thoroughly executed, and clearly written. The figures are very nice. The question of fault strength is an important one in the seismology community. It's essential that non San Andreas studies like this one are conducted to help resolve some of the questions in that field.

I have just a few minor suggestions to the authors, but the paper is basically publishable as is.

1. What kind of quality control are you doing on mechanisms that go into the stress inversions, any other than the basic selection criteria you list?

2. It would be nice to see a table of error outputs (or misfits) from the three stress inversion programs used. So many people use these output errors to interpret confidence in results. Can you add a few sentences comparing the error or fit results given by the different methods perhaps?

3. Figure 1 - Label the MFS (or is it the entire figure area?).

4. Last sentence of first paragraph on page 4 (in the case of a weak fault..."): At this point in the paper, it's not clear why this statement would be correct. Perhaps add another sentence explaining.

5. First sentence under section 2.1: Add the word "magnitude" after the words "vertical stress".

6. How large an area do the groups of focal mechanisms cover in space?

7. Second sentence under section 2.2: I don't entirely understand this. Another sentence or phrase of explanation would be helpful.

8. What range of earthquake magnitudes are you using for the anisotropy study? What kind of 'short period' seismometers are you using specifically? I've never done anisotropy studies, so this might be a naive question. I'm wondering if you use a large magnitude range of earthquakes and are sampling different frequency bands as a result, could you be measuring different scales of anisotropy with different event-instrument pairs?

9. Section 3.1 - Can you point to the Lake Tennyson area specifically on one of the early map figures?

10. Can you comment on the magnitude of anisotropy observed? What can we learn about the material properties or crust from these delay times specifically?

11. It would be nice if you included a few more sentences discussing the implications that arise from observations that these faults and the SAF are weak. How might these results apply beyond these two areas? Have any similar studies been done any where else that support fault strenght/weakness in different environments or on different scales?

12. First sentence page 16. Add location that Zinke and Zoback studied.

13. Last paragraph before conclusions. It's not entirely clear how this paragraph is relavent to your research. Perhaps add a sentence explaining why you discuss this study.

Reviewer 2 Comments:

This paper requires only minor alteration / additions before it is in a publishable form.

The paper describes results from a stress inversion and seismic anisotropy study. From reading the initial paragraph of the introduction the relevance of writing a paper with both these techniques in is not as apparent as it should be. Whilst reading the manuscript I was left with the question 'isn't this 2 papers being squeezed in to 1?' for too long. This problem can be easily solved by some additional sentances in the first paragraph of the introduction.

I understand a summary or abstract should be a stand-alone section to a paper. The abstract needs minor additions. Where are the Marlborough and Wellington faults? What sort of faults are they? (1st sentance). The sentance (line 8) about shear-wave splitting interupts the description of the stress results. The anisotropy results need to be quantified to imply large error bars.

p2 SHmax needs defining when first mentioned in the Introduction.

p3 Bibby 1993; Holt and Haines 1988 in text but not in references

p7 a reference to figure 6 when describing the clustering would help the readers understanding

Figure 6 unclear why the clustering algorithm has chosen certain events in the overlapping clusters 5 and 10.

p8 Units of slowness in equation 5.

p10 define variables in equation 6

p14 'whether the apparent weakness is an artifact resulting from inadequate near-fault resolution' please clarify this statement as it is unclear what it means.

p11 not convinced that the paragraph on the discussion on anisotropy betwen 50-100km at WAG is required.

A comment in the discussion on the direction of plate motion relative to stress direction and anisotropy in the crust could be interest.